

NUMERICAL PREDICTION AND EXPERIMENTAL INVESTIGATION OF  
FRETTING FATIGUE CRACK INITIATION AT RAILWAY AXLE - WHEEL  
CONTACTS

A THESIS SUBMITTED TO  
THE GRADUATE SCHOOL OF NATURAL AND APPLIED SCIENCES  
OF  
MIDDLE EAST TECHNICAL UNIVERSITY

BY

GÖKSU GÜRER

IN PARTIAL FULFILLMENT OF THE REQUIREMENTS  
FOR  
THE DEGREE OF DOCTOR OF PHILOSOPHY  
IN  
METALLURGICAL AND MATERIALS ENGINEERING

APRIL 2017



Approval of the thesis:

**NUMERICAL PREDICTION AND EXPERIMENTAL INVESTIGATION OF  
FRETTING FATIGUE CRACK INITIATION AT RAILWAY AXLE -  
WHEEL CONTACTS**

submitted by **GÖKSU GÜRER** in partial fulfillment of the requirements for the degree of **Doctor of Philosophy in Metallurgical and Materials Engineering Department, Middle East Technical University** by,

Prof. Dr. Gülbin Dural Ünver  
Dean, Graduate School of **Natural and Applied Sciences**

\_\_\_\_\_

Prof. Dr. Cemil Hakan Gür  
Head of Department, **Metallurgical and Materials Engineering**

\_\_\_\_\_

Prof. Dr. Cemil Hakan Gür  
Supervisor, **Metallurgical and Materials Engineering Dept., METU**

\_\_\_\_\_

**Examining Committee Members:**

Prof. Dr. Tayfur Öztürk  
Metallurgical and Materials Engineering Dept., METU

\_\_\_\_\_

Prof. Dr. Cemil Hakan Gür  
Metallurgical and Materials Engineering Dept., METU

\_\_\_\_\_

Prof. Dr. Cevdet Kaynak  
Metallurgical and Materials Engineering Dept., METU

\_\_\_\_\_

Assoc. Prof. Dr. Özgür Aslan  
Mechanical Eng. Dept., Atılım University

\_\_\_\_\_

Assist. Prof. Dr. Kazım Tur  
Metallurgical and Materials Eng. Dept., Atılım University

\_\_\_\_\_

**Date:** 28.04.2017

**I hereby declare that all information in this document has been obtained and presented in accordance with academic rules and ethical conduct. I also declare that, as required by these rules and conduct, I have fully cited and referenced all material and results that are not original to this work.**

Name, Last name: Göksu Gürer

Signature :

## **ABSTRACT**

### **NUMERICAL PREDICTION AND EXPERIMENTAL INVESTIGATION OF FRETTING FATIGUE CRACK INITIATION AT RAILWAY AXLE - WHEEL CONTACTS**

Gürer, Göksu

Ph. D., Department of Metallurgical and Materials Engineering

Supervisor: Prof. Dr. Cemil Hakan GÜR

April 2017, 149 pages

The aim of this thesis is to develop a procedure based on the multi-axial fatigue theories that can be used at the design stage for minimizing fretting fatigue failures of the railway axles. The premature fretting fatigue failure of the press-fitted wheel-axle assembly was investigated by means of mechanical and metallurgical methods. First, the loading path obtained through finite element analysis was implemented into the stress-based multiaxial fatigue models to predict possible sites of crack initiation. Then, the computed multiaxial fatigue index of the identified loading path was compared with the reduced fatigue limit presented by the Kitagawa analysis to describe the threshold conditions for fretting fatigue initiation and to define the onset of fatigue crack propagation. The stress intensity factor and the tangential stress at the permissible defects were determined by using the weight functions. The results of the analyses were compared to and verified with those obtained from the metallurgical investigations of the full-scale 34CrMo4 axles failed during service. The effects of the microstructure, the contact surface, and the applied press-fit interference on the initiation of fretting fatigue cracks were discussed. The possible mechanical and metallurgical treatments to improve the fretting fatigue resistance were presented. The consistency between the results of fractographic investigations and numerical analyses

reveals that the proposed procedure can be used as an effective tool to assess the risk of fretting damage through uniaxial coupon tests. This procedure also gives designers an opportunity to evaluate the effects of the selected assembly and geometry parameters on fretting fatigue before conducting expensive and time-consuming full-scale axle tests which are requested by international standards.

**Keywords:** Fretting fatigue, multi-axial fatigue, railway axle, structural integrity, weight function solution, finite element analysis.

## ÖZ

### **DEMİRYOLU DİNGİL-TEKER TEMAS YÜZEYLERİNDE AŞINMA ÇATLAĞI OLUŞUMUNUN NUMERİK YÖNTEMLERLE TAHMİNİ VE DENEYSEL OLARAK İNCELENMESİ**

Gürer, Göksu

Doktora, Metalurji ve Malzeme Mühendisliği Bölümü

Tez Yöneticisi: Prof. Dr. Cemil Hakan GÜR

Nisan 2017, 149 sayfa

Bu çalışmanın amacı, demiryolu akslarında aşınma çatlağı bağlantılı yorulma hasarlarını azaltmak için, çok eksenli yorulma modellerini esas alan ve aks tasarımı aşamasında kullanılabilecek bir prosedürün geliştirilmesidir. Bu amaçla, teker-aks sıkı geçirmelerindeki aşınma çatlağı bağlantılı erken yorulma hasarları mekanik ve metalurjik açılardan ele alınmıştır. Mikroyapı, temas yüzeyi özellikleri ve geçme sıklığının aşınma-yorulma çatlaklarının oluşumuna etkileri ve bu tip çatlakların oluşumunu önlemeye yönelik mekanik ve metalurjik işlemler irdelenmiştir.

Sayısal analizlerde ilk olarak, aşınma bölgesine uygulanan yük çevrimleri sonlu elemanlar analiziyle belirlenmiştir. Takiben, gerilme tabanlı çok eksenli yorulma modelleri vasıtasıyla bu yük çevrimleri sırasında oluşabilecek çatlaklar için hassas bölgeler, yorulma endeksi değeri ile ifade edilmiştir. Elde edilen yorulma endeksi değerleri, Kitagawa analizinden elde edilen deneysel yorulma gerilmeleriyle karşılaştırılarak, aşınma çatlaklarının başlangıç ve ilerlemesinin eşik koşulları tanımlanmıştır. Son olarak, izin verilebilir hatalara karşılık gelen etkin gerilme yoğunluğu faktörü ve teğetsel gerilmeler ağırlık fonksiyonu yöntemi ile hesaplanmıştır.

Hesaplamalar sonucunda elde edilen deęerler, yorulma nedeniyle kullanım dıřı kalan 34CrMo4 aksları üzerinde yapılan deneylerin ve hasar analizlerinin sonularıyla karřılařtırılmıřtır. Karřılařtırma sonuları, sadece tek eksenli yorulma deneylerinin sonularına ihtiya duyan bu prosedürün, akslardaki aşınma yorulması riskinin tasarım aşamasında deęerlendirilmesi iin kullanılabileceęini gstermektedir. Bu prosedür, uluslararası standartların zorunlu tuttuęu gerek boyutlu komponent deneyleri öncesinde, tasarımcılara farklı boyut ve sıkı geme parametrelerinin etkilerini deęerlendirme imkanı da sunmaktadır.

**Anahtar Kelimeler:** Aşınma yorulması, ok eksenli yorulma, demiryolu aksları, yapısal bütönlük, aęırlık fonksiyonu özümü, sonlu elemanlar analizi



*To My Family,*

## ACKNOWLEDGEMENTS

I would like to express my sincere appreciation to Prof. Cemil Hakan Gür for his supervision, support and encouragement throughout the study.

I am grateful to Prof. Dr. Stefano Beretta and Dr. Stefano Foletti for their guidance and hospitality during one year I spent at Politecnico di Milano. They helped me to gain knowledge and skills about design, analysis, and qualification of railway axles. I would also thank Dr. Danielle Regazzi for his cooperation and guidance in finite element analysis.

Chief engineers Atilla Keskin and Çetin Tekin (TCDD / DATEM) helped us to provide the damaged railway axles which constitute the mainstays of this study. Undoubtedly, this study could not be accomplished without their support and invaluable experience. Technical expenses of this study were fully supported by “Research and Development” group of “METU Welding Technology and Non-Destructive Testing Center.” I would like to thank Dr. Koray Yurtışık, Dr. Süha Tirkeş, Dr. Turhan Güngör, Murat Tolga Ertürk, Burcu Anık, Mine Kalkancı for their professional support, friendship and generosity.

I would like to thank “METU Welding Technology Non-Destructive Testing Center” staff Seyhan Çamlıgüney, Orcan Kolankaya, İlker Yelbay, Tuğçe Kaleli and Hüseyin Hızlı for their support in NDT investigations.

I am thankful to Burak Özcan, Hafize Çakmak, Uygur Tosun, Mehmet Çağırıcı, Kubilay Savcı Yeşildemir and technicians who contributed to the experimental part of this study.

I would also like to thank my beloved friends Ayşe Günay, Berat Yoldaş, Kemal Bayhan and Volkan Ertürk.

Finally, I owe a debt to my family for their endless love, support and encouragement throughout my life.

This research has been supported by “The Scientific and Technological Research Council of Turkey (TUBITAK)” / 2211C grant program.

## TABLE OF CONTENTS

ABSTRACT .....	v
ÖZ .....	vii
ACKNOWLEDGEMENTS .....	x
TABLE OF CONTENTS .....	xi
LIST OF TABLES .....	xv
LIST OF FIGURES.....	xvi
1. INTRODUCTION .....	1
1.1. Motivation .....	1
1.2. Aim and Main Contribution of the Thesis.....	4
2. THEORY AND LITERATURE REVIEW .....	7
2.1. Literature Review .....	7
2.2. Fretting Fatigue .....	10
2.2.1. Initiation of Short Fretting Cracks .....	13
2.2.1.1. Isotropic Hardening .....	15
2.2.1.2. Kinematic Hardening.....	16
2.2.1.3. Ratcheting (Cyclic Creep).....	17
2.2.1.4. Non-proportional Cyclic Hardening .....	18
2.2.2. Fretting Fatigue Tests .....	20
2.3. Mechanical Investigation of Rail-Wheel- Axle Contact .....	21
2.3.1. Vertical Contact Stresses .....	21
2.3.2. Press- Fit Stresses .....	23
2.3.3. Slip and Stick at the Cylindrical Contact.....	24
2.3.4. Translation of Stress at an Internal Point.....	26
2.4. Multiaxial Loading Paths and Multiaxiality Assessment.....	28
2.4.1. Proportional and Non-Proportional Loading .....	28
2.4.2. In-Phase and Out-of-Phase Loading.....	29
2.5. Multiaxial Fatigue .....	30

2.5.1. Modes of Failure in Fatigue Loading .....	31
2.5.2. Small Cracks .....	32
2.6. Multiaxial Fatigue Models .....	34
2.6.1. Stress-Based Models .....	35
2.6.1.1. Critical Stress Approach .....	35
2.6.1.1.1. Gough.....	35
2.6.1.1.2. Sines.....	36
2.6.1.2. Critical Plane Approach .....	36
2.6.1.2.1. Findley .....	36
2.6.1.2.2. Mataka .....	37
2.6.1.2.3. Mc Diarmid.....	37
2.6.1.2.4. Liu – Mahadevan .....	37
2.6.1.3. Mesoscale Approach Models .....	39
2.6.1.3.1. Dang - Van.....	39
2.6.1.3.2. Correction for Dang-Van Model.....	41
2.7. Crack Propagation.....	41
2.7.1. Basic Concepts.....	42
2.7.2. Calculation Elastic Strain Energy Release Rate (G).....	43
2.7.3. Calculation of Stress Intensity Factor .....	44
2.7.3.1. Estimation of Stress Intensity Factor by Finite Element Method .....	46
2.7.3.2. Estimation of Stress Intensity Factor by Weight Function Solutions.....	46
2.7.4. Plastic Strain Field around Crack Tip .....	49
2.7.5. Out-of-Plane Deformations.....	51
2.7.6. Fracture Mechanics-Based Models .....	52
2.7.6.1. Mixed Mode Growth Models .....	54
2.7.6.1.1. Maximum Tangential Stress Model.....	54
2.7.6.1.2. Crack Tip Displacement Model.....	55
2.7.6.1.3. Strain Energy Release Rate Model .....	56
2.7.6.1.4. Strain Energy Density Model .....	56
3. EXPERIMENTAL PROCEDURE .....	59

3.1. Experimental and Analytical Approach .....	59
3.2. Material and Geometry .....	61
3.3. Metallurgical Characterization .....	66
3.4. Failure Investigation .....	66
3.4.1. Magnetic Particle Inspection .....	67
3.4.2. Determination of Crack Depth and Distribution.....	69
3.4.3. Fractography .....	72
3.5. Mechanical Characterization .....	72
3.5.1. Conventional Mechanical Tests.....	72
3.5.2. Fracture Toughness Tests .....	73
3.5.3. Fatigue Tests .....	73
3.5.4. Kitagawa – Takahashi Analysis.....	75
3.5.5. Fatigue Crack Growth Rate Tests.....	76
3.5.6. Cyclic Plasticity Tests.....	77
3.6. Finite Element Analysis .....	78
3.6.1. Meshing .....	79
3.6.2. Loads and Boundary Conditions .....	79
4. RESULTS AND DISCUSSION.....	81
4.1. Stress Analysis.....	81
4.1.1. Stress Distribution at Press-Fit Seat .....	82
4.1.2. The Effect of Friction Coefficient .....	89
4.1.3. Multiaxiality Analysis .....	91
4.1.4. Loading Path and Proportionality Analysis.....	94
4.2. Fractographic Investigation of Fretting Fatigue Cracks .....	96
4.2.1. Size and Distribution of Fretting Fatigue Cracks .....	98
4.2.2. Metallurgical Condition of the Axle Material .....	105
4.2.3. Surface Deformations .....	109
4.2.3.1. Effect of Surface Roughness.....	113
4.2.3.2. Effect of Metallic Inclusions.....	114
4.2.4. Crack Propagation Plane.....	115

4.3. Multiaxial Fatigue Assessment .....	119
4.3.1. Stress-Based Approach .....	119
4.3.1.1. Uniaxial Fatigue Tests.....	119
4.3.1.2. Kitagawa - Takahashi Analysis.....	122
4.3.1.3. Dang –Van Multiaxial Fatigue Model .....	123
4.3.1.4. Liu – Mahadevan Multiaxial Fatigue Model .....	126
4.3.2. Fracture Mechanics Based Approach .....	128
4.3.2.1. Fracture Toughness Tests.....	128
4.3.2.2. Fatigue Crack Growth Rate.....	130
4.3.2.3. Maximum Tangential Stress Criterion .....	131
4.3.2.3.1. Prediction of Fatigue Crack Initiation .....	131
4.3.2.3.1. Prediction of Fatigue Crack Propagation.....	133
5. SUMMARY AND CONCLUSIONS .....	137
REFERENCES .....	141
CURRICULUM VITAE .....	149

## LIST OF TABLES

### TABLES

Table 1 Material parameters for fatigue damage evaluation.....	39
Table 2 Angle coefficients for weight function solutions.....	48
Table 3 SIF Results for the inclined cracks obtained by weight function .....	49
Table 4 Comparison of the weight function solution and SIF handbook. ....	49
Table 5 Chemical composition for EA grade railway axles and 34CrMo4.....	62
Table 6 Minimum mechanical requirements for some railway axle materials. ....	62
Table 7 Crack depths and positions coinciding with radial direction. ....	104
Table 8 Spectral analysis (by weight %). ....	105
Table 9 Tensile properties of 34CrMo4 railway axle steel. ....	108
Table 10 Fatigue limits under tension and shear loading. ....	120
Table 11 Results of the fracture toughness tests (ISO 12135).....	129

## LIST OF FIGURES

### FIGURES

Figure 1 Ultrasonic inspection: (a) solid axle, (b) hollow axle .....	2
Figure 2 Typical damage accumulation locations on the railway axles .....	2
Figure 3 Circumferential crack under wheel press-fit .....	4
Figure 4 Typical failure locations inspected at G1 axles (DE24000 locomotives) ....	4
Figure 5 Critical initiation locations for fretting cracks on railway axles .....	11
Figure 6 Fretting damage and adhesion between contact surfaces .....	11
Figure 7 Fretting map .....	12
Figure 8 Layers of surface deformation .....	13
Figure 9 Scale of surface damage .....	14
Figure 10 Schematic explanation of isotropic hardening .....	16
Figure 11 Schematic explanation of kinematic hardening .....	16
Figure 12 Isotropic and kinematic hardening during non-proportional loading .....	17
Figure 13 Non-proportional path of (a) cyclic stress, (b) and strains .....	18
Figure 14 Cyclic stress-strain for proportional and non-proportional hardening .....	19
Figure 15 Fretting pad set-up for fretting tests .....	20
Figure 16 Test jigs for full-scale component test (a) Minden type, (b) Vitry type ...	21
Figure 17 Contact of elastic cylinders .....	22
Figure 18 Tractive rolling contact of similar cylinders .....	25
Figure 19 Coordinates of stress at an internal point .....	27
Figure 20 Loading paths and non-proportionality factor .....	29
Figure 21 In-phase and out-of-phase loading .....	29
Figure 22 Modes of failure and crack propagation paths under uniaxial loading .....	31
Figure 23 Two different cases of crack propagation .....	32
Figure 24 Stages of crack propagation under uniaxial cyclic stress .....	32
Figure 25 Kitagawa - Takahashi Diagram .....	33
Figure 26 :Macro and micro stresses as a function of time on a volume $V(M)$ .....	40
Figure 27 Limiting curve for Dang Van failure criteria .....	41
Figure 28 Change in compliance with increasing physical crack size .....	43



Figure 29 Stress field around crack tip .....	44
Figure 30 Modes of crack propagation and tearing on a minute crack .....	45
Figure 31 Stress distribution along x'y' axes placed on the inclined crack plane .....	47
Figure 32 Tensile stress and plastic zone around crack tip. ....	50
Figure 33 Size effect in fracture toughness testing .....	51
Figure 34 Out-of-plane deformations.....	51
Figure 35 Crack growth in mixed mode loading for low carbon steels. ....	53
Figure 36 Crack tip deflection and its translation to the x-y coordinate plane. ....	55
Figure 37 Flow diagram for the analytical and experimental methods.....	60
Figure 38 Flow diagram for fractographic analysis. ....	61
Figure 39 Critical parts of solid (right), hollow (left) railway axles. ....	63
Figure 40 S-transition and T-notch. ....	63
Figure 41 Effective diameter and notch radius for non-powered and powered axle	64
Figure 42 Assembly details of railway axle and wheel.....	65
Figure 43 Technical drawing of the F3 axle. ....	65
Figure 44 Location of typical fretting cracks on the axle. ....	66
Figure 45 Location of fractographic samples.....	67
Figure 46 Stamped ruler for identification of crack locations .....	68
Figure 47 Circumferential crack maps .....	69
Figure 48 General appearance and locations of the metallographic specimens.....	70
Figure 49 Translation of crack measurements to global cylindrical coordinates.....	71
Figure 50 Technical drawing of the axial fatigue test specimen.....	73
Figure 51 Technical drawing of the torsional fatigue test specimen. ....	74
Figure 52 Rotating beam fatigue test setup.....	74
Figure 53 Axial fatigue test equipment. ....	75
Figure 54 (a)SEM image of specimen surface, (b) defect area machined by WEDM, (c)fatigue crack propagation plane.....	76
Figure 55 Set-up for crack measurement by potential drop technique. ....	77
Figure 56 Strain-controlled fatigue test set-up.....	78
Figure 57 Loading and boundary conditions applied to the wheel-axle assembly. ..	80
Figure 58 Schematic view of the loading on the wheel-axle-rail assembly.....	81
Figure 59 Distribution of von-Mises' stress: (a) press-fitting, (b) static loading.....	83

Figure 60 Stress distributions for the maximum tensile stress loading of axle .....	84
Figure 61 Distribution of surface shear and tensile stresses along the press-fit surface during.....	85
Figure 62 Variation of the compressive stress components caused by applied press-fit during tension and compression cycles of the axle .....	87
Figure 63 Fretting cracks on Axle A (a) and Axle B (b).....	88
Figure 64 Change of stress distributions along the press-fit with friction coefficient: (a) longitudinal stress, (b) shear stress .....	90
Figure 65 Distribution of stresses at the axles section during static loading: (a,b,c) radial (S11), tangential (S22) and longitudinal (S33) stresses and (d,e,f) shear stresses (S12, S13, and S23 respectively).....	92
Figure 66 Cyclic stresses during a loading - unloading cycle .....	93
Figure 67 Proportional and non-proportional loading path at an 18mm distance from S transition.....	94
Figure 68 Initiation regions of fretting cracks. Non-propagating small cracks and propagated major cracks.....	95
Figure 69 Broken line pattern of the cracks: (a) Axle A, (b) Axle B.....	96
Figure 70 Position and propagation direction of fretting cracks on (a) macro scale, (b) micro scale (x150) .....	97
Figure 71 Crack measurements on planes (a) far from the diameter, and (b) close to the diameter. ....	98
Figure 72 Crack maps based on the corrected crack measurements. ....	100
Figure 73 3D distribution of fatigue cracks on the sectioned 30-mm-thick discs...	101
Figure 74 Estimated projection of the circumferential cracks on the axle cross-section. ....	102
Figure 75 Propagation of cracks initiated from different points. ....	103
Figure 76 The major crack angle with respect to the longitudinal axis.....	104
Figure 77 Representative micrographs on (a) transverse, (b) longitudinal plane (550x). ....	106
Figure 78 Sulfur print of the press-fitted sections for (a) axle A, (b) axle B. ....	107
Figure 79 Variation of impact toughness with temperature (longitudinal) .....	108
Figure 80 Cyclic stress- strain curve and monotonic curves for 34CrMo4.....	109
Figure 81 (a) Formation of triangular region between two critical planes of crack propagation, (b) thickness of the deformed layer (8000x) .....	110
Figure 82 Propagating and non-propagating cracks at the material surface .....	111

Figure 83 Debris accumulation inside major crack (x2000). .....	112
Figure 84 Debris accumulation between the crack faces (x4000) .....	112
Figure 85 Deformation and crack initiation at surface asperities (Axle B). .....	113
Figure 86 SEM micrograph showing fretting damage at the surface.....	113
Figure 87 Sub-surface cracking at grain boundaries. ....	114
Figure 88 MnS inclusions intersected by a surface crack. ....	115
Figure 89 Macrograph: rubbing in the damaged section. ....	116
Figure 90 Transition from rubbing to the indications of axial fatigue (x500). .....	117
Figure 91 Crack depth comparisons on (a) the polished surface (b) fracture plane	118
Figure 92 S-N diagram of the 34CrMo4 railway axle material (R=-1) .....	120
Figure 93 S-N diagram of the 34CrMo4 railway axle material (R=0).....	120
Figure 94 Goodman diagram of the normalized 34CrMo4 steel .....	121
Figure 95 Haigh diagram of the normalized 34CrMo4 steel .....	121
Figure 96 Kitagawa diagram (normalized 34CrMo4).....	122
Figure 97 Determination of Dang-Van constants and application of modified locus for the normalized 34CrMo4. ....	124
Figure 98 Dang Van criterion and original locus.at points on the contact area .....	125
Figure 99 Comparison of the allowable crack size along the contact surface according to Dang Van multiaxial fatigue criterion. ....	126
Figure 100 Application of Liu Mahadevan criterion at different locations along the contact area (under the nominal bending stress of 120 MPa). ....	127
Figure 101 Load vs. CMOD graphs for 34CrMo4 at different temperatures .....	128
Figure 102 Fracture surface appearances at (a) room temperature, and (b) -10°C .	129
Figure 103 Fatigue crack growth rate data for 34CrMo4 steel (normalized) .....	130
Figure 104 Variations of stress intensity factors with a crack angle for 110 µm deep cracks (a) maximum applied nominal stress (b) minimum applied nominal stress. ....	132
Figure 105 Distribution of stress intensity factor for 70° degree inclined crack, with a depth of 1600 µm, along press-fit (a) maximum applied nominal stress, (b) minimum applied nominal stress. ....	134
Figure 106 Settlement of the estimated crack and its possible deflection. ....	135



## CHAPTER 1

### INTRODUCTION

#### 1.1. Motivation

After the development of mass production techniques for steel in the mid of 19<sup>th</sup> century, horse-powered freight transportation on wooden tracks has been replaced by railway transportation [1]. Advances in steels have been forced to compensate the increasing demands of society by means of rail transportation. Catastrophic accidents encountered at different stages of railway history have led the development of new techniques for investigation and prevention of component failures. Although the rail failures were reduced by the improvements in steel quality, the axle and wheel failures have been still considered as the most detrimental causes of railway accidents [1]. Earlier efforts in railway research were concentrated on the prediction of limiting conditions of fatigue events caused by repeated loading. Engineering approaches based on the fatigue limit still constitute the basis of axle design procedures according to EN standards [2, 3]. The standard procedures for qualification and manufacturing of axles, wheels, and wheelsets were published in 2003 [4-6].

The sudden increase of railway axle fractures in the USA between 1995 and 2004 was explained by the increased mileage and wagon capacity [7]. The possible solutions to the axle failures are classified as

- Development of axle geometry through finite element analysis
- Determination of load spectra and improving fatigue resistance accordingly
- Increasing the safety level of defect acceptance criteria and NDT frequency
- Increase axle performance with surface and heat treatments
- Selecting axle materials with superior mechanical properties

According to a recent report by European Railway Agency (ERA), the number of broken axles between 2006 and 2009 was reported to be 349 in total [8]. The fatigue failures were due to ballast impact, material defects, corrosion pits, fatigue cracks and paint detachment [9].

Development of damage tolerant design methods and use of new steels are the modern approaches to increase the reliability of the railway axles. Modern hollow axle designs provide 100% detectability of the axles (Figure 1).

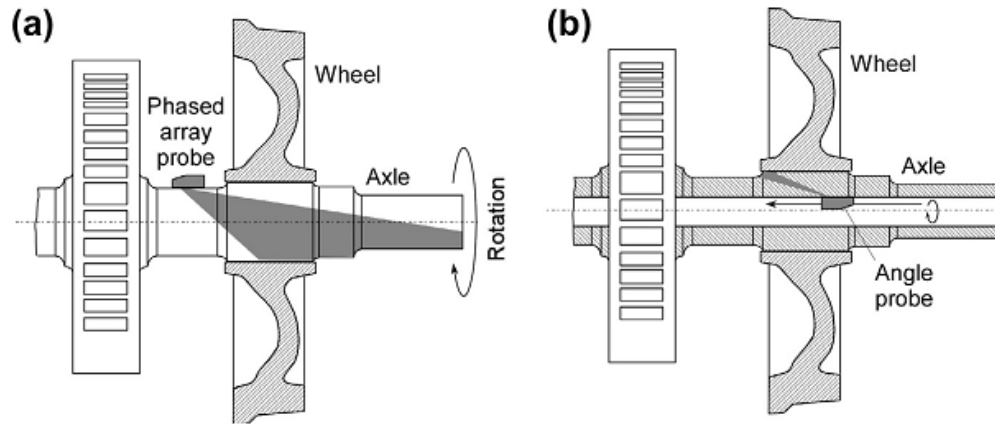


**Figure 1** Ultrasonic inspection: (a) solid axle, (b) hollow axle [8]

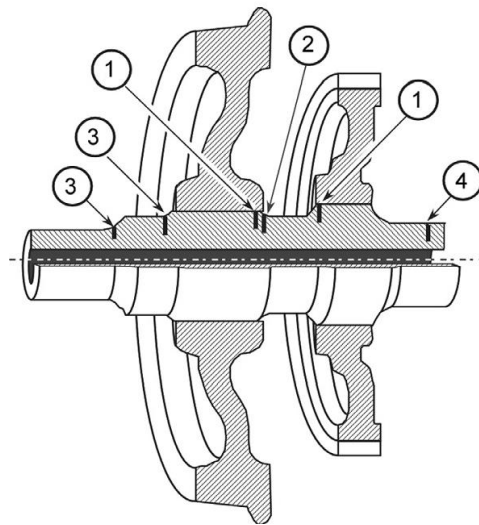


**Figure 2** Typical damage accumulation locations on the railway axles [8]

Failure investigation of the broken or damaged railway axles clearly indicates four common locations for crack initiation (Figure 2). The crack initiation underneath the press-fitted sections is associated with surface damage caused by fretting wear (Figure 2, region 1). Another location is the contact edges (Figure 2, region 2). The material defects or the surface irregularities at this section easily propagate by the influence of

present stress concentration. Failures due to ballast impact and corrosion damage are observed on the axle body which is open to atmospheric conditions and physical damage (Figure 2, region 3 and 4).

Assessment of damage accumulation underneath the press-fitted section constitutes an important issue for the design of railway axles. Unlike the other fatigue failures initiated from a single origin, the fretting fatigue nucleates at several points experiencing the similar multiaxial conditions along the press-fitted surface. Incorporation of individual fretting cracks gives rise the formation of a major circumferential crack which propagates very rapidly [10]. The sudden increase in the fatigue crack propagation rate results in miscalculation of the remaining fatigue life, and thus, premature failure of the axle. Another important consequence is the need for more frequent inspection intervals which means increased operational costs.

A recent survey in Turkish State Railways (TCDD) reported that 89 of 256 examined axles were prematurely cracked between the years 2000 and 2006 [11]. 12 of the identified axles were reported to crack before reaching 75% of their estimated fatigue life (20 years). The remaining 77 were reported to crack within 15 and 20 years. The majority (84%) of the identified cracks was caused by the fretting damage at the press-fit seat (Figure 3 and Figure 4). Furthermore, the fretting fatigue was associated with one particular type of axle geometry (G1 axles) which also verifies the effect of axle design in fretting fatigue assessment.

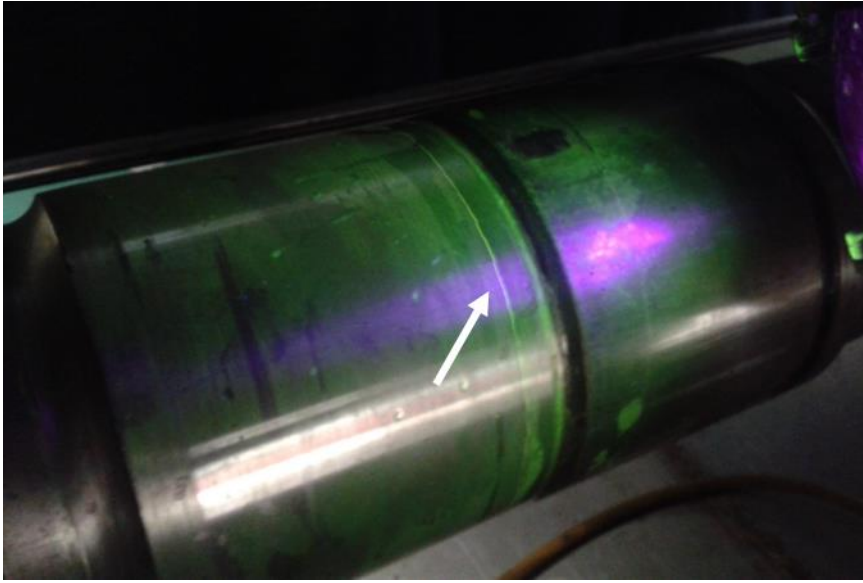


**Figure 3** Circumferential crack under wheel press-fit

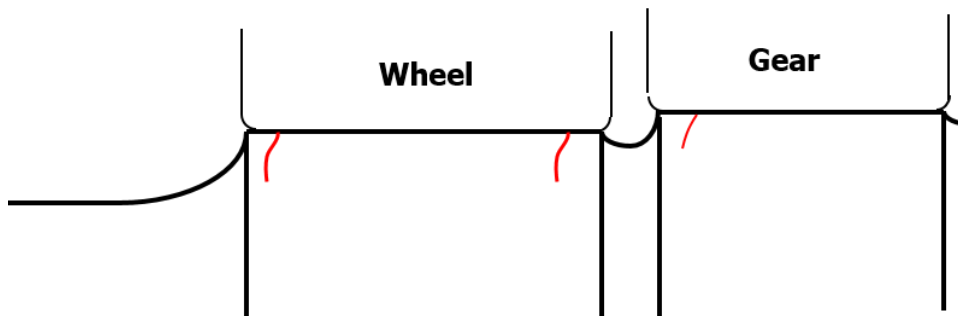


**Figure 4** Typical failure locations inspected at G1 axles (DE24000 locomotives) [11]

The failure of railway axles due to fretting fatigue at the wheel-axle contact still constitutes a problem for railway operators.

## 1.2. Aim and Main Contribution of the Thesis

This thesis aims to develop a numerical prediction procedure for structural integrity assessment of railway axles. The proposed techniques benefit from FE analysis, multiaxial fatigue models, fracture mechanics, and mechanical testing to investigate the possible effects fretting fatigue during design period. The main contribution of the



study is that the presented numerical approach give designers an opportunity to evaluate the possible effects of fretting fatigue and improve their design accordingly before conducting expensive and time-consuming full-scale axle test. Additionally, reduction of total life cost by optimizing defect acceptance criteria and inspection frequency by using the proposed techniques.

The chronic axle failures provided by TCDD were examined to understand the metallurgical basis of the fretting fatigue and check the applicability of the multiaxial fatigue theories to a real axle problem. Fractography and three-dimensional mapping of the full-scale axles, which worked under actual service conditions for 10 to 15 years, provides a valuable representation of uneven fatigue crack propagation and multi-site damage associated with fretting failures.

The study differs from the other studies in literature by considering the effect of metallurgical variables on mechanical phenomena. An extensive description of conditions causing nucleation of fretting fatigue cracks was tried to be given by the fractographic evidence.

Furthermore, fracture mechanics approaches, stress-based multiaxial fatigue models, and short crack threshold conditions were used in combination to increase the prediction ability and cover different aspects fretting fatigue problem.

The problems related to the fretting fatigue of conventional axles in Turkey have remained unsolved since the 1970s. The suggested solutions to prevent fretting fatigue could not be proven due to lack of analytical tools to examine the effect of potential treatments before conducting full-scale axle tests. Consequently, the inspection frequency of the conventional rail axles has been high and the defect acceptance limits are based on the previous experience. The presented methods and experimental data in the study can be utilized in the development of structural integrity assessment strategies of 34CrMo4 railway axles.



## **CHAPTER 2**

### **THEORY AND LITERATURE REVIEW**

#### **2.1. Literature Review**

The premature fatigue failure of the railway axles as a result of environmental damage and contact fatigue is a significant concern that should be followed carefully to sustain structural integrity of railway components. The contact fatigue expressed as the fatigue failures caused by the corrosion, wear or cracking due to repeated loading of contacting bodies [12]. The relative sliding between the bodies causes a partial slip of the contacting surfaces upon direct loading or vibration.

The research on the fretting failure of the railway axles dates back to 1930s [7, 13]. A lot of full-scale axle tests were conducted to understand the effect of geometry, residual stresses, heat treatments, case hardening, surface coating, cold working, material change, shot peening, lubrication and water contact [13]. Results of the expensive and time consuming full-scale tests were utilized in the assessment of structural integrity. Furthermore, the stress calculations on different axle geometries were limited on the numerical models based on experimental studies [7]. The number of axle failures was remarkably reduced after introduction of ultrasonic testing in 1957 and improved further by the use of angle probe in 1963 [14]. However, inspection frequency of the press-fitted wheel axle assembly was made in a conservative manner at the beginning. The modern approach to the wheelset design is to reduce the “Total Life Cycle Cost” which can be achieved by fracture mechanics calculations and determination of fatigue crack threshold conditions through advanced experimental techniques [9]. Sustainability of “damage tolerance” within “safe life” in an economical way is the ultimate objective of the railway industry. The monitoring of structural integrity by using “in-service damage indication systems” is an issue of cost efficiency and safety. The design concepts such as “one million miles axles” are introduced to produce axles with maximized safety [8].

Fretting fatigue of railway axles was extensively studied in the literature.

The fretting fatigue at the sub-surface and the stick-slip interface may be investigated by analytical methods [15, 16]. The prediction of fretting fatigue crack initiation at the notch root, and the contact edge is complex due to stress singularities at these positions [16]. The singularity-aware approaches have been adopted for fretting fatigue assessment of these locations[17].

The use of FEA gives the opportunity to investigate the stress distributions for different geometries and contact parameters without making full-scale axle tests. The calculation of multiaxial fatigue index and stress intensity factors to determine the location and critical size of fretting cracks is frequently studied in the literature [15, 16, 18-21]. A collection of stress data from the fretting-pad tests with digital image correlation (DIC) or photoelasticity is also presented in the literature[10, 22].

The comparison of the strain based multiaxial fatigue models with the experimental data reveals that the most of the applied models are sufficient to calculate the position of fretting crack initiation sites. However, the computed critical crack limits differ from model to model [10, 15, 22]. The applied strain-life models have difficulties in determining the number of cycles for initiation of fretting cracks. Although some models managed to make predictions in terms of percent fatigue life, a remarkable scatter within the obtained data is reported. The scatter of the results of the experimental studies reveal that the fatigue crack initiation by fretting is not only affected by effective stress and strain [23].

Stress-based multiaxial fatigue models are used to aim to determine the effect of high cycle fatigue behavior [24]. Consistent results with experimental data are reported in general [15, 16, 21]. The stress-based models do not consider surface plasticity and are unable to make predictions of the number of cycles for crack initiation but still effectively be used in geometry optimization [18].

The fracture mechanics based approach is also widely utilized in the assessment of fretting crack propagation. The comparison of predicted stress intensity factors with the experimental threshold conditions provide an idea of crack propagation on the full-scale axle [9, 20, 25-27]. The application of Paris –Erdogan equations for prediction

of remaining fatigue life is also presented for the fatigue crack propagation period [10, 15, 22]. Determination of threshold conditions through Kitagawa-Takahashi diagrams was effectively used in both stress and fracture mechanics based estimation of critical crack limits [16, 25].

The experimental investigation of fretting fatigue provides crucial results since the numerical models neglect the environmental, tribologic and microstructural parameters. Fractography of the press-fitted fatigue samples is utilized in investigating the characteristics of fretting fatigue initiation. Rotating beam fatigue tests at different test speeds show how fatigue life is affected by inertial force, oscillation frequency and generated heat at the material surface [21]. Similarly, Kubota et. al. showed the increased rate of fretting crack initiations with the variable stress amplitudes experimentally [28]. Analysis of load spectrum obtained through strain gage placement showed that the fretting cracks nucleated despite the applied stress level below the fretting fatigue limit determined by constant amplitude loading [26].

Experimental studies by Nishioka et. al. investigate fretting fatigue in terms of slip amplitude, fretting mechanisms, mean stress effect, relative slip, contact pressure, surface hardness and test methods [29-34]. The experimental studies show that the fretting crack initiation period consists the majority of fretting fatigue life [19, 22, 23]. Tribologic tests are expressed as the most efficient way to investigate the fretting crack initiation tendency [25].

The axles of the modern high-speed trains are manufactured from high yield strength alloy steels [9]. The aim of this selection is to reduce the unsprung mass to decrease the inertial stresses and provided hollow geometries with 100% probability of detection (PoD) [9, 21]. Fretting fatigue experiments on different axle materials showed that the static mechanical properties and plain fatigue strengths of various axle materials showed no significant effect on the fretting fatigue limits of the press fitted assemblies [13, 27]. However, variations in a number of cycles to fretting crack initiation were shown experimentally [35]. Comparison of the results revealed that the fatigue crack growth rates, short crack threshold stress intensities and fracture toughness were effective to achieve desired “safe life” [20, 26, 35-37].

The possible precautions to the fretting fatigue problem are to retard fretting crack nucleation through the surface coating, case hardening and shot peening [9, 14, 37]. The decrease of fretting fatigue failures between 1974 and 1995 induction hardening of JIS - S38C steel was given in detail [14, 20]. Modifications to the induction and surface finish parameters resulted in eight different processes [14]. The comparison of induction hardened and normalized samples showed that the threshold stress intensity factor for the induction hardened case was twice better ( $6.2 \text{ MPa.m}^{1/2}$  and  $12.6 \text{ MPa.m}^{1/2}$ ) [20]. The difference was associated with the surface residual stresses. The previous results of the shot-peening operations showed a similar effect of surface residual stress on fretting fatigue [13].

Fretting crack prevention by metallic coating presented outstanding results [36, 37]. Surface examination of Mo-coated, and induction hardened surface coatings revealed that the fretting cracks were not visible on the coated sample [36]. The Mo coatings are currently used to prevent fretting fatigue on bainitic 30NiCrMoV12 axles used in Pendolino speed trains [9]. A similar result was achieved by comparison of solely shot-peened and WC-Co coated shot peened surfaces [37]. The numerical analysis of surface stresses showed the applicability of functionally graded material (FGM) coatings to prevent or retard the initiation of fretting fatigue [38].

## **2.2. Fretting Fatigue**

Fretting damage is defined as the surface and sub-surface damage due to repetitive contact loading which is accompanied by surface corrosion and crack nucleation [12, 39]. Surface deterioration caused by the relative sliding between two contacting bodies under normal compressive stress leads nucleation of small fretting cracks, corrosion pits and wear debris [40]. The relative motion may be due to vibration or mechanical loads or both as is the case in the axle fretting problem [12]. Case studies on fretting fatigue of the railway axles show that four positions within the wheel seat are critical initiation of fretting fatigue cracks (Figure 5) [14, 15, 41, 42].

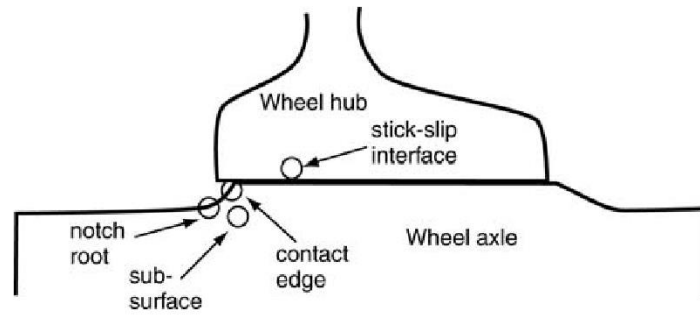


**Figure 5** Critical initiation locations for fretting cracks on railway axles [15].

The fretting fatigue is accompanied with adhesive wear between the surfaces and abrasive wear due to entrapped debris. Practically, the applicability of adhesive wear is limited to the situations where the compressive stress due to normal force ( $N/A_{\text{real}}$ ) is equal or less than three times hardness of the material [43]. Reduced surface roughness may increase the real contact area ( $A_{\text{real}}$ ), and thus the effect of adhesive wear may be reduced.

A schematic representation of fretting is given in (Figure 6).

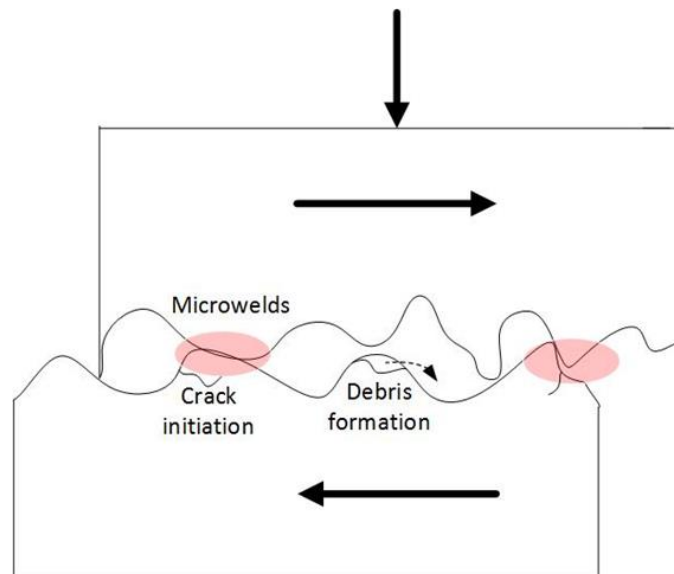


**Figure 6** Fretting damage and adhesion between contact surfaces.

The fretting damage is classified according to the amount of relative motion ( $\delta$ ) and slip [44]. The experimental “fretting maps” are used to classify the severity of the fretting damage (Figure 7).

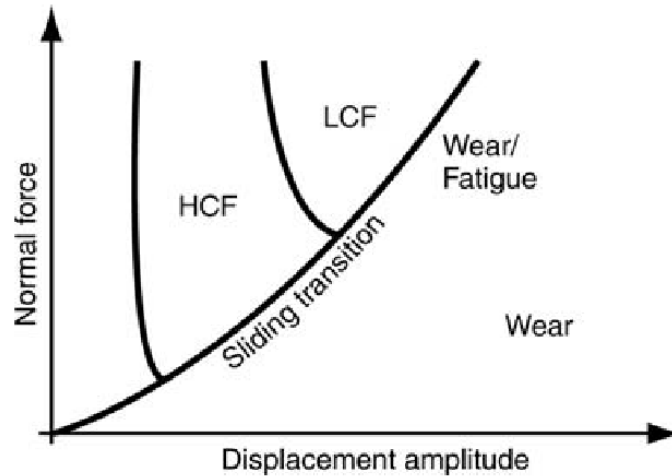


**Figure 7** Fretting map. HCF: high cycle fatigue region, LCF: low cycle fatigue region [15]

Three regimes of fretting are identified based on the fretting maps [44]. The first regime is “the stick regime” where the amount of slip is approximately 3  $\mu\text{m}$ . A small amount of surface damage is observed in the stick regime [44].

The “mixed stick- slip” regime” exists between 3 and 20  $\mu\text{m}$  of slip where a stick-slip behavior is observed. The local “micro welds” between the surface asperities form and cause friction coefficient to increase which is termed as seizure [45]. The amount slip is restricted by the plasticity of the microwelds as fretting proceeds [22]. Failed micro welds may give rise to the debris accumulation and small crack formation (Figure 6).

Gross slip motion more than 20  $\mu\text{m}$  is classified as “fretting wear” while the other two regimes are classified as “fretting fatigue”[44]. Wear is defined as gradual (or progressive) removal of material from the contact surfaces [46]. The extended wear results in failure due to breakage of the surface profile and then the loss of the applied press-fit interference.



### 2.2.1. Initiation of Short Fretting Cracks

The initiation of small fretting cracks is observed as a result of cyclic deformation of the surface layer due to applied shear. A representative sketch of the deformed surface is presented in Figure 8.

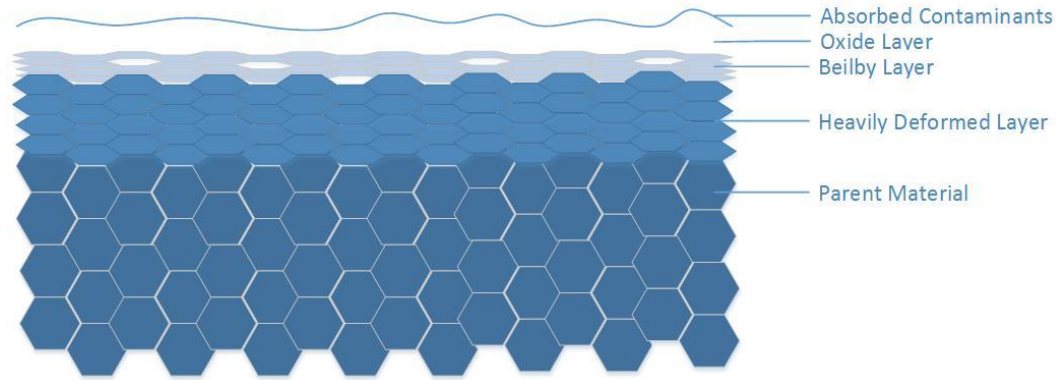


**Figure 8** Layers of surface deformation [40]

The oxide layer is the outermost layer of the material facing the atmospheric effects. Its thickness is typically 0.01-0.1 micron. Beilby layer is a mixture of metallic content and metallic oxides [40], and it is typically 0.1 micron in thickness. The heavily deformed layer is the layer experiencing large plastic deformations due to contact loads [40]. In the case of repetitive loading, cyclic hardening takes place at the heavily deformed layer.

A size comparison between the scale of damaged layer and the typical surface features is given in Figure 9.

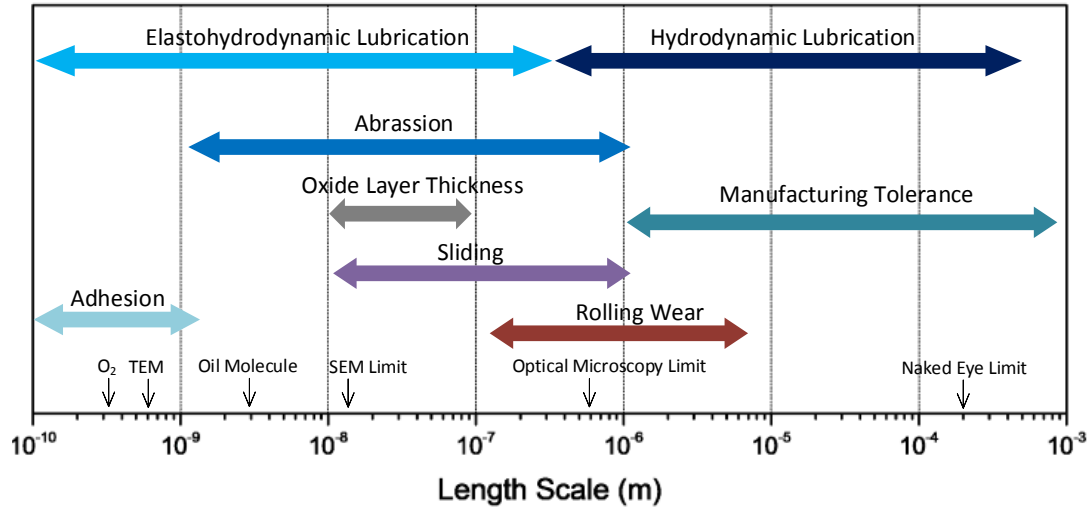


**Figure 9** Scale of surface damage [40, 46]

Initiation phase of the fretting fatigue consists of three stages [10, 47]. The fretting damage starts with the removal of the oxide layer which is followed by the adhesion of surface asperities (microwelds or cold welds) [42]. Upon failure of the micro-welded surface asperities initial accumulation of wear debris is observed and the friction coefficient decreases [30, 48-50].

Plastic deformation and oxidation of near surface zone take place in the second stage where grain-sized fretting cracks appear [10, 49]. Formation of fretting cracks is related to elastic shakedown and ratcheting processes taking place in the heavily deformed layer (Figure 8). A slight strain hardened film forms on the surface. Continuous strain hardening of the surface layer results “ratcheting” or “cyclic creep” at the surface [51]. The heavily deformed layer is also susceptible to initiation of sub-surface cracks.

Small fretting cracks nucleated at different locations merge to form a major crack as fretting proceeds [10, 16]. That is, an accelerated propagation might follow initiation period. It has been reported that fretting fatigue causes to decrease fatigue life up to 60-75% [22, 42]. Furthermore, the results obtained from fretting tests reveal that the majority of the fatigue life is spent during initiation period [50].

In the third stage, the influence of surface stress reduces and the propagation rate controlled by the external bulk stress [10, 15, 16, 22, 24]. Propagation of long cracks, driven by the bulk stress, results in final fracture of the axle as cyclic loading proceeds. The cyclic shear in axle-wheel assembly is accompanied by cyclic bending and torsion stresses. The cyclic deformation path of such a complex loading differs from the uniaxial loading. A more detailed explanation of multiaxial hardening is given here, but the plastic deformation of the surface layer is not examined in the analytic part of the study.

#### 2.2.1.1. *Isotropic Hardening*

At the onset of yielding effective stress ( $\bar{\sigma}$ ) invariant equals to the equation of yield locus stated by the von Mises' equations. Since the effective stress function is an invariant function, it is independent of the loading method.

$$\bar{\sigma} = \frac{1}{\sqrt{2}} \sqrt{(\sigma_x - \sigma_y)^2 + (\sigma_y - \sigma_z)^2 + (\sigma_x - \sigma_z)^2 + 6(\tau_{xy}^2 + \tau_{yz}^2 + \tau_{xz}^2)} \quad (2.1)$$

For a biaxial torsion-tension test where the terms, excluding  $\sigma_x$  and  $\tau_{xy}$ , are zero. Equation 2.1 reduces to the Equation 2.2:

$$\bar{\sigma}^2 = \sigma_0^2 = \sigma^2 + 3\tau^2 \quad (2.2)$$

which represents a circle with a diameter of  $\sigma_0$  centered at the origin of an  $\sigma - \sqrt{3}\tau$  coordinate axes. As the cyclic plastic deformation is repeated, the value of yield stress increases in each cycle (Figure 10), which results in an increment in the radius term expressed in Equation 2.2. In other words, the circle representing yield locus on  $\sigma - \sqrt{3}\tau$  axes expand as cyclic deformation takes place. This expansion due to the hardening is constrained by “elastic shakedown limit.” Once the elastic shakedown state has been achieved isotropic hardening mechanism becomes ineffective.

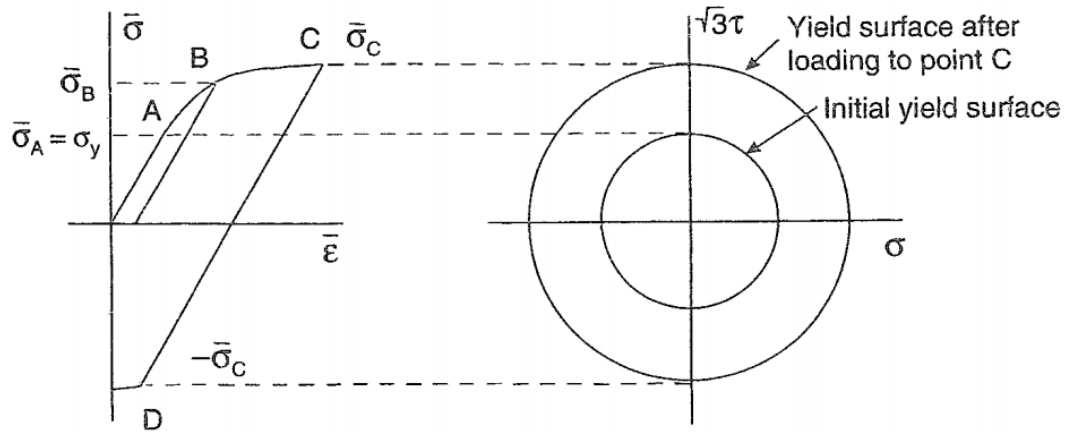


**Figure 10** Schematic explanation of isotropic hardening [24]

#### 2.2.1.2. Kinematic Hardening

For the materials exhibiting Bauschinger effect, the mechanism of cyclic plasticity may be observed in the form of displacement of yield locus without any change in the radius expressed on the  $\sigma - \sqrt{3}\tau$  axes. Translation vector of yield locus is presented by a vector  $\alpha$  (Figure 11).

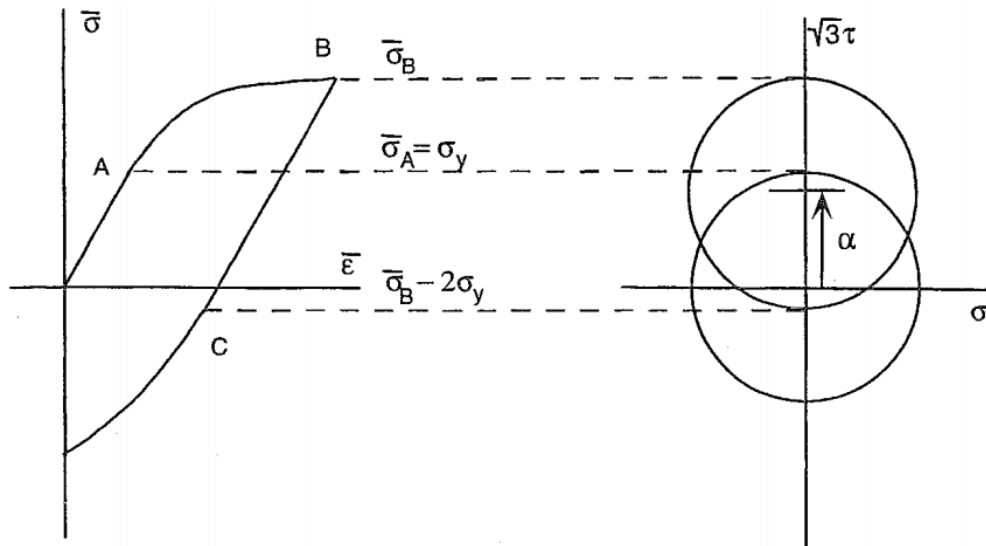


**Figure 11** Schematic explanation of kinematic hardening [24].

The materials are considered to exhibit both kinematic and isotropic hardening. Once the stabilization has been achieved only kinematic hardening is observed.

To discuss the path dependence of kinematic and isotropic hardening, a non-proportional path of tension test was presented in Figure 12. In the example, stress controlled tension-torsion loading has been divided into two paths where a pure torsion loading was applied from Point A to B, then unloaded to point A again. Next, the specimen was loaded to tension from point A to C.

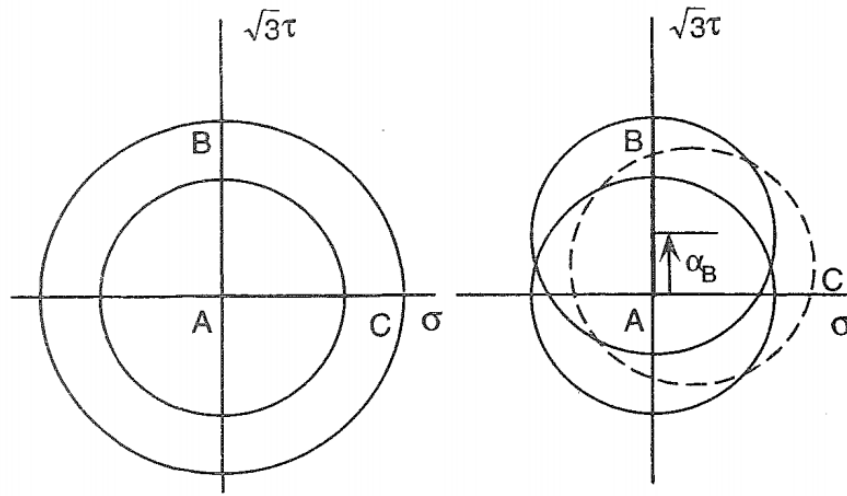


**Figure 12** Isotropic and kinematic hardening during non-proportional loading [24].

The change in yield locus due to proportional and non-proportional loading can be differentiated by comparing Figure 11 and Figure 12.

#### 2.2.1.3. *Ratcheting (Cyclic Creep)*

Ratcheting (or cyclic creep) is defined as the plastic deformation accumulation as a result of mean stress in the cyclic deformation process [24]. For instance, linear plastic strain accumulates when torsional shear is applied to a statically loaded tension bar. In such a case, the rate of plastic strain accumulation may decrease or increase depending on the applied shear strain amplitude and material's microstructure.

In this study, crack initiation due fretting fatigue was investigated. The origin of surface damage resulting in fatigue failure was presented to be due to local ratcheting

caused by the major loading stress accompanied by localized deformation at the contact.

In the case of rail –wheel contact, accumulation of plastic strains due to contact stresses may be stabilized after a few loading cycles. That is, further plastic deformation can be inhibited by the residual stress stored in the form of elastic shakedown. The deformation or load exceeding shakedown limit may lead further plastic deformation known as “ratcheting” (cyclic creep) or “incremental collapse” [12].

#### 2.2.1.4. *Non-proportional Cyclic Hardening*

Non-proportional cyclic hardening can be handled as a combination of the hardening effects discussed until here. Typical  $\sigma - \sqrt{3}\tau$  and  $\frac{\gamma}{\sqrt{3}} - \epsilon$  curves for a non-proportionally loaded tension-torsion bar is presented in Figure 13.

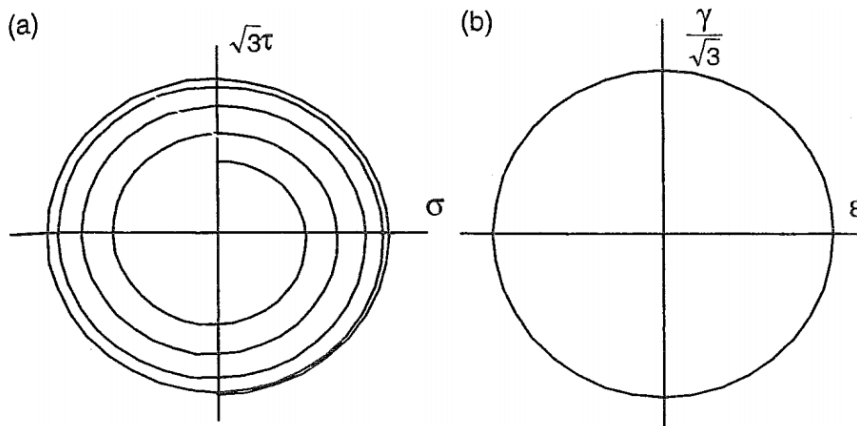


**Figure 13** Non-proportional path of (a) cyclic stress, (b) and strains [24]

The overall difference in cyclic deformation can be presented more clearly in the cyclic stress-strain curve (Figure 14). The magnitude of additional hardening is dependent on the microstructural features of the material and the number active slip systems taking part in plastic deformation.

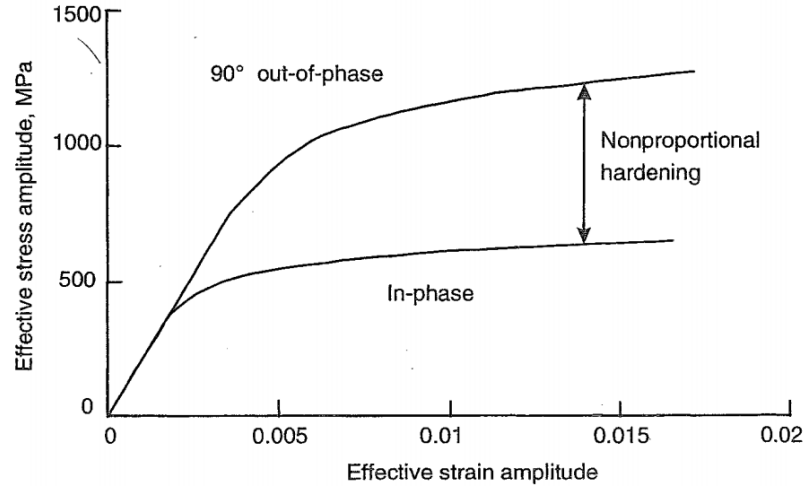


**Figure 14** Cyclic stress-strain curves for proportional and non-proportional hardening [24].

A non-proportional hardening coefficient ( $\alpha$ ) can be defined to express the magnitude of maximum additional hardening due to non-proportional loading [24]. The hardening coefficient can be taken as the difference between the ratio computed at the flat portion of cyclic stress-strain curve and unity. That is, a zero non-proportional hardening would indicate no additional plastic strain due to non-proportional loading path.

In practice, non-proportional loading path can be expressed by an ellipse surrounding close loop of points representing the loading path on  $\frac{\gamma}{\sqrt{3}} - \epsilon$  coordinate axes. A non-proportionality factor (F) can be defined as the ratio of minor and major axes of the corresponding ellipse [24]. A flow rule for such an arrangement can be expressed by Equation 2.3:

$$\bar{\sigma} = K' (1 + \alpha F)(\bar{\epsilon}_p)^{n'} \quad (2.3)$$

where  $\alpha$  is the non-proportional hardening coefficient,  $K'$  and  $n'$  are cyclic plasticity parameters calculated from the cyclic stress-strain curve.

### 2.2.2. Fretting Fatigue Tests

The basic measurement technique for assessment of fretting damage is the fretting pad test. A general schematic of the test setup is given in Figure 15.

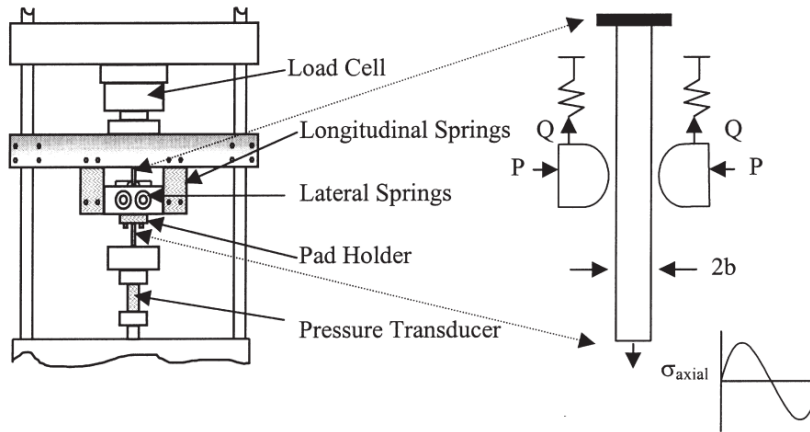


**Figure 15** Fretting pad set-up for fretting tests [19]

In fretting pad technique, a cylindrical or rectangular pad pressure is applied to the specimen. The normal pad pressure is kept constant during the test. The test piece is loaded with fixed displacement and frequency by the aid of a magnetic pulsator up to a certain number of cycles [10, 19, 22].

Comparison tests and fractographic examinations reveal that the fretting pad technique is not a suitable technique for the assessment of the fretting problem encountered in railway axles [9, 15, 16]. Furthermore, the coupon scale testing of the railway axles has been reported not to represent the case in full-scale fretting fatigue [9]. The Minden and Vitry type of test jigs (Figure 16) have been designed to conduct full-scale testing of railway axles [9, 16].





(a)



(b)

**Figure 16** Test jigs for full-scale component test (a) Minden type, (b) Vitry type [16]

### 2.3. Mechanical Investigation of Rail-Wheel- Axle Contact

The stress distribution along the wheel-axle contact has been identified by using the FEM in this study. The mechanical analysis of the wheel-axle assembly is based on the loads and the assembly parameters given by the international standards. Although the practical use of the components is under random dynamic loading, the stress assumption used is based on the static loading under the maximum allowable service condition. The mechanical basis of the contact stresses, stick slip conditions and stress translations in local coordinate systems are given in following sections.

#### 2.3.1. Vertical Contact Stresses

One of the main contributions to surface deformation on the press-fit seat surface is made by the elliptical contact at the wheel-axle assembly. Repetitive deformations caused the normal contact stresses give rise to the nucleation of surface cracks. The

compressive stress at “wheel-axle” contact may be determined as a case of “two-dimensional contact of cylinders” [52, 53]. Static contact between elastic is presented in Figure 17.

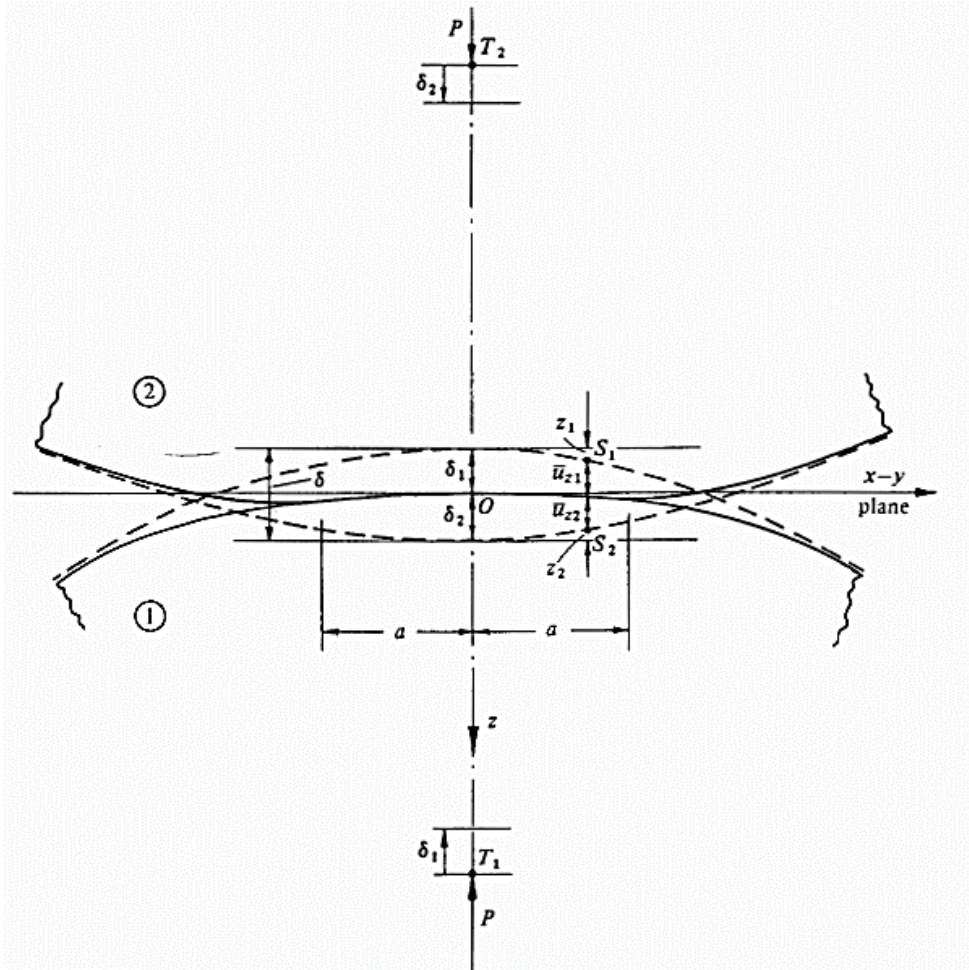


**Figure 17** Contact of elastic cylinders [53].

In the discussion of the 2D problem, two cylinders are in contact due to a vertical compressive load ( $P$ ). The problem is described as the line loading of half space (Figure 17) [53]. Half-width of the line contact is denoted by “ $a$ .” The vertical separation ( $h$ ) between the surface points is described by the sum of distances  $z_1$  and  $z_2$  (Equation 2.4).

$$h = z_1 + z_2 = \frac{1}{2} \left( \frac{1}{R} \right) x^2 \quad (2.4)$$

where

$$\frac{1}{R} = \frac{1}{R_1} + \frac{1}{R_2} \quad (2.5)$$

and  $R_1$  and  $R_2$  are the radii of contacting cylinders.  $u_{z1}$  and  $u_{z2}$  denote the displacement of a contact point. The maximum displacement ( $\delta_1$  and  $\delta_2$ ) is achieved at the contact center.

$$u_{z1} + u_{z2} = (\delta_1 + \delta_2) - \frac{1}{2}(1/R)x^2 \quad (2.6)$$

the pressure distribution is given by the Equation 2.7:

$$p(x) = \frac{2P}{\pi a} (a^2 - x^2)^{1/2} \quad (2.7)$$

At the position of maximum compressive stress ( $x=0$ );

$$p_0 = \frac{2P}{\pi a} = \frac{4}{\pi} p_m = \left( \frac{PE^*}{\pi R} \right)^{1/2} \quad (2.8)$$

where

$$\frac{1}{E^*} = \frac{1}{E_1} + \frac{1}{E_2} \quad (2.9)$$

$P_m$  is the mean pressure, and  $P_0$  is the maximum pressure. Equation 2.10 presents half-width of the contact.

$$a^2 = \frac{4^* P^* R}{\pi E^*} \quad (2.10)$$

### 2.3.2. Press- Fit Stresses

Radial and tangential stress components on the press fitted cylinders are determined in relation with the applied radial interference ( $\Delta$ ). The distribution of surface stress is also affected by the roundness of press-fitted (shrink fitted) cylinders. The maximum interface pressure ( $P$ ) is given by Equation 2.11 [54, 55].

$$\sigma_r = \frac{\Delta}{\frac{D_{I,outer}}{E_{outer}} \left( \frac{D_{O,outer}^2 + D_{I,outer}^2}{D_{O,outer}^2 - D_{I,outer}^2} + \nu_{outer} \right) + \frac{D_{O,inner}}{E_{inner}} \left( \frac{D_{O,inner}^2 + D_{I,inner}^2}{D_{O,inner}^2 - D_{I,inner}^2} + \nu_{outer} \right)} \quad (2.11)$$

where subscripts I and O represents inner and outer cylinders, respectively. The inner diameter of the inner cylinder ( $D_{I,inner}$ ) is zero in the case of solid axles. Tangential stress caused by the inner pressure can be calculated by Equation 2.12.

$$\sigma_{\theta,outer} = \sigma_r \frac{D_{O,outer}^2 + D_{I,outer}^2}{D_{O,outer}^2 - D_{I,outer}^2} \quad (2.12)$$

Likewise, the tangential stress caused by the external forces are given by Equation 2.13.

$$\sigma_{\theta,inner} = \sigma_r \frac{D_{O,inner}^2 + D_{I,inner}^2}{D_{O,inner}^2 - D_{I,inner}^2} \quad (2.13)$$

The stress at the press-fitted axle-wheel assembly is computed by FE analysis in the study. The hand calculations verify the computed stress state.

### 2.3.3. Slip and Stick at the Cylindrical Contact

The partial slip of the wheel on the axle's seat results in fretting. The conforming contact between the wheel and the axle is different from that of a cylinder on a flat surface. But in principle, a similar stick-slip condition exist in the

The elastic contact between a cylinder and a flat surface is expressed by the Hertzian pressure distribution:

$$P(x) = \frac{2P}{\pi a^2} \sqrt{a^2 - x^2} \quad (2.14)$$

Similarly the distribution of the tangential tractions (q) is expressed by Eqn. 1.15:

$$q(x) = \frac{Q}{\pi \sqrt{a^2 - x^2}} \quad (2.15)$$

where Q is the tangential frictional force. The rise of tangential tractions, which goes to infinity at the contact edges ( $x=\pm a$ ), is limited by the finite tangential frictional force  $q=\mu p$ . The high shear stress at the contact rim is relieved by the relative “slip” between

the bodies. Thus a “stick” region, which is balance by the shear deformations, exists in the inner portion of the contact.

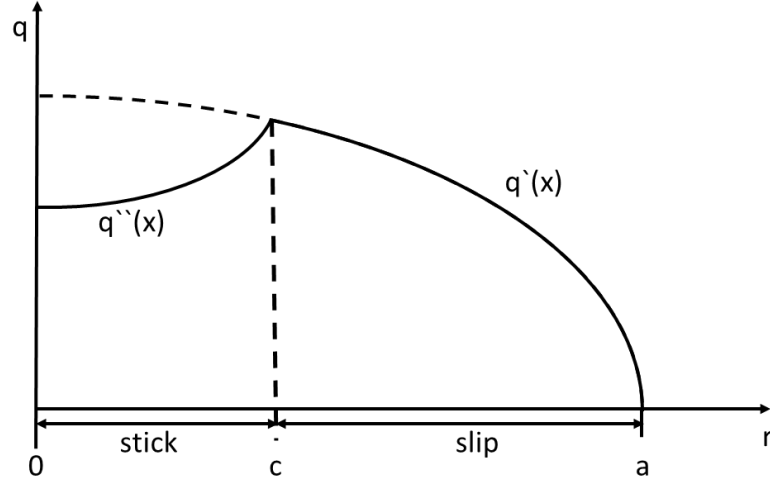


**Figure 18** Tractive rolling contact of similar cylinders [12, 52].

In the full slip, the traction equals to friction force. Traction as a function of distance from contact center in x-direction is given by Amonton’s law [52].

$$q'(x) = \mu p_o \left( 1 - \frac{x^2}{a^2} \right)^{1/2} \quad \text{for } c < |x| \leq a \quad (2.16)$$

where  $\mu$  is the friction coefficient, and  $c$  is the half-width of stick region.

Traction less than limiting force causes a part of the contact to stick. Traction function in such a case is expressed by Equation 2.17 [52].

$$q''(x) = \frac{c}{a} \mu p_o \left[ 1 - \frac{(a+x-c)^2}{c^2} \right]^{1/2} \quad \text{for } -c < |x| \leq c \quad (2.17)$$

Superposition of traction for slip and stick cases are presented in Figure 18 [53]. In the presence of dynamic tractive effort, stick center is dislocated by a distance “d.”

The relation between creepage, d and c is given by the Equation 2.18:

$$d = \frac{\xi a E}{4(1-\nu^2) \mu P_0} \quad (2.18)$$

where  $\xi$  is the “creepage” which is defined as sliding (slip) to roll (stick) ratio applied during motion. Creepage can be expressed as a ratio of relative velocities of the metal surfaces sliding on each other [52].

$$\xi = V_2 - \frac{V_1}{V_m} \quad (2.19)$$

where  $V_1$  is the forward velocity of the first body,  $V_2$  is the velocity of the second body and  $V_m$  is the mean velocity. Tractive force induced on the contact can be computed from the Equation 2.20.

$$T_{effective} = \mu P \left[ 1 - \left( 1 - \frac{\xi E^*}{2\mu P_0} \right)^2 \right] \quad (2.20)$$

After obtaining the contact width and stick region width, the ratio of stick and slip can be obtained from the ratio  $c/a$ . In wear design and analysis, this ratio is considered as the ratio of areas that rolling and sliding take place. Fretting damage observed underneath the press-fit surface is typically located in the proximity of stick-slip boundary [15].

The stick-slip boundary concept can be applied to the stress distribution at the press-fitted wheel-axle assembly. In this study, the stick-slip boundary for the wheel-axle assembly was determined by the finite element modeling. Displacement of the stick-slip boundary with changing friction characteristics is also presented.

#### 2.3.4. Translation of Stress at an Internal Point

Stress state at an internal point is affected by the presence of contact pressure and traction distributed along the surface. To calculate stress at a point, surface load distributions should be divided into a finite number of elements, and the net effect would be the summation of stress tensor from the individual elements. A reference coordinate system to evaluate the distribution of contact forces along contact is presented in Figure 19.

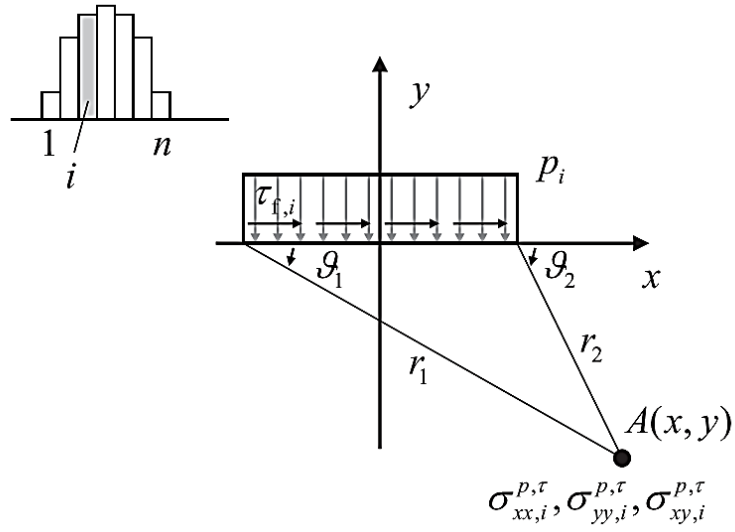


**Figure 19** Coordinates of stress at an internal point [56].

In global coordinates (x-y) stress at an internal point, A(x,y) is expressed by Equations 2.21-2.23 [56].

$$\sigma_{xx,i}^{p,\tau} = -\frac{p_i}{2\pi} \left( 2(\theta_1 - \theta_2) + (\sin 2\theta_1 - \sin 2\theta_2) \right) + \frac{\tau_{f,i}}{2\pi} \left( 4\ln \frac{r_1}{r_2} - (\cos 2\theta_1 - \cos 2\theta_2) \right) \quad (2.21)$$

$$\sigma_{yy,i}^{p,\tau} = -\frac{p_i}{2\pi} \left( 2(\theta_1 - \theta_2) - (\sin 2\theta_1 - \sin 2\theta_2) \right) + \frac{\tau_{f,i}}{2\pi} (\cos 2\theta_1 - \cos 2\theta_2) \quad (2.22)$$

$$\sigma_{xy,i}^{p,\tau} = -\frac{p_i}{2\pi} (\cos 2\theta_1 - \cos 2\theta_2) + \frac{\tau_{f,i}}{2\pi} \left( 2(\theta_1 - \theta_2) + (\sin 2\theta_1 - \sin 2\theta_2) \right) \quad (2.23)$$

A stress term may be added to the identified stress state to include the effect of local residual stress if it exists.

## **2.4. Multiaxial Loading Paths and Multiaxiality Assessment**

To solve the multiaxial fatigue problems, detailed analysis of the loading path has a great importance. First of all, multiaxiality of the problem should be stated, and time-dependent changes of applied stress should be analyzed. Once the stress history has been achieved, static and dynamic features of the applied stress should be identified. Based on the gathered information “proportionality” of the applied stress path is determined.

### **2.4.1. Proportional and Non-Proportional Loading**

Local plastic deformations caused by cyclic loading have an important role in nucleation and propagation of fatigue cracks. The orientation of the maximum shear plane with respect to the materials’ crystallographic orientation affects the ease of dislocation slip, and thus, fatigue crack initiation. On the other hand, strain hardening behavior of the material is a major factor for the non-proportional loading path.

The orientation of the principal planes remains fixed or rotates during multiaxial cyclic loading. The loading regime in which the principal planes (or maximum shear plane) remains fixed is called “proportional loading.” If the orientation of the principal planes rotates with time during cyclic loading “non-proportional loading” takes place. Proportionality of the load path can be assessed by the representation of the stress state on a  $\sigma$ - $\tau$  (or  $\varepsilon$ - $\gamma$ ) diagram. A closed loop represents non-proportional loading while a linear path represents proportional loading (Figure 20).

Non-proportionality can be classified by the proportionality factor (F) which is the ratio of the minor axis to the major axis of the curve enclosing the non-proportional path. The proportionality factor is zero for the proportional case and unity for the 90° out-of-phase loading (Figure 20a and 8b).



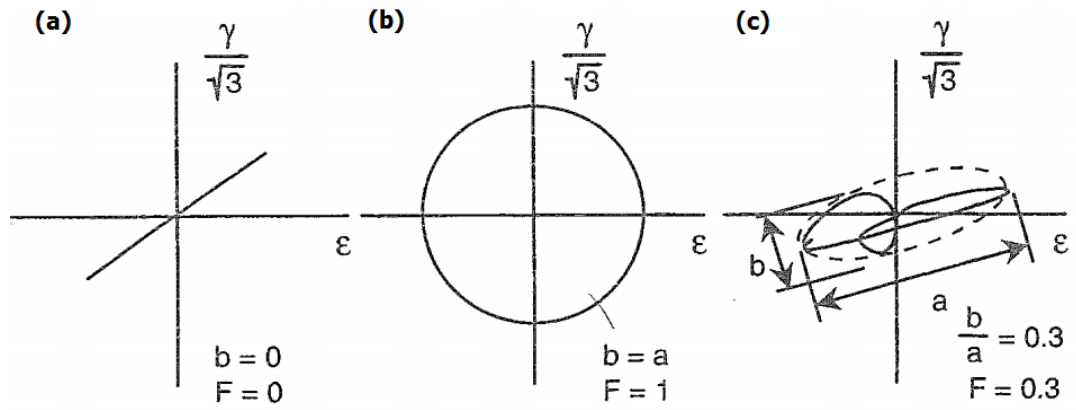


**Figure 20** Loading paths and non-proportionality factor (F) (a) proportional loading, path, (b) and (c) non-proportional loading path [24].

#### 2.4.2. In-Phase and Out-of-Phase Loading

A general representation of “in-phase” and “out-of-phase” loading paths, used to describe loading history of sinusoidal and triangular waveforms, is given in Figure 21.

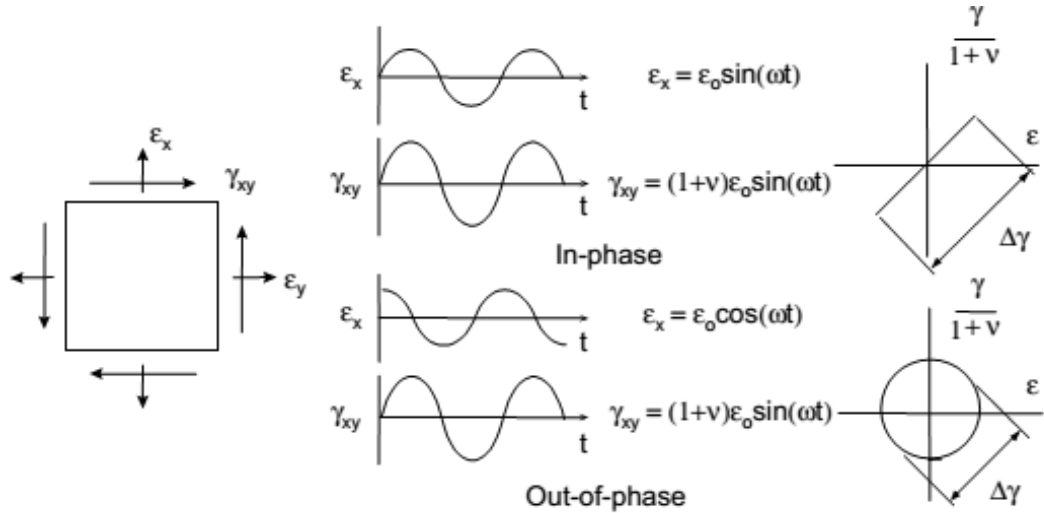


**Figure 21** In-phase and out-of-phase loading [24].

An application of tension-torsion load cycle has been demonstrated in Figure 21. In-phase loading of tensile and shear stresses follows a linear “proportional” path while “out-of-phase” loading of the same stresses is represented by a “non-proportional”

path. Cyclic plasticity, fracture mechanisms and microstructural dependence of the fatigue damage are all affected by the proportionality of the loading path.

In this study, the load paths were identified based on the data obtained from the finite elements analysis. Additional features such as friction, interference and residual stress were implemented to the FE model. The stress distribution along contacts exposed to rolling contact fatigue or fretting damage was identified. Stress tensor obtained at the maximum and minimum nominal stress moments were introduced to a numerical model of the stress state to investigate proportionality, phase, mean, amplitude and the ratio of loading cycle.

## **2.5. Multiaxial Fatigue**

The accumulation of fatigue damage due to repeated loading and its relations with crystal structure through slip mechanism was presented in the earlier stages of fatigue research [16]. Repetitive deformation of grains on the surface which are positioned at angles of the maximum resolved shear stress leads the formation of initiation points during proportional loading [43]. That is, slip takes place at certain orientations. In the case of non-proportional loading, crack initiates at multiple angles due to the rotating maximum shear plane [24]. In other words, the life spent in nucleation, growth and fracture stages becomes path dependent [10, 15, 19, 22]. This section includes the discussion of the growth mechanism of the cracks developing under the influence of multiaxial loading.

### 2.5.1. Modes of Failure in Fatigue Loading

Three modes of failure and their representation on uniaxially tested specimens are presented in Figure 22.

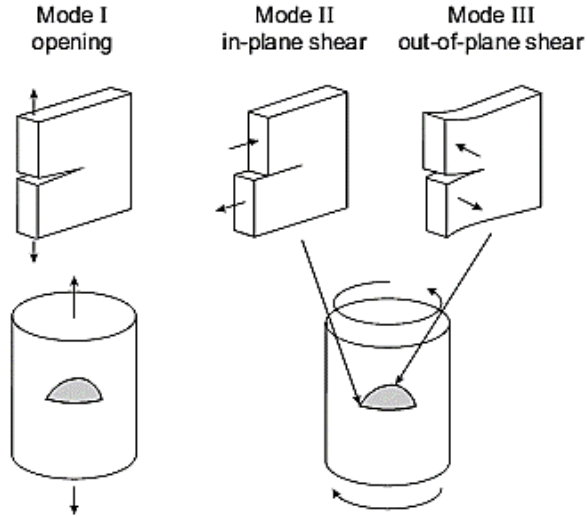


**Figure 22** Modes of failure and crack propagation paths under uniaxial loading [24].

Out of plane shear (Mode III) is active at the maximum depth of semi-elliptical crack while the in-plane shear (Mode II) is observed at the specimen surface. In the torsion case presented in Figure 22 propagation direction is in the radial direction for Mode III while Mode II propagation is in the circumferential direction. In practice, surface cracks under the influence of Mode II are considered as “low aspect ratio” cracks which are shallow in depth [24]. Circumferential fretting cracks found in railway axles are classified in this type.

Crack propagation due to the shear component of applied stress is examined as “in-plane” and “out-of-plane” cases (Figure 23).

In Case A, crack propagation is “in-plane shear propagation” which is parallel to the crack length with no component causing propagation in depth direction. Conversely, in Case B “out of plane shear” acts in the direction of depth in which the intrusion-extrusion type of fatigue damage is observed.

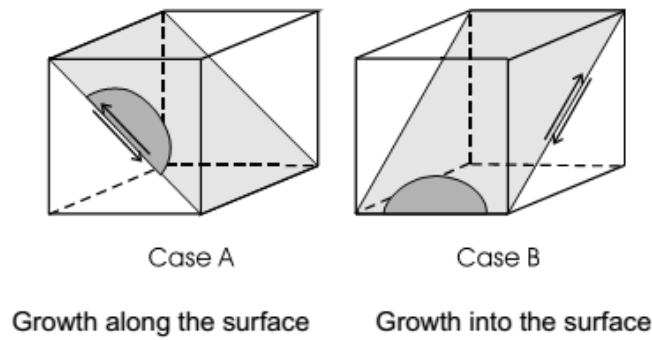


**Figure 23** Two different cases of crack propagation [24].

### 2.5.2. Small Cracks

At the earlier stages the crack growth is dependent on the crack size, crack closure and microstructure [24]. Cracks with dimensions comparable to grain size or interparticle spacing are classified as “small cracks.” Small crack propagation is primarily controlled by the micromechanical effect of major applied stress (Figure 24, Stage I). As propagation proceeds applied fracture, mode governs the propagation process (Figure 24, Stage II) [15, 24]. The transition between different stages of crack propagation can be identified by investigation of the crack path [57]. A deviation in the propagation angle is observed upon transition from stage I to stage II (Figure 24).

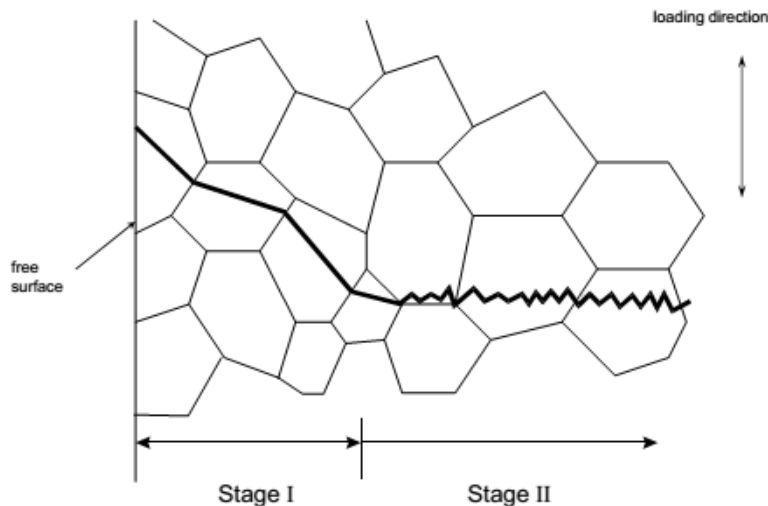


**Figure 24** Stages of crack propagation under uniaxial cyclic stress [24].

Propagation rates of small cracks are higher than those of the large cracks [24, 58]. In the cases of multi-site surface damage (MSD), rapid linking of small surface cracks is observed. Reduction in fatigue life up to 60% was reported for the cases of fretting [10].

Kitawaga-Takahashi diagrams are drawn to present effect of initial defect size on fatigue (endurance) limit of a certain material [59]. The general appearance of Kitagawa diagrams is shown in Figure 25. Reduced fatigue limit due to the presence of allowable size of defects is presented in Kitagawa diagrams.

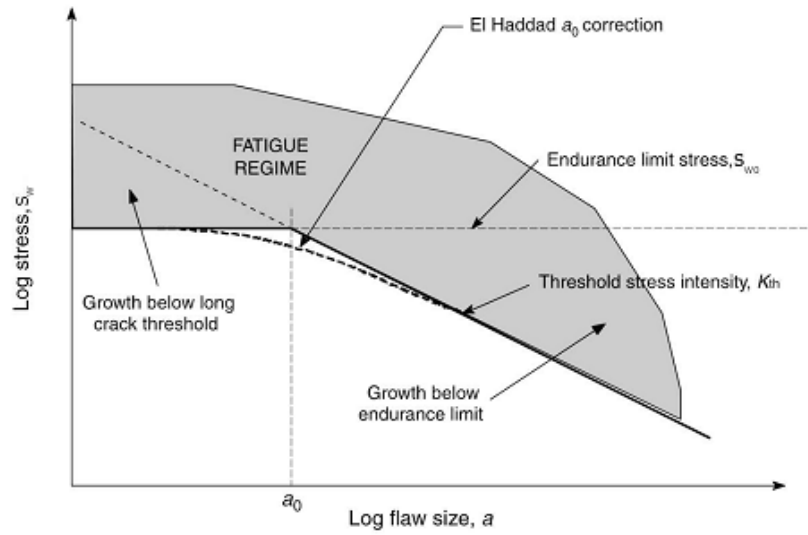


**Figure 25** Kitagawa - Takahashi Diagram [60].

El-Haddad et. al. introduced a numerical approach, known as “El-Haddad correction,” to model the effect of small cracks presented by Kitagawa diagram [61].

El-Haddad correction curve is expressed by the Equation 2.24

$$\Delta S_w = \Delta S_{w0} \left( \frac{a_0}{a + a_0} \right)^{1/2} \quad (2.24)$$

where  $\Delta S_{w0}$  is the fatigue limit of the unnotched specimen and  $\Delta S_w$  is the fatigue limit for the notched specimen. For Mode I loading the intensity factor at the onset of long crack propagation (for  $a > a_0$ ) can be related to  $\Delta K_{th}$  (Equation 2.25)

$$\Delta K_{th} = \Delta S_{w0} F \sqrt{\pi a} \quad (2.25)$$

where  $F$  is the geometrical factor. Besides, it may be concluded that  $\Delta K_{th}$  becomes a size dependent threshold for small cracks [62].

Crack size is considered in terms of “the square root of effective area” of the very shallow surface crack (Equation 2.26)

$$\sqrt{area} = c\sqrt{10} \quad (2.26)$$

where  $c$  is 2D crack length [63, 64].

Considering the flaw size in  $\sqrt{area}$  parameter, the Equation 2.24 can be rearranged to calculate the fatigue limit with a small surface defect ( $\Delta S_w$ ).

$$\Delta S_w = \Delta S_{w0} \left( \frac{\sqrt{area_0}}{\sqrt{area} + \sqrt{area_0}} \right)^{1/2} \quad (2.27)$$

## 2.6. Multiaxial Fatigue Models

Multiaxial fatigue models are developed to assess the overall effect of loading path and calculation of fatigue index which is comparable to the uniaxial experimental data.

In general approach, the main objective of the presented analytical models is to identify the regions that are susceptible to crack initiation, characterize the severity of the damage. The results obtained from the analysis is combined with the experimental data to identify the number of cycles spent in nucleation period and its percentage in total fatigue life of the tested material [19, 22, 23].

In practical application, the selection of the suitable multiaxial fatigue model defining the aspects of multiaxial fatigue damage is essential. Comparison of the results obtained from different models for a certain material is presented in the literature [10, 15, 16, 19, 22, 23, 65].

Multiaxial fatigue models are classified according to the theoretical basis [24]:

- Stress- Based Models
- Strain-Based Models
- Energy-based Models
- Fracture Mechanics Models

Considering the high cycle applications where the applied stress is near and below the fatigue threshold, the stress based and fracture mechanics-based models were used in this study. Application of strain and energy- based models was reported to be more suitable for the low-cycle fatigue applications where the applied loads are in the range of plastic deformation [24]. Besides, application of the strain based models requires assessment of strain-life record of the tested materials in the plastic range.

### 2.6.1. Stress-Based Models

Description of a safe-life envelope for the applied stress is aimed in the stress-based model. The index values defined by the applied model is compared with the uniaxial fatigue limits of the tested material.

#### 2.6.1.1. Critical Stress Approach

##### 2.6.1.1.1. Gough

The observations of Gough model is based on the experimental bending and torsion test conducted on different types of materials [66, 67]. In this model application of plain fatigue data into the relation given in Equation 2.28 and 2.29

$$\frac{f^2}{b^2} + \frac{q^2}{t^2} = 1 \quad (2.28)$$

$$\frac{q^2}{t^2} + \frac{f^2}{b^2} \left( \frac{b}{t} - 1 \right) + \frac{f}{b} \left( 2 - \frac{b}{t} \right) = 1 \quad (2.29)$$

where  $f$  is the bending stress,  $b$  is the bending fatigue limit,  $q$  is the shear stress, and  $t$  is fatigue limit in torsion.

#### 2.6.1.1.2. Sines

The difference between Sines and Gough criteria is that the Sines criterion considers octahedral shear stress to express an average value for the shear stresses acting on the slip planes [68, 69]. In Sines model, the limiting criterion is “the critical resolved shear stress” for a single grain [24, 43]. As a result of experimental studies with different combinations of static and dynamic torsion, bending and axial stresses the hydrostatic component of applied stress is concluded to have an effect on fatigue life [69]. The locus of safe life has been expressed by the Equation 2.30.

$$\frac{\Delta\tau_{oct}}{2} + \alpha(3\sigma_h) = \beta \quad (2.30)$$

The constants  $\alpha$  and  $\beta$  are the material constants which can be determined by uniaxial tests at two different loading conditions.

#### 2.6.1.2. *Critical Plane Approach*

##### 2.6.1.2.1. Findley

Findley model proposes the influence of normal stress on a shear plane [70, 71]. The difference of the model from Sines and Gough models is that Findley model seeks for any shear plane where the maximum value of the damage parameter presented in Equation 2.31 is maximized. This type of approach is termed as “critical plane approach” while Sines and Gough represent “critical stress approach.”

$$\left( \frac{\Delta\tau}{2} + k\sigma_n \right)_{\max} = f \quad (2.31)$$

Where  $k$  is a constant that can be found by conducting torsional and pure bending (or axial) tests at two different stress states. Solutions for the Findley equation for various loading cases can be found in [24].



#### 2.6.1.2.2. Matake

Matake model is another critical plane model which is very similar to Findley model. The underlying assumption of this model is that the multiaxial fatigue is the most severe on a critical plane where the shear and normal stress amplitudes are maximized [72]. The Matake model is expressed by Equation 2.32

$$\frac{\Delta \tau_{\max}}{2} + k \sigma_{n,\max} = \beta \quad (2.32)$$

#### 2.6.1.2.3. Mc Diarmid

Mc Diarmid model based on the analysis of the several high cycle data proposes a critical plane model seeking for the planes where maximum shear stress amplitude and maximum normal stress amplitude coincides (or maximized) on the same plane [73, 74]. The index for Mc Diarmid model is expressed by Equation 2.33.

$$\frac{\Delta \tau_{\max}}{2t_{A,B}} + \frac{\sigma_{n,\max}}{2\sigma_{uts}} = 1 \quad (2.33)$$

where  $t_{A,B}$  is the shear fatigue strength for Case A and B types of cracking.

The main difference between Findley and Mc Diarmid models is that the Mc Diarmid model seeks for a plane where the shear and normal stress amplitudes are maximized; not for the plane where the sum of the shear and normal stress is maximized. The main disadvantage of both models is that they are not applicable to the cases where the normal stress is compressive.

#### 2.6.1.2.4. Liu – Mahadevan

Liu-Mahadevan model is a critical plane model based on the idea of maximized multiaxial fatigue index. The index is expressed by Equation 2.34.

$$\sqrt{\left(\frac{\sigma_{a,c}}{f_{-1}}\right)^2 + \left(\frac{\tau_{a,c}}{t_{-1}}\right)^2 + \left(\frac{\sigma_{a,c}^H}{f_{-1}}\right)^2} = \beta \quad (2.34)$$

where the subscript “a,c” denotes the amplitude in a specific plane and the terms  $f_{-1}$  and  $t_{-1}$  are the bending and torsion fatigue strengths in reversed loading, respectively. Different from the other critical plane models considering the maximum normal stress amplitude Liu-Mahadevan model seeks for a critical plane which is described with respect to the normal vector indicating the plane of maximum principal stress and maximum shear amplitude[75]. The critical plane angle ( $\alpha$ ) is the angle between the normal vector of fatigue fracture plane, which experiences the maximum normal stress amplitude, and a vector which is orthogonal to both of maximum principal stress plane normal and maximum shear amplitude vector.

Based on the experimental data the correction terms are described for the Liu-Mahadevan model [75]. A general form of corrected multiaxial fatigue parameter is presented in Equation 2.35

$$\frac{1}{\beta} \sqrt{\left[ \sigma_{a,c} \left( 1 + \eta \frac{\sigma_{m,c}}{f_{-1}} \right) \right]^2 + \left( \frac{f_{-1}}{t_{-1}} \right)^2 (\tau_{a,c})^2 + k (\sigma_{a,c}^H)^2} \leq f_{-1} \quad (2.35)$$

where  $\eta$  is a material parameter which can be calibrated by uniaxial fatigue tests with mean stress. Alternatively, the relations presented in Equations 2.36 and 2.37 can be used.

$$\eta = \frac{3}{4} + \frac{1}{4} \left( \frac{\sqrt{3} - \frac{f_{-1}}{t_{-1}}}{\sqrt{3} - 1} \right) \quad \left( \frac{t_{-1}}{f_{-1}} \leq 1 \right) \quad (2.36)$$

$$\eta = 1 \quad \left( \frac{t_{-1}}{f_{-1}} \leq 1 \right) \quad (2.37)$$

$k$  and  $\beta$  are material properties which are described in Table 1. An extended version of Liu – Mahadevan model was used in this study.

**Table 1** Material parameters for fatigue damage evaluation [75]

Material Property	for $s = \frac{t_{-1}}{f_{-1}} < 1$	for $s = \frac{t_{-1}}{f_{-1}} > 1$
$\alpha$	$\cos(2\alpha) = \frac{-2 + \sqrt{4 - 4(1/s^2 - 3)(5 - 1/s^2 - 4s^2)}}{2(5 - 1/s^2 - 4s^2)}$	$\alpha = 0$
k	$k = 0$	$k = 9(s^2 - 1)$
$\beta$	$\beta = [\cos^2(2\alpha)s^2 + \sin^2(2\alpha)]^{1/2}$	$\beta = s$

### 2.6.1.3. Mesoscale Approach Models

Mesoscale approach models are described as the models that consider the fatigue problem in a scale which is comparable to grain structure of the materials [76]. The term “mesoscale” can be regarded as the size scale which is larger in crack tip singularity and smaller than a few grain size. The most important feature of the mesoscale approach is that the fatigue loads caused by the major stress are transformed and evaluated in problem coordinates with respect to the crystallographic directions of the individual grains [76].

#### 2.6.1.3.1. Dang - Van

The main proposal of Dang-Van criterion is the fact that nucleation of the fatigue cracks originates from the slip bands formed at the locality of plastically deformed grains [24]. In microscale shear component of applied stress is responsible for the plastic deformation where the hydrostatic component of the stress is in charge of volumetric expansion and compression [43]. The basis of the Dang Van model is nucleation of a fatigue crack at intragranular slip bands. According to Dang-Van criterion fatigue crack nucleation is related to shear and hydrostatic components of microscopic stress applied on grain. The shear component accounts for the formation of intragranular slip band formation [24].

To apply Dang-Van model translation of macro-stress into a micro-stress level is necessary.

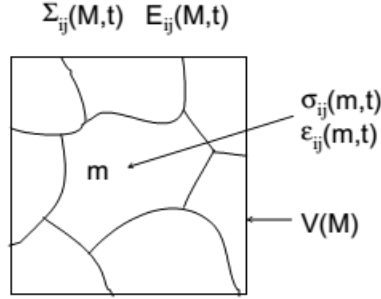


**Figure 26** :Macro and micro stresses as a function of time on a volume  $V(M)$  [24].

In the mesoscopic level, Dang Van model suggests a criterion based on the linear relation of shear and deviatoric components of applied micro stress (Equation 2.38).

$$\tau(t) + a\sigma_h(t) = b \quad (2.38)$$

where  $\tau$  and  $\sigma_h$  are shear and hydrostatic components of micro-stress tensor and  $a$  and  $b$  are the Dang-Van constants.

Mesoscopic stress tensor can be computed by translation of the macroscopic stress tensor. However, primarily the stabilized residual stress tensor ( $\rho^*$ ) after reaching elastic shakedown limit should be calculated.

$$\sigma_{ij}(t) = \Sigma_{ij}(t) + dev\rho^* \quad (2.39)$$

where  $\Sigma_{ij}$  is the macro-stress tensor and  $dev\rho^*$  is the deviatoric part of the stabilized residual stress tensor. In application  $\rho^*$  tensor can be approximated to the vector between origin and stress-path origin on principal stress coordinate system. Consideration of this tensor introduces plasticity consideration to the analysis. With this property, Dang Van model is differentiated from the other stress-based models.

Shear component of the microscopic stress can be related to the tensile material properties and implemented in the fatigue criterion through Tresca maximum shear stress criterion [24, 43].

$$\tau(t) = \frac{1}{2} [\sigma_1(t) - \sigma_3(t)] \quad (2.40)$$

In the perspective of engineering practice, Dang Van criterion could be used to define multiaxial fatigue envelope by using Equation 2.38(Figure 27). Dang Van constants (a and b) could be solved at least two uniaxial fatigue tests (axial or shear) for certain materials.

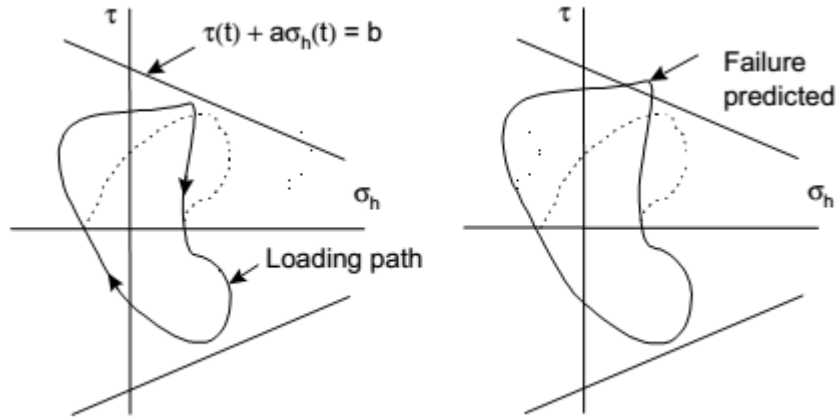


**Figure 27** Limiting curve for Dang Van failure criteria [24].

#### 2.6.1.3.2. Correction for Dang-Van Model

It was reported that the application of Dang Van criterion on non-proportional path contain some errors because the model computes shear on different planes at each time frame due to rotation caused by non-proportionality [24]. Since the normal stress is invariant, the computation of the resultant shear amplitude needs some correction. Dang Van has proposed “the minimum circumscribed circle” method, and its modification by Papadopoulos is used to define the maximum and mean shear amplitudes [47, 77]. This method was applied for the proportional loading in the study.

## 2.7. Crack Propagation

Controlling initiation, growth, and accumulation of cracks along the load carrying structure constitutes the basis of damage tolerant design. Identification of propagating cracks before reaching the critical size is essential for safety and structural integrity.

For this reason, the definition of the critical condition for rapid crack propagation and its convenience for monitoring during service is aimed at the design stage.

### 2.7.1. Basic Concepts

During deformation of brittle materials mechanical energy introduced to the system is considered to be dissipated by the creation of fracture surfaces and elastic strain energy (Griffith's theory of brittle fracture) [43].

$$\frac{d\Delta U}{da} = 0 = \frac{d}{da} \left( 4c\gamma_s - \frac{\pi a^2 \sigma^2}{E} \right) \quad (2.41)$$

where  $\Delta U$  is the increment in energy term, and  $a$  is the crack size. The  $\gamma_s$  term is the surface energy of the crack plane. In the equation, the first term is related to energy dissipated by surface energy where the second term represents energy dissipated as elastic strain energy.

For the plane strain condition, Griffith's theory is presented by the Equation 2.42.

$$\sigma = \left[ \frac{2E\gamma_s}{(1-\nu^2)\pi a} \right]^{1/2} \quad (2.42)$$

In the case of metallic materials energy stored in the form of plastic strain energy is included additionally [78].

$$\sigma_f = \left[ \frac{2E(\gamma_s + \gamma_p)}{(1-\nu^2)\pi a} \right]^{1/2} = \left( \frac{E\gamma_p}{a} \right)^{1/2} \quad \text{since } \gamma_p \gg \gamma_s \quad (2.43)$$

Concept of “elastic strain energy release rate ( $G$ )” is introduced by the Irwin Theory [79],

$$\sigma_f = \left( \frac{EG_c}{\pi a} \right)^{1/2} \quad (2.44)$$

### 2.7.2. Calculation Elastic Strain Energy Release Rate (G)

For high strength materials exhibiting limited plasticity, the slope of the linear relationship between applied load and displacement decreases as crack advances (Figure 28).

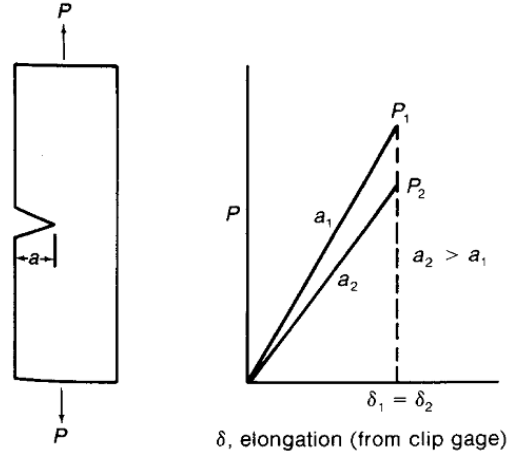


**Figure 28** Change in compliance with increasing physical crack size [43].

The rate of decrease in the slope (or increase in the compliance) can be related to the rate of change in the energy of the system, and thus, to the elastic energy release rate. Energy stored in the system is the area under load – displacement curve.

$$U = \frac{1}{2} P \delta = \frac{P^2}{2m} \quad (2.45)$$

where  $m$  is the slope of the load – displacement curve. Since energy is conserved in fracture process

$$G = \left( \frac{\partial U}{\partial a} \right)_{\delta} = -\frac{1}{2} P^2 \frac{\partial \left( \frac{1}{M} \right)}{\partial a} \quad (2.46)$$

Equation 2.46 shows the dependency of the elastic energy release rate to the compliance change.

### 2.7.3. Calculation of Stress Intensity Factor

Representation of stress field around a crack tip singularity, expressed in cylindrical coordinates, for the plane stress condition is given by Equation 2.47 - 2.49.

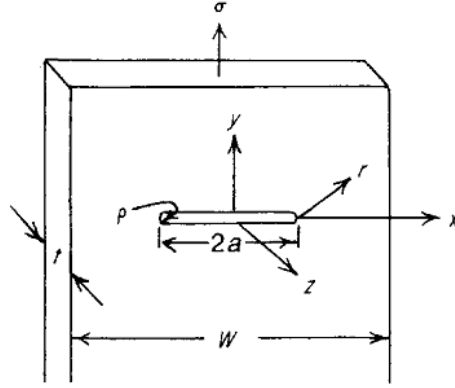


**Figure 29** Stress field around crack tip [43].

$$\sigma_x = \sigma \left( \frac{a}{2r} \right)^{1/2} \left[ \cos \frac{\theta}{2} \left( 1 - \sin \frac{\theta}{2} \sin \frac{3\theta}{2} \right) \right] \quad (2.47)$$

$$\sigma_y = \sigma \left( \frac{a}{2r} \right)^{1/2} \left[ \cos \frac{\theta}{2} \left( 1 + \sin \frac{\theta}{2} \sin \frac{3\theta}{2} \right) \right] \quad (2.48)$$

$$\tau_{xy} = \sigma \left( \frac{a}{2r} \right)^{1/2} \left[ \cos \frac{\theta}{2} \sin \frac{\theta}{2} \sin \frac{3\theta}{2} \right] \quad (2.49)$$

The stress tensor for the  $(r, \theta)$  coordinate system is proportional to the product of applied normal stress ( $\sigma$ ) and the square root of crack size ( $a$ ). This proportionality in local stress is called “stress intensity” [43, 79].

$$K = \sigma \sqrt{\pi a} \quad (2.50)$$

Then, Equations 2.47-2.49 become

$$\sigma_x = \frac{K}{\sqrt{2\pi r}} \left[ \cos \frac{\theta}{2} \left( 1 - \sin \frac{\theta}{2} \sin \frac{3\theta}{2} \right) \right] \quad (2.51)$$

$$\sigma_y = \frac{K}{\sqrt{2\pi r}} \left[ \cos \frac{\theta}{2} \left( 1 + \sin \frac{\theta}{2} \sin \frac{3\theta}{2} \right) \right] \quad (2.52)$$

$$\tau_{xy} = \frac{K}{\sqrt{2\pi r}} \left[ \cos \frac{\theta}{2} \sin \frac{\theta}{2} \sin \frac{3\theta}{2} \right] \quad (2.53)$$



Stress intensity at the crack tip goes to infinity as radius term approaches zero. A geometrical factor (Y), dependent on crack size and geometry, is defined to solve crack tip singularity problem (Equation 2.54).

$$K = Y\sigma\sqrt{\pi a} \quad (2.54)$$

Case specific geometry factor and stress intensity factor can be expressed as parametric equations in the form of weight function solutions or basic relations presented in handbooks [63, 80, 81]. Determination of stress intensity factors through finite element analysis (FEM), photoelastic methods (PE), strain gauge (SG) measurements and digital image correlation (DIC) are also possible [82, 83].

Depending on the type of loading in the uniaxial system stress term ( $\sigma$ ) in “stress intensity factor” expression becomes dependent on crack opening mode (Figure 30).

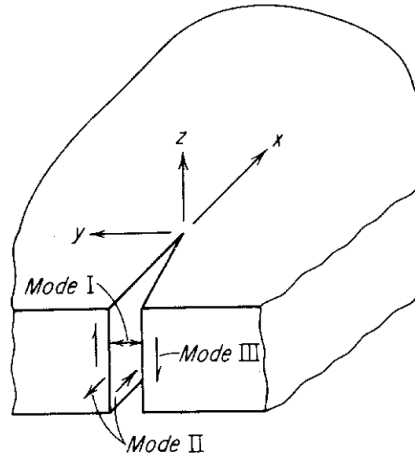


**Figure 30** Modes of crack propagation and tearing on a minute crack [43]

The critical value of the elastic strain energy release rate ( $G_c$ ) at the onset of fracture is related to the critical value of stress intensity factor that is termed as the “fracture toughness” ( $K_c$ ) for high strength materials.

Rearranging the Equation 2.44

$$G = \frac{\pi a \sigma^2}{E} \quad (2.55)$$

The numerator of the equation equals the square of stress intensity factor (K) defined for the plane stress case. Considering the compatibility relations for plane stress and plane strain equations of K-G relation can be derived as follows [43, 84].

$$\text{for plane stress condition} \quad K^2 = GE \quad (2.56)$$

$$\text{for plane strain condition} \quad K^2 = G \frac{E}{(1-\nu^2)} \quad (2.57)$$

For Mode I failure the limiting thickness (B) between plane stress and plane strain conditions is given by the Equation 2.58 [85, 86].

$$B = 2.5 \left( \frac{K_{Ic}}{\sigma_0} \right)^2 \quad (2.58)$$

Equation 2.58 is valid if linear elastic fracture mechanics conditions are met.

#### *2.7.3.1. Estimation of Stress Intensity Factor by Finite Element Method*

In general, estimation of stress intensity factor by finite element method is made defining a seam which represents a crack. The calculation method is based on the calculation of energy term (J-integral) around a path enclosing the crack tip elements.

#### *2.7.3.2. Estimation of Stress Intensity Factor by Weight Function Solutions*

In the study, weight function solution for the “inclined surface cracks was applied for analytical computation of stress intensity factor for edge cracked axle geometries [56]. In weight function solution method verified analysis of the surface cracked semi-infinite plate models are presented in Equations 2.59-2.62. Global and local coordinate systems for the problem are presented in Figure 31.

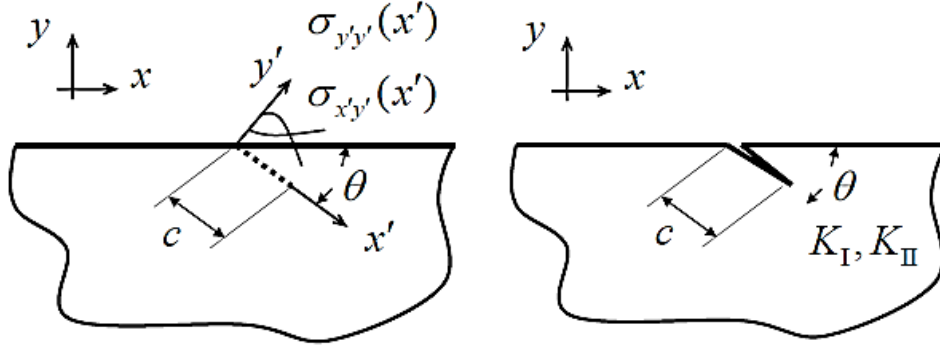


**Figure 31** Stress distribution along x'y' axes placed on the inclined crack plane [56].

For  $hk=11$  and  $hk=22$

$$h_{hk}(x', c, \theta) = \sqrt{\frac{2}{\pi c}} \left[ \left(1 - \frac{x'}{c}\right)^{-\frac{1}{2}} + \sum_{i=1}^4 \alpha_i^{hk}(\theta) \left(1 - \frac{x'}{c}\right)^{-\frac{1}{2}} \right], hk = 11 \text{ \& } hk = 22 \quad (2.59)$$

$$\alpha_i^{hk}(\theta) = \lambda_{i1}^{hk} \tan^2(\theta - \pi/2) + \sum_{j=2}^5 \lambda_{ij}^{hk} \cos((j-2)(\theta - \pi/2)) \quad (2.60)$$

For  $hk=12$  and  $hk=21$

$$\alpha_i^{hk}(\theta) = \lambda_{i1}^{hk} \tan^2(\theta - \pi/2) \sin(\theta - \pi/2) + \sum_{j=2}^5 \lambda_{ij}^{hk} \sin((j-1)(\theta - \pi/2)) \quad (2.61)$$

$$h_{hk}(x', c, \theta) = \sqrt{\frac{2}{\pi c}} \left[ \sum_{i=1}^4 \alpha_i^{hk}(\theta) \left(1 - \frac{x'}{c}\right)^{-\frac{1}{2}} \right] \quad (2.62)$$

$\lambda_{ij}^{hk}$  values are given in Table 2 [56]. The stress intensity factors  $K_I$  and  $K_{II}$  are calculated by implementing stress matrix given in problem axes into Equation 2.64

$$\begin{bmatrix} K_I \\ K_{II} \end{bmatrix} = \int_0^c \begin{bmatrix} h_{11}(x', c, \theta) & h_{12}(x', c, \theta) \\ h_{21}(x', c, \theta) & h_{22}(x', c, \theta) \end{bmatrix} \begin{bmatrix} \sigma_{y'y'}(x') \\ \sigma_{x'y'}(x') \end{bmatrix} \quad (2.63)$$

The accuracy range of the model is reported as 1% provided that the angle  $\theta$  be within the range  $15^\circ$ - $165^\circ$  [56].

**Table 2** Angle coefficients for weight function solutions [56]

	$i = 1$	2	3	4
$\lambda_{ij}^{11}$				
$j = 1$	0.352260648	0.561740777	0.002757774	-0.082522228
2	20.12858867	-6.75915207	14.69890758	-6.555566564
3	-28.35443914	12.21105233	-24.64961078	10.87434602
4	10.61781505	-6.721903843	13.14073974	-5.893279322
5	-1.794159914	1.272090422	-2.589806357	1.200996132
$\lambda_{ij}^{12}$				
$j = 1$	0.04401007	-0.088936286	0.09297728	-0.035669115
2	5.730314603	-11.04002435	12.13325221	-4.883436003
3	-4.413898809	10.19534617	-11.84935675	4.856493593
4	1.598258465	-3.559021699	4.07900429	-1.676244823
5	-0.257065332	0.515781329	-0.548201846	0.214198514
$\lambda_{ij}^{21}$				
$j = 1$	0.177883032	0.728488774	-0.248806075	0.023045677
2	0.808784091	17.6992381	-10.7581263	3.112044367
3	0.101895496	-16.00705368	11.92486888	-4.026999105
4	-0.023285672	5.675420857	-3.879295621	1.234486015
5	0.001237758	-0.851326701	0.497548624	-0.133053283
$\lambda_{ij}^{22}$				
$j = 1$	0.114487102	-0.22899214	0.242228468	-0.093044459
2	8.781169684	-11.51130605	11.0665334	-4.245644102
3	-12.02782951	19.63198074	-19.64671793	7.575469487
4	4.571171695	-9.876681231	11.38812338	-4.668556109
5	-0.723370423	1.708779212	-2.077090179	0.884130668

The stress intensity factors  $K_I$  and  $K_{II}$  are calculated by implementing stress matrix given in problem axes into Equation 2.64

$$\begin{bmatrix} K_I \\ K_{II} \end{bmatrix} = \int_0^c \begin{bmatrix} h_{11}(x', c, \theta) & h_{12}(x', c, \theta) \\ h_{21}(x', c, \theta) & h_{22}(x', c, \theta) \end{bmatrix} \begin{bmatrix} \sigma_{y'y'}(x') \\ \sigma_{x'y'}(x') \end{bmatrix} \quad (2.64)$$

The accuracy range of the model is reported as 1% provided that the angle  $\theta$  be within the range  $15^\circ$ - $165^\circ$  [56].

In the study, presented SIF calculation model by weight function is applied. To define stress distribution in problem axis ( $x'$ - $y'$ ) calculation techniques for “stress distribution at in internal point” discussed in “Section 2.3.4” is used. Contact stresses causing stress along the crack path is obtained by FEM analysis of the problem.

In axle models, the weight function solution is adapted to free-expansion (finite) plate assumption, that is, compressive stresses accumulated due to semi-infinite plate assumption are disobeyed by the expandable finite end of the axle structure.

Weight function solutions for 100- $\mu$ m-long hypothetical edge crack, under 100 MPa opening mode stress stresses are presented in Table 3.

**Table 3** SIF Results for the 100  $\mu\text{m}$  inclined cracks obtained by weight function calculations presented at [56]

Mode	Crack Angle ( $\theta$ )	SIF ( $\text{MPa}\cdot\text{m}^{1/2}$ )
$K_I$	$45^\circ$	1.2482
$K_{II}$	$45^\circ$	0.6445
$K_I$	$135^\circ$	1.2482
$K_{II}$	$135^\circ$	-0.6445

The model was verified by referencing to “oblique edge crack in a semi-finite plane” case [63]. Comparison of the handbook solution with weight function calculations was presented in Table 4.

**Table 4** Comparison of SIF results for the weight function solution [56] and SIF handbook [63].

	Computed Value [56]	Reference Value [63]
$K_I$ ( $\text{MPa}\cdot\text{m}^{1/2}$ )	1.2482	1.2496
$K_{II}$ ( $\text{MPa}\cdot\text{m}^{1/2}$ )	0.6445	0.6459

The comparison presented in Table 4 has shown the compatibility and the verification of the weigh-function solution for the inclined surface crack case.

#### 2.7.4. Plastic Strain Field around Crack Tip

In Equation 2.51, the normal stress ( $\sigma_x$ ) in the direction of applied load increases to infinity as  $r$  goes to zero (Figure 32). Practically, this is not possible since the normal stress that can be attained is limited by the tensile strength of the material. Furthermore, the full elastic response of the material ends at the yield strength. Therefore, the induced strain has elastic and plastic components at the crack tip.

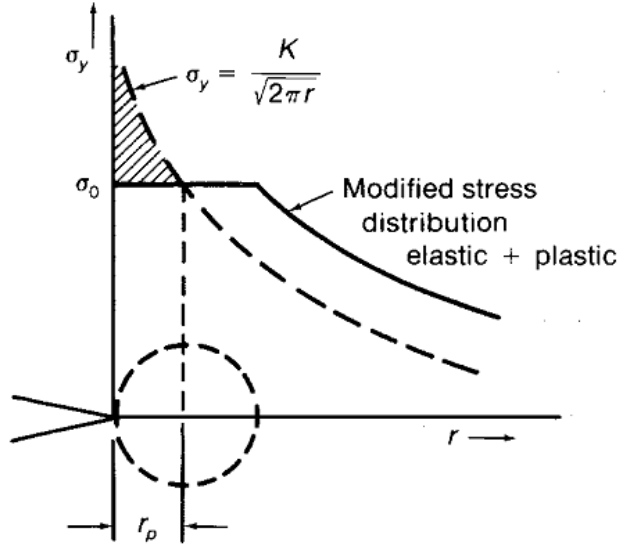


**Figure 32** Tensile stress and plastic zone around crack tip [43].

An effective crack length can be calculated by adding the plastic zone radius to the physical crack size [43].

$$r_p \approx \frac{1}{2\pi} \left( \frac{K}{\sigma_0} \right)^2 \quad (\text{plane stress}) \quad (2.65)$$

$$r_p \approx \frac{1}{6\pi} \left( \frac{K}{\sigma_0} \right)^2 \quad (\text{plane strain}) \quad (2.66)$$

$$a_{eff} = a + r_p \quad (2.67)$$

$$K_{eff} = Y\sigma \sqrt{\pi a_{eff}} \quad (2.68)$$

On the other hand, the Dugdale model describes plastic zone size (R) through Equation 2.69 [43].

$$R = \frac{\pi K^2}{8\sigma_0^2} \quad (2.69)$$

### 2.7.5. Out-of-Plane Deformations

Due to the triaxial state of stress and size effect, fracture toughness test is limited to the plane strain condition [85, 86]. Another reason for the plane strain measurement is the dependence of fracture toughness on the material thickness (Figure 33).

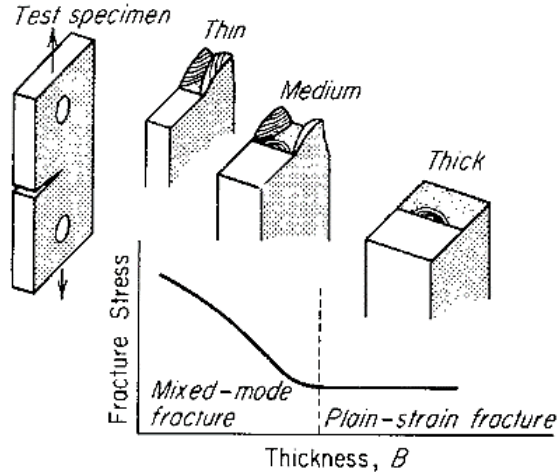


**Figure 33** Size effect in fracture toughness testing [43]

In cases of plane stress, “out-of-plane” deformations are observed around the crack tip in the form of reductions in the thickness direction (Figure 34) [43]. Using the compatibility equations of elasticity and Mode I displacement field [83, 84],

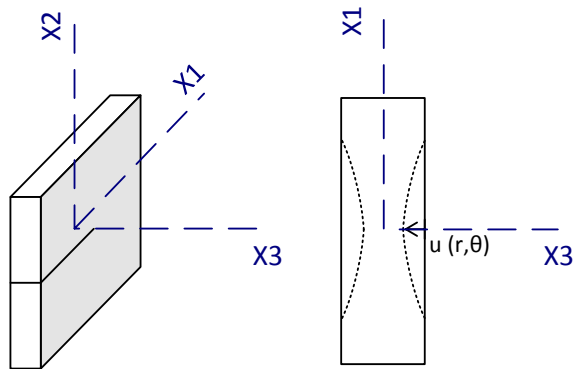


**Figure 34** Out-of-plane deformations

$$u_3\left(x_1, x_2, \frac{h}{2}\right) = \frac{1}{E} \int_0^{h/2} [\sigma_{33} - \nu(\sigma_{11} + \sigma_{22})] dx_3 \quad (2.70)$$

for plane stress  $\sigma_{33} = 0$

$$u_3\left(0, 0, \frac{h}{2}\right) = -\frac{\nu h}{2E}(\sigma_{11} + \sigma_{22}) \quad (2.71)$$

from the Equations 2.51 and 2.52,

$$(\sigma_{11} + \sigma_{22}) = \frac{2K_I}{\sqrt{2\pi r}} \cos\left(\frac{\theta}{2}\right) \quad (2.72)$$

$$u_3(r, \theta) = -\frac{\nu h}{E} \frac{K_I}{\sqrt{2\pi r}} \cos\left(\frac{\theta}{2}\right) \quad (2.73)$$

Out-of-plane deformation at the material surface

$$u_3\left(\frac{h}{2}, 0\right) = -\frac{\nu}{E} K_I \left(\frac{h}{\pi}\right)^{1/2} \quad (2.74)$$

where  $\nu=0.5$  for plastically deformed ligament.

### 2.7.6. Fracture Mechanics-Based Models

Fretting and rolling contact problems are the typical examples of multiaxial fatigue damage. Although the presented multiaxial models are sufficient to predict sensitive regions, life assessment of the components exposed to fretting damage still constitutes the important part of premature fatigue failures. Life estimations based on multiaxial fatigue models are still unable to predict the lifetime at the nucleation stage of fatigue cracks [1-5]. Very rapid development of small-fretting cracks is observed when minute cracks join each other.

Considering the difficulty in estimation of the number of cycles for crack nucleation, “singularity-aware approach” to fretting fatigue problem has been developed. Fracture mechanics based models aim to define allowable defect size which can be determined by non-destructive inspections [15].

Propagation of larger cracks differs from that of small cracks; i.e. small crack propagation is often increased by crack coalescence [24].



In the case of mixed mode, the propagation rate becomes dependent on the crack size, rubbing between fractured surfaces, crack closure, and the loading path. The crack propagation path is dependent on the effective modes of fracture [87, 88]. Propagation conditions for low carbon steel working under mixed mode loading (Mode I and Mode II) are presented in Figure 35 [89].

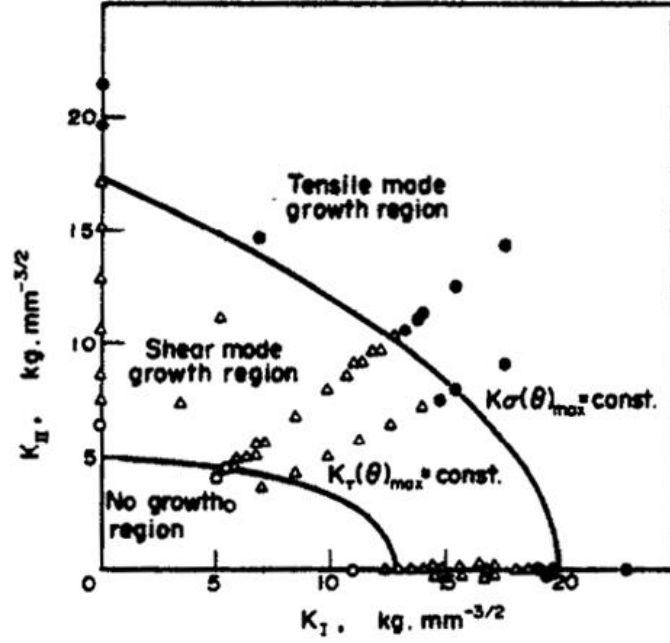


**Figure 35** Crack growth in mixed mode loading for low carbon steels [89].

Considering the stress field around a crack tip,

$$\sigma_{\theta} = \frac{1}{\sqrt{2\pi r}} \cos \frac{\theta}{2} \left[ K_I \cos^2 \frac{\theta}{2} - K_{II} \sin \theta \right] \quad (2.75)$$

$$\tau_{r\theta} = \frac{1}{2\sqrt{2\pi r}} \cos \frac{\theta}{2} \left[ K_I \sin \theta + K_{II} (3 \cos \theta - 1) \right] \quad (2.76)$$

Then, the intensity factors for shear and tensile loading are achieved by multiplying both sides by  $\sqrt{2\pi r}$ .

$$K_{\sigma(\theta)} = \cos \frac{\theta}{2} \left[ K_I \cos^2 \frac{\theta}{2} - K_{II} \sin \theta \right] \quad (2.77)$$

$$K_{\tau(\theta)} = \frac{1}{2} \cos \frac{\theta}{2} \left[ K_I \sin \theta + K_{II} (3 \cos \theta - 1) \right] \quad (2.78)$$

Propagation takes place when one of the intensity factor parameters exceeds the threshold level.

#### 2.7.6.1. Mixed Mode Growth Models

To apply Paris law to the propagation problems, the expression of an “Equivalent Stress Intensity Factor” is required. Different approaches to mixed mode crack propagation have been presented in the literature.

##### 2.7.6.1.1. Maximum Tangential Stress Model

Crack tip deflections during crack propagation and final failure under the effect of Mode I and II intensity factors were estimated based on the maximum tangential stress criterion [90]. According to this model, the highest level of the crack opening is achieved at an angle  $\theta$  where the highest value of tangential stress expressed in the cylindrical coordinate system around crack tip singularity is maximum (Figure 36).

Asymptotic stress fields for Mode I and Mode II openings, expressed by Williams solution, are given by Equations 2.79 and 2.80 [83, 84, 90].

$$\begin{pmatrix} \sigma_{rr} \\ \sigma_{\theta\theta} \\ \sigma_{r\theta} \end{pmatrix} = \frac{K_I}{\sqrt{2\pi r}} \frac{1}{4} \begin{pmatrix} -\cos(\frac{3\theta}{2}) + 5\cos(\frac{\theta}{2}) \\ \cos(\frac{3\theta}{2}) + 3\cos(\frac{\theta}{2}) \\ \sin(\frac{\theta}{2}) + \sin(\frac{3\theta}{2}) \end{pmatrix} \quad (2.79)$$

$$\begin{pmatrix} \sigma_{rr} \\ \sigma_{\theta\theta} \\ \sigma_{r\theta} \end{pmatrix} = \frac{K_{II}}{\sqrt{2\pi r}} \frac{1}{4} \begin{pmatrix} -5\sin(\frac{\theta}{2}) + 3\sin(\frac{3\theta}{2}) \\ -3\sin(\frac{\theta}{2}) - 3\sin(\frac{3\theta}{2}) \\ \cos(\frac{\theta}{2}) + 3\cos(\frac{3\theta}{2}) \end{pmatrix} \quad (2.80)$$

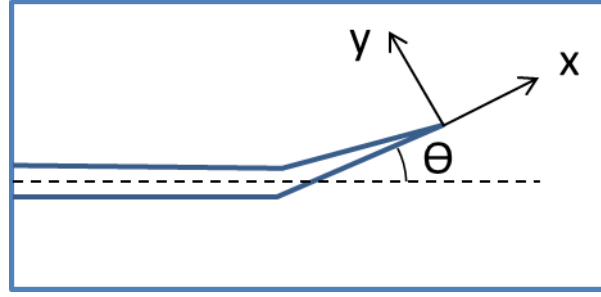


**Figure 36** Crack tip deflection and its translation to the x-y coordinate plane.

adding tangential terms together

$$\sigma_{\theta} = \frac{1}{\sqrt{2\pi r}} \left[ \frac{K_I}{4} \left( 3\cos\frac{\theta}{2} + \cos\frac{3\theta}{2} \right) - \frac{K_{II}}{4} \left( 3\sin\frac{\theta}{2} + 3\sin\frac{3\theta}{2} \right) \right] \quad (2.81)$$

the maximum stress intensity factor is achieved when

$$\frac{\partial \sigma_{\theta}}{\partial \theta} = 0 \quad (2.82)$$

Consequently,

$$K_I \sin\theta + K_{II} (3\cos\theta - 1) = 0 \quad (2.83)$$

The tangential stress intensity factor ( $K_{\theta}$ ) is defined as

$$K_{\theta} = \left[ \frac{K_I}{4} \left( 3\cos\frac{\theta}{2} + \cos\frac{3\theta}{2} \right) - \frac{K_{II}}{4} \left( 3\sin\frac{\theta}{2} + 3\sin\frac{3\theta}{2} \right) \right] \quad (2.84)$$

In this study, local analysis of crack tip was performed to predict the crack propagation direction. The maximum value of  $K_{\theta, \max}$  was also determined for  $\theta_{\max}$  at which crack tip deflections take place.

#### 2.7.6.1.2. Crack Tip Displacement Model

Based on the work by Tanaka [91] an equivalent stress intensity factor was described. According to the model, the displacements behind the crack tip are considered to cause propagation. Expression for the equivalent SIF is given in Equation 2.85

$$\Delta K_{eq} = \left[ \Delta K_I^4 + 8\Delta K_{II}^4 + \frac{8\Delta K_{III}^4}{(1-\nu)} \right]^{0.25} \quad (2.85)$$

#### 2.7.6.1.3. Strain Energy Release Rate Model

For a planar crack under plane strain condition strain, energy release for the mixed mode can be used as an equivalent SIF model. The relation for the mixed mode could be expressed by Equation 2.86.

$$J = G = \frac{1}{E} \left( K_I^2 + K_{II}^2 + (1+\nu)K_{III}^2 \right) \quad (2.86)$$

The terms in the parenthesis can describe an equivalent SIF ( $\Delta K_{eq}$ ).

$$\Delta K_{eq} = \left( \Delta K_I^2 + \Delta K_{II}^2 + (1+\nu)\Delta K_{III}^2 \right)^{0.5} \quad (2.87)$$

or

$$\Delta K_{eq} = \left( \Delta K_I^2 + \Delta K_I \Delta K_{II} + \Delta K_{II}^2 \right)^{0.5} \quad (2.88)$$

$\Delta K_{eq}$  can be implemented into the Paris law to estimate the remaining number of cycles to failure [24].

#### 2.7.6.1.4. Strain Energy Density Model

The accumulation of strain energy around the crack tip can be expressed by a strain energy density factor (S) [92].

$$S = a_{11}K_I^2 + 2a_{12}K_I K_{II} + a_{22}K_{II}^2 + a_{33}K_{III}^2 \quad (2.89)$$

where

$$a_{11} = \left( \frac{(1+\nu)}{\pi 8E} \right) \left[ (3-4\nu - \cos \theta)(1 + \cos \theta) \right] \quad (2.90)$$

$$a_{12} = \left( \frac{(1+\nu)}{\pi 8E} \right) \left[ (2 \sin \theta \{ \cos \theta - (1-2\nu) \}) \right] \quad (2.91)$$

$$a_{22} = \left( \frac{(1+\nu)}{\pi 8E} \right) \left[ 4(1-\nu)(1 - \cos \theta) + (1 + \cos \theta)(3 \cos \theta - 1) \right] \quad (2.92)$$

$$a_{33} = \left( \frac{(1+\nu)}{\pi 2E} \right) \quad (2.93)$$

where  $\theta$  is crack tip deflection in the cylindrical coordinates. The strain density factor produces a minimum at an angle ( $\theta_0$ ), at which the first derivative with respect to  $\theta$  is

zero and second derivative yields a positive value. The direction given by  $\theta_0$  indicates the path of crack extension. Strain energy density factor for cyclic loading is expressed by Equation 2.94.

$$\Delta S = 2 \left[ a_{11}(\theta_0) K_I^{mean} \Delta K_I + a_{12}(\theta_0) (K_{II}^{mean} \Delta K_I + K_I^{mean} \Delta K_{II}) \right. \\ \left. + a_{22}(\theta_0) K_{II}^{mean} \Delta K_{II} + a_{33}(\theta_0) K_{III}^{mean} \Delta K_{III} \right] \quad (2.94)$$

Use of such a parameter in the Paris law is given by Equation 2.95

$$\frac{da}{dN} = C_s (\Delta S)^{\frac{m}{2}} \quad (2.95)$$

$$C_s = C \left( \frac{2\pi E}{(1-2\nu)(1+\nu)} \right)^{\frac{m}{2}} \quad (2.96)$$

where C and m are the constants found by uniaxial fatigue crack growth tests. The iterative application of this method to a mixed mode problem was presented by Sih and Barthelemy [93].



## **CHAPTER 3**

### **EXPERIMENTAL PROCEDURE**

#### **3.1. Experimental and Analytical Approach**

Experimental and analytical approaches, given in Figure 37, were used to verify the applicability of multiaxial fatigue models in the investigation of fretting initiated fatigue failures in 34CrMo4 (AISI 4135) railway axles.

Own codes (program scripts) were developed to compute the related property. Apart from the main codes (I to V), some complementary codes (Code VI and Code VII) were used in the processing of mechanical test data. The red arrows indicate the necessary mechanical tests. Impact and low cycle fatigue tests were also performed.

Analytical calculations were compared with the fractography results. Flow diagram for fractographic analysis is given in Figure 38. The green lines indicate the critical outputs.

Features that is essential for the analysis are presented by the green line (Figure 38).

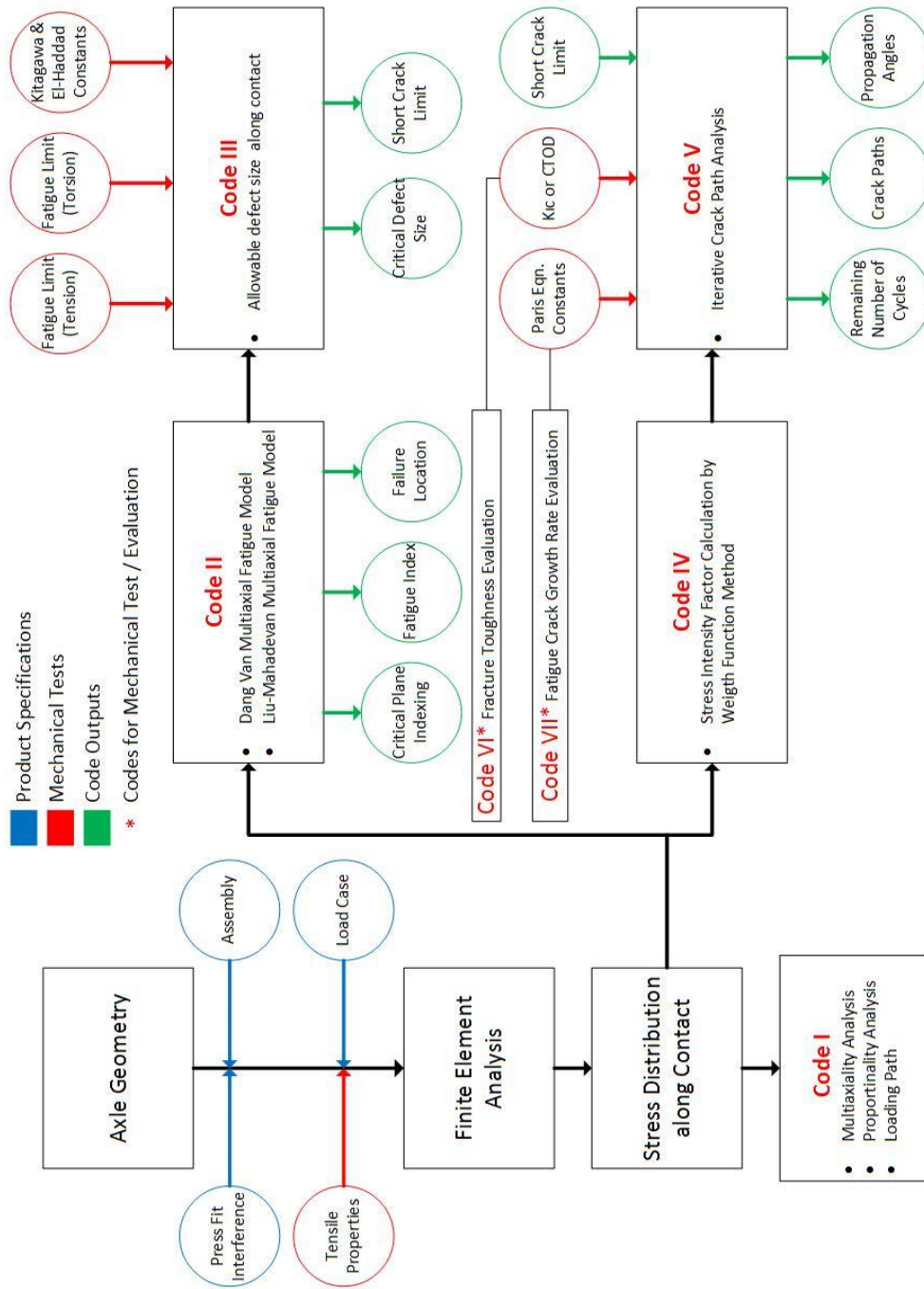


**Figure 37** Flow diagram for the analytical and experimental methods



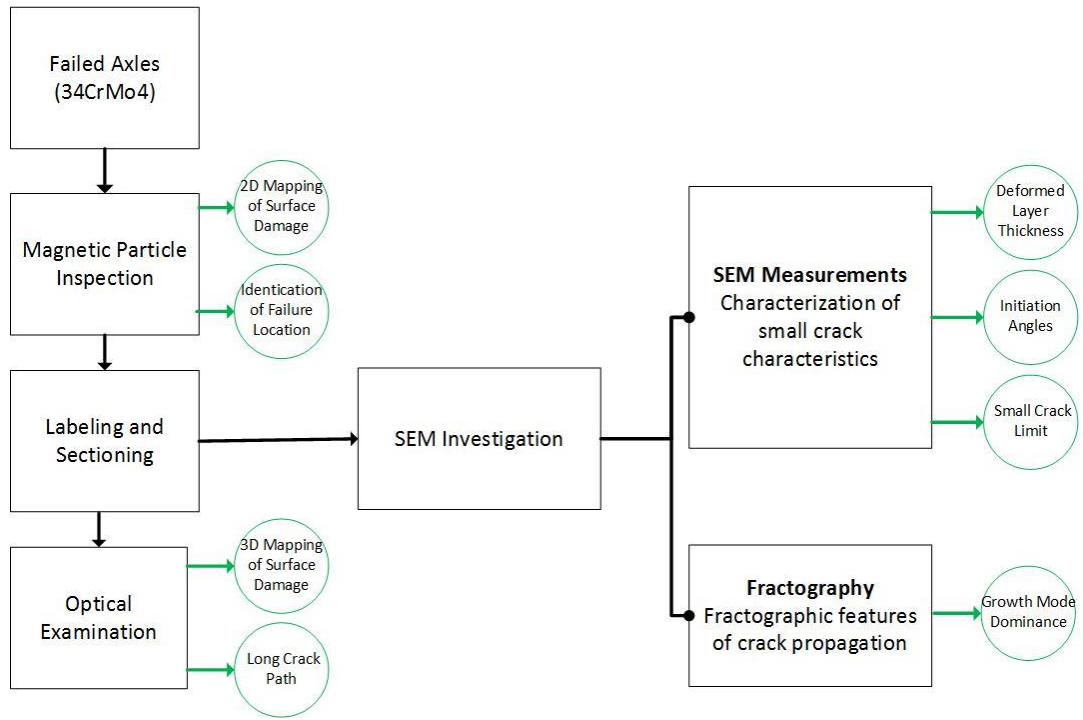


**Figure 38** Flow diagram for fractographic analysis.

### 3.2. Material and Geometry

Product requirements for railway axles are described in EN 13261 [6]. Minimum mechanical requirements and design principles for axle loading are presented in EN 13103 and EN 13104 [2, 3]. Standard definitions and material limits presented in these standards are mainly based on EA grade axle material. The qualification and validation procedures for the steel grades other than EA grade are also presented. Chemical compositions of standard EA grade axle steels and 34CrMo4 steel used in this study are listed in Table 5.

**Table 5** Chemical composition for EA grade railway axles and 34CrMo4 [6] (by weight %).

Grade	C	Si	Mn	P	S	Cr	Cu	Mo	Ni	V
<b>EA1N</b> (S35)	0.40	0.50	1.20	0.020	0.020	0.30	0.30	0.08	0.30	0.06
<b>EA1T</b>	0.40	0.50	1.20	0.020	0.015	0.30	0.30	0.08	0.30	0.06
<b>EA4T</b> (25CrMo4)	0.22-0.29	0.15-0.40	0.50-0.80	0.020	0.015	0.90-1.20	0.30	0.15-0.30	0.30	0.06
<b>34CrMo4</b>	0.37	0.40	0.90	0.025	0.035	1.20	-	0.30	-	-

The values represent the allowable limits for alloying elements. The designations N and T represents normalized and tempered microstructures, respectively. The axles were manufactured by hot forging, and then, normalization heat treatment was done. Mechanical requirements for various railway axle materials are given in Table 6.

**Table 6** Minimum mechanical requirements for some railway axle materials [6, 9].

	<b>EA1N</b>	<b>EA1T</b>	<b>EA2N</b>	<b>AAR M101 Gr.F.</b>	<b>EA4T</b>	<b>30NiCrMoV12</b>
<b>R<sub>p0.2</sub></b> (MPa)	min 320	min 350	min 350	min 360	min 420	min 850
<b>R<sub>m</sub></b> (MPa)	550-650	550-700	510-620	600-750	650-800	950-1080
<b>Elongation</b> (%)	min 22	min 22	min 22	min 17	min 18	min 15
<b>CVN<sub>T</sub></b> (J)	min 25	min 25	min 40	min 20	min 40	min 50
<b>K<sub>IC</sub></b> (MPa.m <sup>1/2</sup> )	52	54	61	46	73	117
<b>Fatigue Limit</b> (MPa)	274	min 250	-	-	min 350	510*

Fatigue design of railway axles has several aspects. The classical approach is given in the standards, and it aims to keep the applied stress level below the fatigue endurance limit at some critical positions shown in Figure 39 [2, 6].

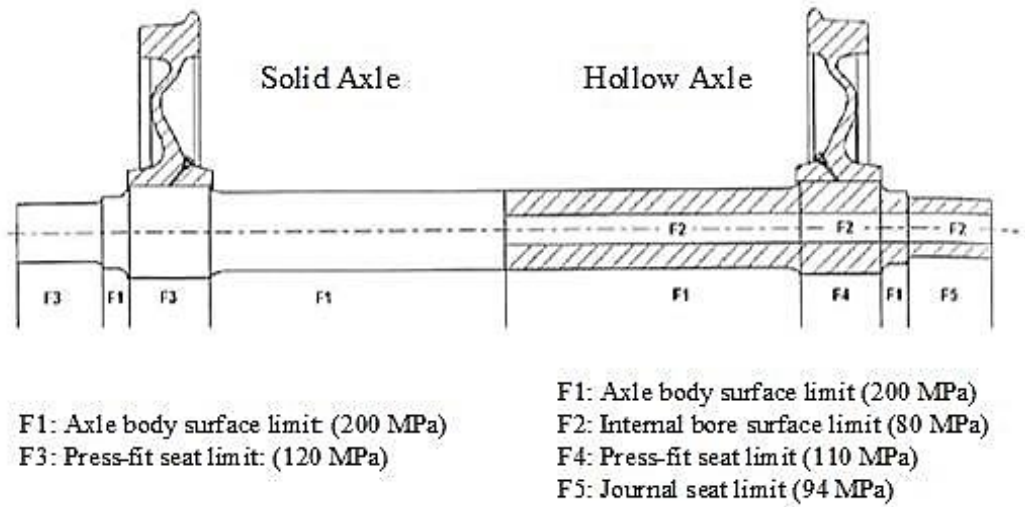


**Figure 39** Critical parts of solid (right), hollow (left) railway axles and maximum allowable stresses on each part (EA1N) [9].

The F2, F4, and F5 regions are only valid for hollow axles while F3 region is only valid for solid axles. In this study, the fretting problem encountered in the press-fit seat (F3 region) was investigated.

The fatigue limits given for the full-scale axle are different from those presented in Table 6. Stress concentration factors for various axle geometries are described based on the critical transitions of axle diameter and notch dimensions. Definitions of T-notch and S-transition are given in Figure 40.

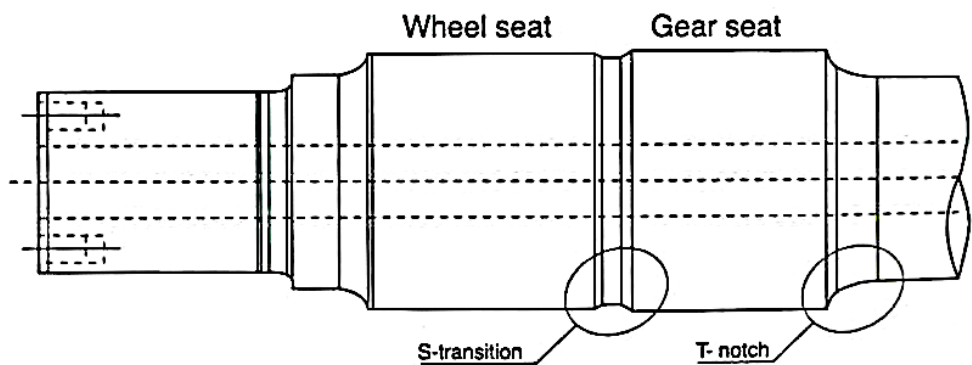


**Figure 40** S-transition and T-notch. [9].

The diagrams of stress concentration factors are presented in EN 13103 and EN 13104 for non-powered and powered axles respectively. Amounts of stress concentration and press-fit interference are defined by  $r/d$  and  $D/d$  ratio (Figure 41).

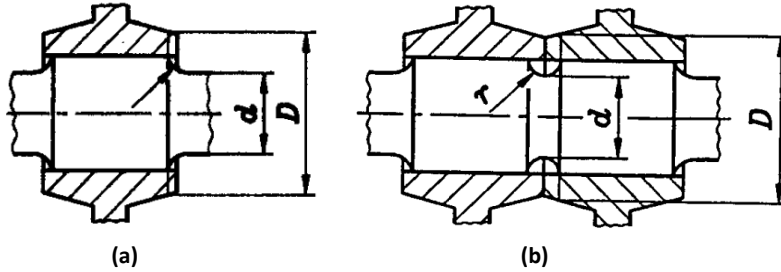


**Figure 41** Effective diameters and notch radius for (a) non-powered axle and, (b) powered axle [2]

In practice, the axles with a diameter ratio (ratio of maximum axle diameter to minimum axle diameter) between 1.2 and 1.0 are classified as F4 axles (or F3 axles in the solid axle case) where the fatigue failure is investigated at the press-fits (Figure 39). The axles with a diameter ratio higher than 1.20 are classified as “F1 axle” where the fatigue limit is evaluated at the axle body.

In this study, two damaged grooved axles (powered G1 axles) were dismantled from the DE24000 locomotives of Turkish State Railways (TCDD). Assembly and geometrical details of F3 axles are given in Figure 42 and Figure 43.

The  $r/d$  and  $D/d$  ratios are 0.077 and 1.15 respectively. Wheels and gear are press fitted on F3 surfaces with an interference of 0.310-0.360 mm. The friction coefficient between wheel-axle interface was assumed to be 0.4.

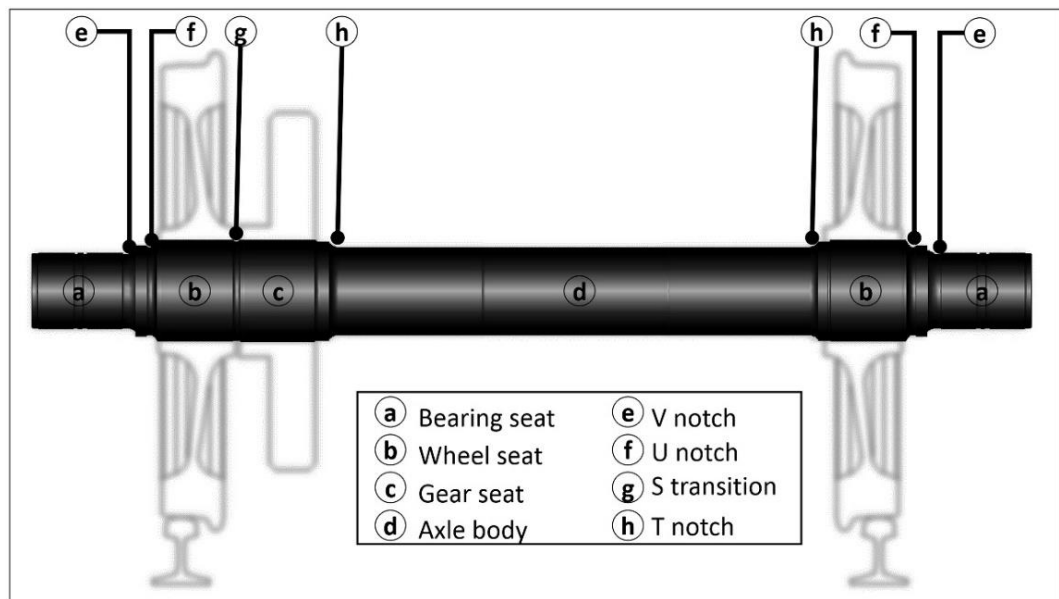


**Figure 42** Assembly details of railway axle and wheel.

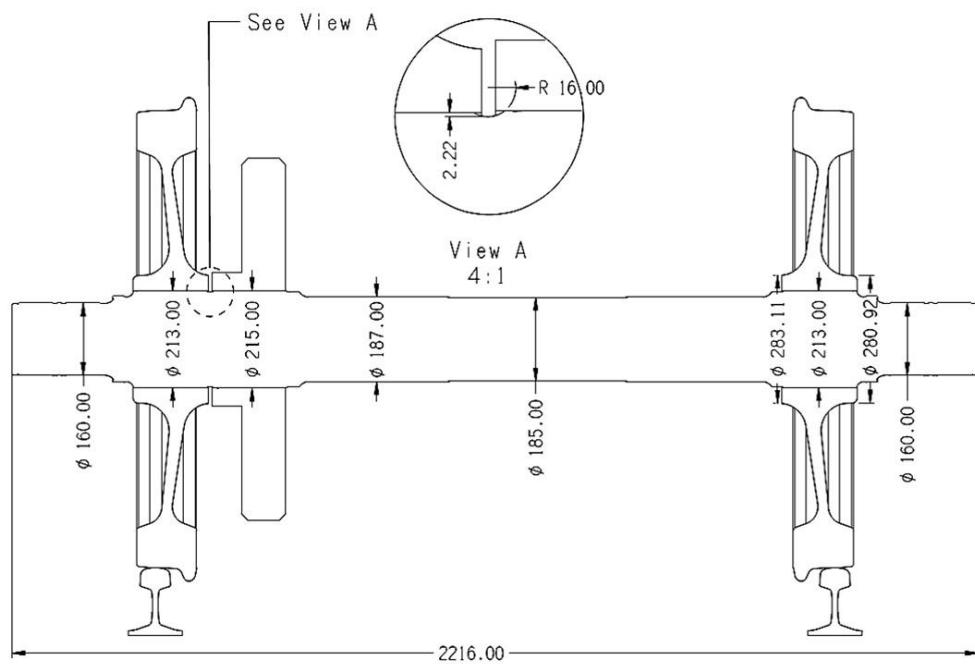


**Figure 43** Technical drawing of the F3 axle.

### 3.3. Metallurgical Characterization

Microstructure and chemical composition of the examined axles were described in the product specifications. The samples cut from the damaged components were metallurgically characterized to understand the metallographic state of the damaged zone and indications of metallurgical nonconformities were investigated.

First, macro etching was applied to examine microstructure variations along the cross-section. Ground and polished axle cross-section were etched to investigate any indications of case hardening or layering.

Second, sulfide distribution was determined by Baumann print method.

The longitudinal and transverse microstructures were also examined to investigate grain orientation affected by hot forging.

### 3.4. Failure Investigation

Failure investigation was made to identify distribution and initiation mechanism of the detected fretting cracks identified on the wheel seat (Figure 44).

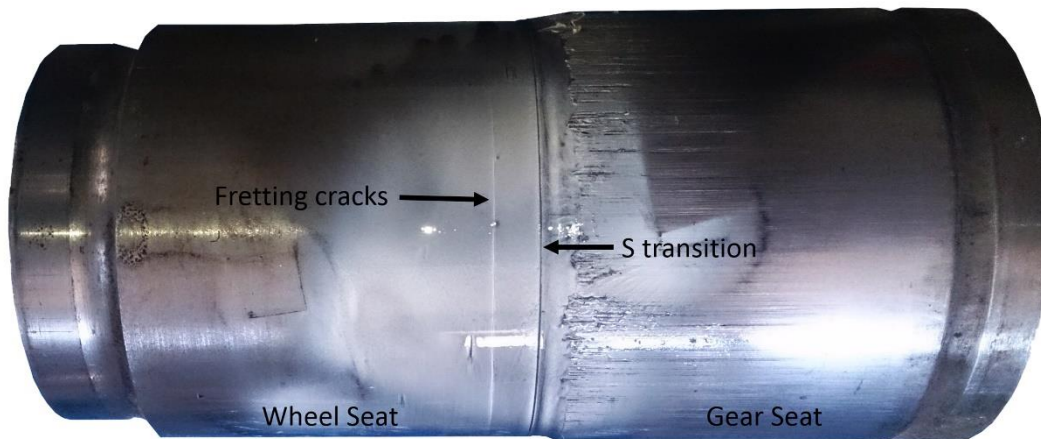


**Figure 44** Location of typical fretting cracks on the axle.

The main objectives of the failure investigation are to determine the propagation path of the major crack in 3D space to clarify the stages of crack propagation process and to show the microstructure dependency of fretting crack initiation.

#### 3.4.1. *Magnetic Particle Inspection*

The portion containing the major crack was determined by MPI, and a 30mm thick slice containing the major crack were cut from the wheel seat (Figure 45).

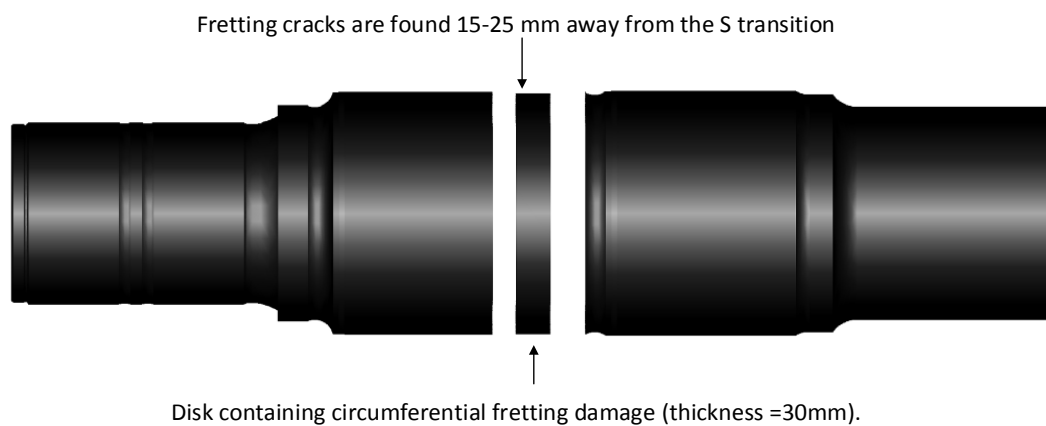


**Figure 45** Location of fractographic samples.

The extracted disk was placed on a rotating table, and MPI was repeated. A 2D map of the circumferential cracks was constructed by combining the photographs taken at successive locations. The recorded positions were stamped on the specimen surface to maintain traceability. (Figure 46).

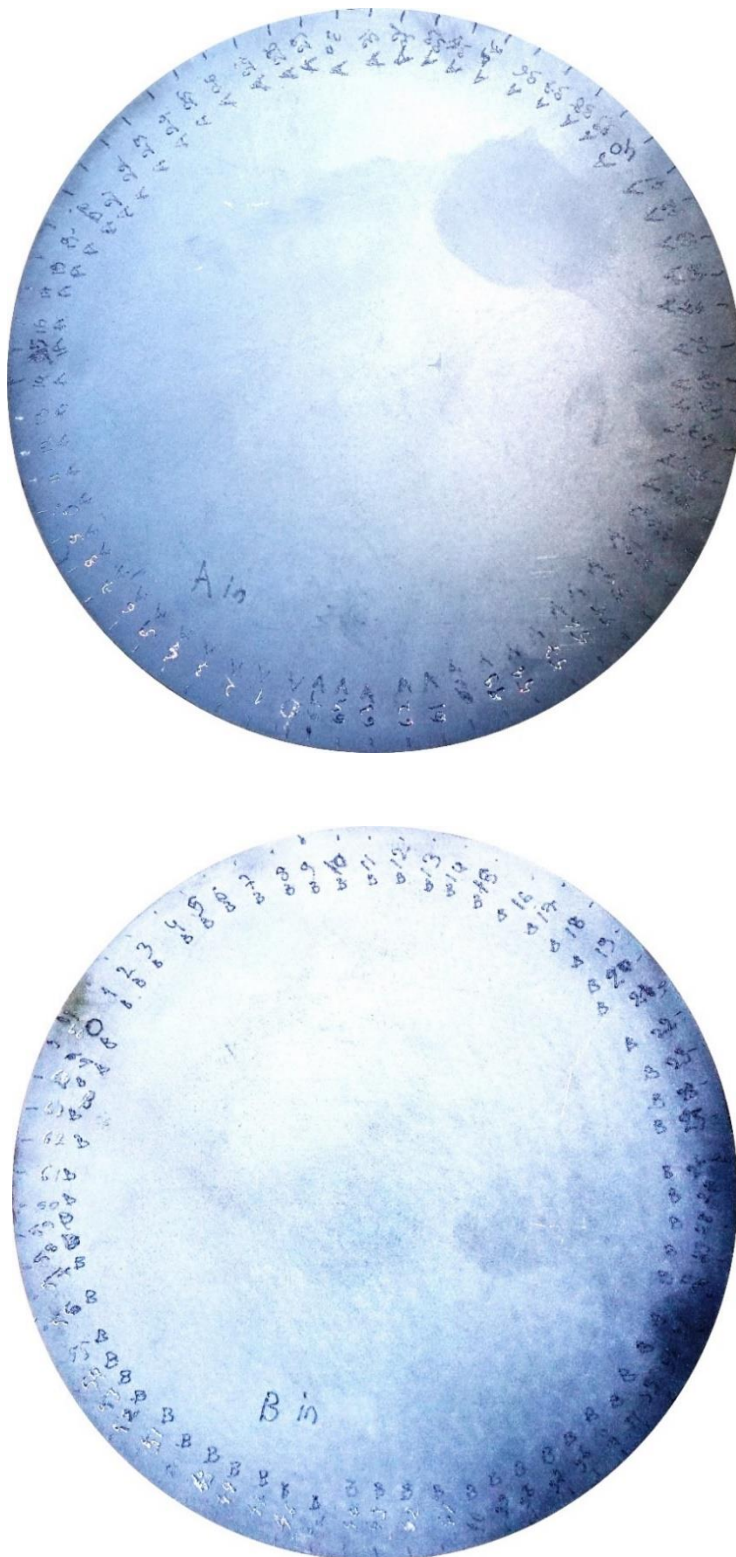


**Figure 46** Stamped ruler for identification of crack locations



### 3.4.2. Determination of Crack Depth and Distribution

Crack depth measurements were taken on the small slices cut from the disk. The cut plan was made based on the constructed defect map (Figure 47). The slices were taken as parallel lines to the axle diameter (Figure 48). 40 metallographic specimens were sectioned from the examined axles.

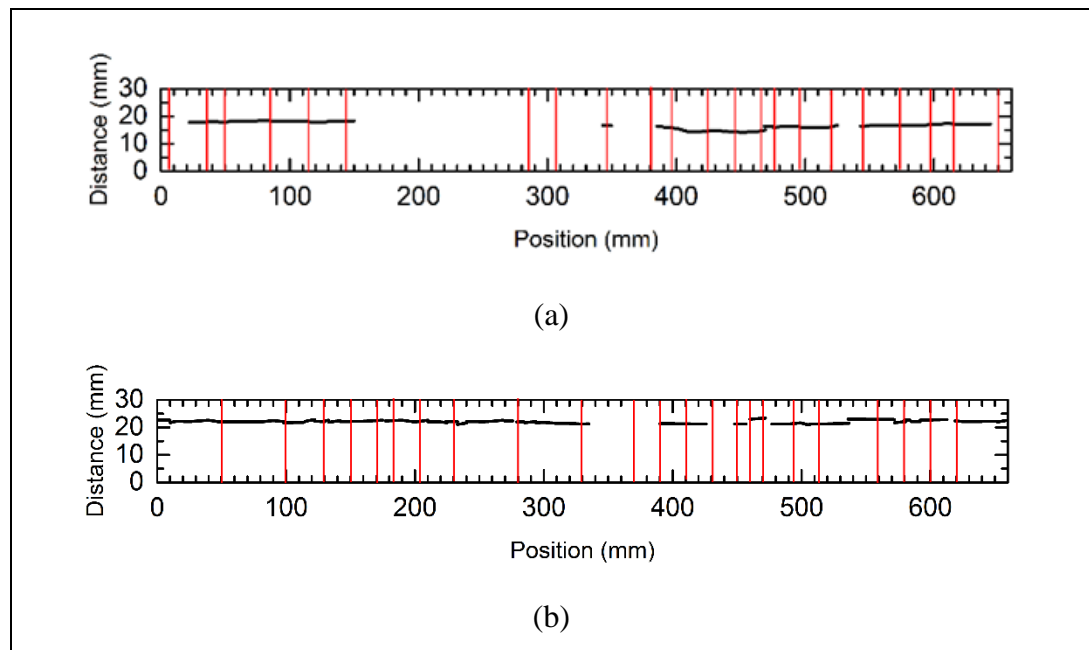
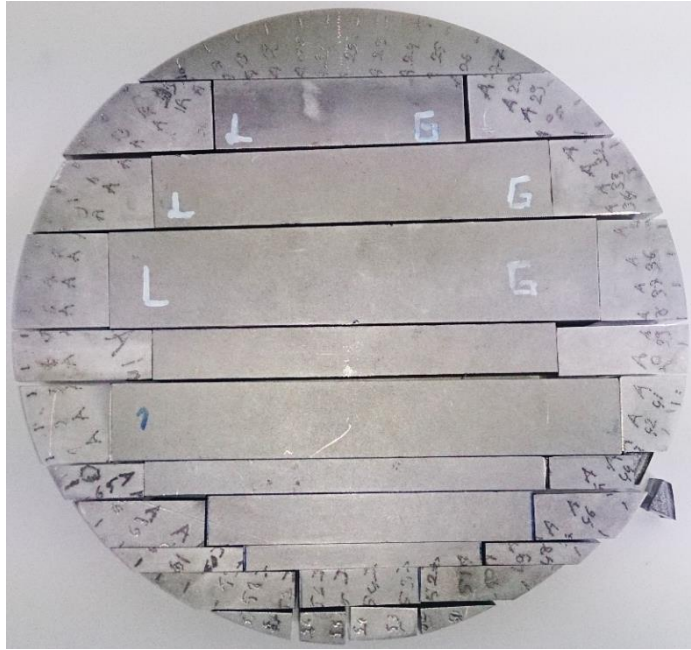


**Figure 47** Circumferential crack maps (a) axle A and (b) axle B. Metallographic sample locations were shown by vertical lines.



(a)



(b)

**Figure 48** General appearance and locations of the metallographic specimens for (a) axle A and (b) axle B.

Measured crack depths on the polished sections were translated into the cylindrical coordinate system to construct a polar map of crack tip locations. The applied correction method is summarized in Figure 49.

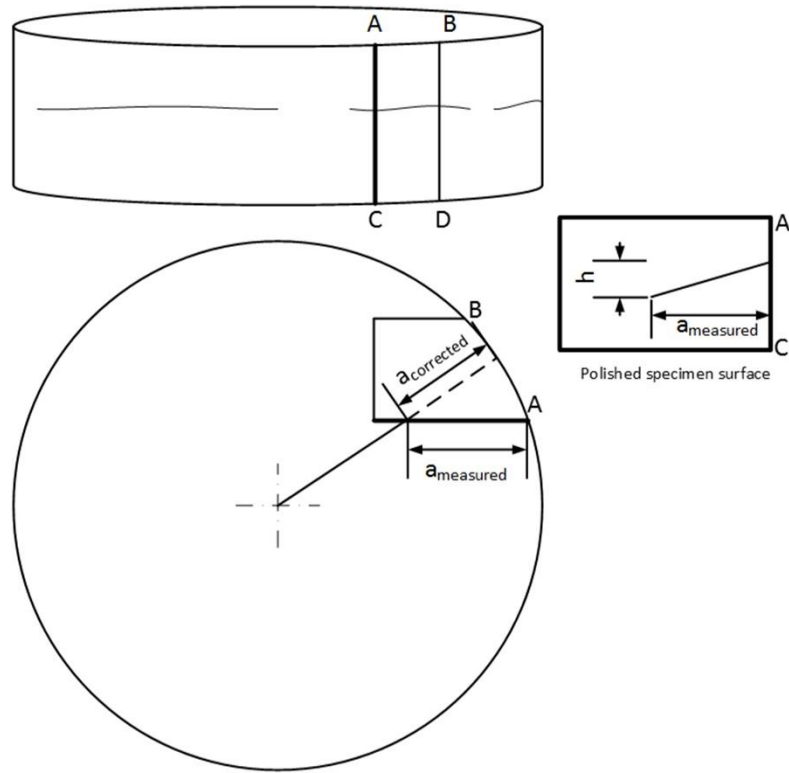


**Figure 49** Translation of crack measurements from specimen coordinates to global cylindrical coordinates.

The data was rearranged to identify the propagation path and the characteristics of the major cracks. The propagation angle was calculated by the ratio between the horizontal (h) distance and corrected crack depth ( $a_{\text{real}}$ ).

The experimentally determined range of propagation angle was compared to the angles computed by the various fracture models. Collected data points, by MPI and crack measurements, were merged to construct a three-dimensional propagation path of the cracks.

### **3.4.3. Fractography**

Fractography of the axle surface, crack initiation sites and crack propagation planes was made by SEM examinations. Fractographs of the material surface and the crack initiation sites were used to investigate the effect of microstructure on fretting crack initiation. The polished and etched specimens were used to distinguish the crack-microstructure interactions. Additionally, some of the specimens were broken into two, and then, fractographic features of the crack propagation plane were investigated.

## **3.5. Mechanical Characterization**

A series of mechanical tests were conducted to characterize mechanical properties of the axle material. Test specimens were manufactured from the inspected axles. The testing was carried out and evaluated according to the ISO standards.

### **3.5.1. Conventional Mechanical Tests**

Tensile testing was performed according to ISO 6892-1. Engineering and true stress-true strain curves were obtained. Specimens used in the test were taken in the longitudinal direction. The obtained results were utilized in the FEM analysis. Additionally, the strain hardening coefficient (K) and strain hardening exponent (n) were determined on the true stress – true strain curve.

Impact tests were conducted according to the ISO 148-1. The Charpy notch was positioned to check the axle's transverse and longitudinal direction. The test was performed at various temperatures between +20°C and -40°C to investigate “ductile to brittle transition.”

Hardness profile of the press fit seat was constructed to investigate the depth of surface plasticity due to press-fit and repeated loading. The hardness tests were done with HV 30 according to the ISO 6507-1.

### 3.5.2. Fracture Toughness Tests

Fracture tests were conducted according to ASTM E1820 and ISO12135 standards [85, 86, 94]. In the experiments, both  $K_{IC}$  and CTOD values are characterized. 20 mm thick SE(B) specimens in the Bx2B arrangement were machined from the axle. An integral knife edge and starting notch were machined by “wire electro-discharge machining” (WEDM) method. Precracking was applied by applying sinusoidal cyclic load with a ratio of 0.1.

Fracture toughness tests were conducted at room temperature and  $-10^{\circ}\text{C}$ . Load vs. crack mouth opening displacement (CMOD) curve of the tested materials were recorded and evaluated according to ISO 12135. Assessment of experimental data was done by the own computer codes named as “Fracture Toughness Evaluation System (Code VI).” CTOD values were determined according to energy method and direct method [86, 94, 95].

### 3.5.3. Fatigue Tests

Fatigue limit of the 34CrMo4 hourglass samples was determined according to ISO 12107 [96]. Axial fatigue tests were conducted according to ISO 1099 [97]. Specimen dimensions for the axial fatigue tests are given in Figure 50.

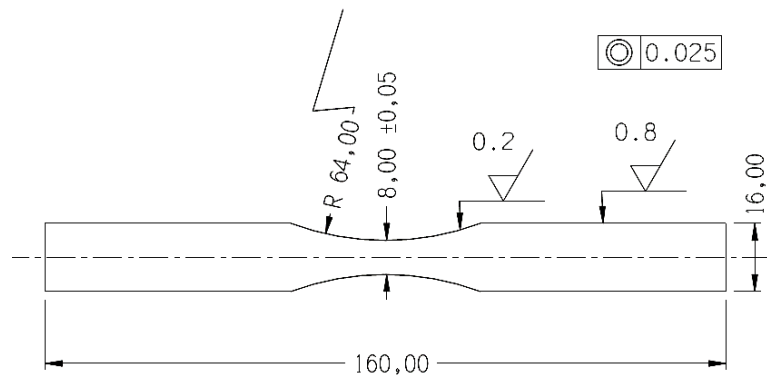


**Figure 50** Technical drawing of the axial fatigue test specimen.

Torsional fatigue testing was planned according to ISO 1352:2011 standard [98]. Torsional fatigue specimens were also used for low cycle fatigue experiments. Specimen dimensions for the torsional fatigue tests are given in Figure 51.

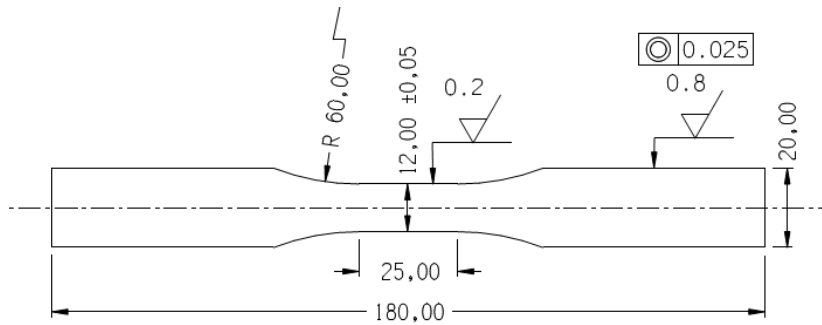


**Figure 51** Technical drawing of the torsional fatigue test specimen.

Fatigue limits were determined for 3 different load regimes. Two sets of axial tests with  $R=0$ ,  $R=-1$  and one torsional fatigue test with  $R=-1$  were done. A rotational beam fatigue device was used for the reversed axial tests (Figure 52). The tests with fatigue ratio ( $R=0$ ) were conducted by a servo-hydraulic testing machine (Figure 53).



**Figure 52** Rotating beam fatigue test setup.

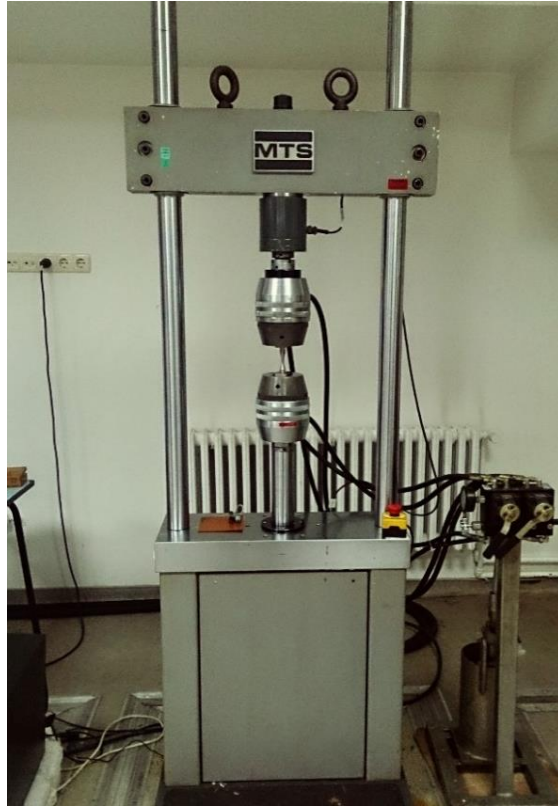


**Figure 53** Axial fatigue test equipment.

Fatigue limit was determined at 5 million number of cycles to failure. Unbroken specimens were classified as “run-out.” Staircase method was used for assessment. The method was applied according to ISO12107 [96].

#### **3.5.4. Kitagawa – Takahashi Analysis**

Kitagawa – Takahashi diagrams were constructed to investigate the effect of defect size on the fatigue limit. Vickers indentation marks and artificial defects machined by electro-discharge machining were placed on the electro-polished fatigue specimens. Murakami’s area parameter was used to classify defect size [41]. Transverse area of the indentation tip was measured calculate the defect area.

The corrected values of the size parameters were obtained by area measurements taken from the fractographic images (Figure 54).

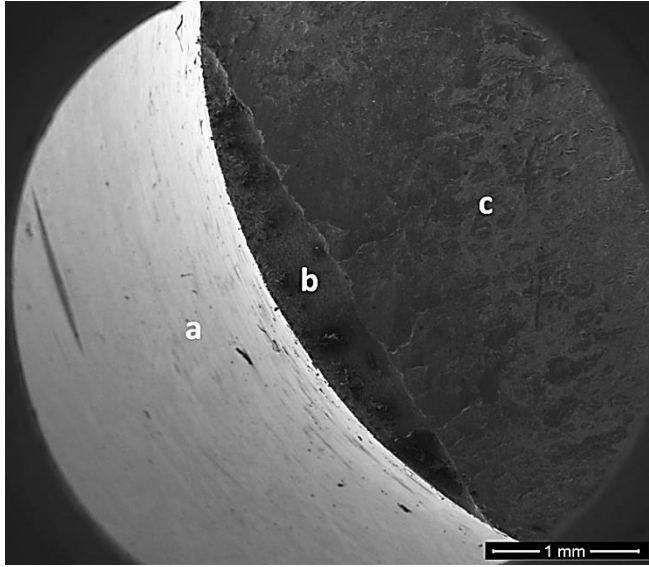


**Figure 54** (a)SEM image of specimen surface, (b) defect area machined by WEDM, (c)fatigue crack propagation plane.

Kitagawa-Takahashi diagrams were used to determine limiting size ( $\sqrt{\text{area}_0}$ ) and threshold stress intensity factor ( $K_{th}$ ) for non-propagating defects. The fatigue threshold intensity was estimated by using the determined non-propagating crack limit given in Equation 3.1 [64].

$$K_{I,th} = 0.65S_w \sqrt{\pi \sqrt{\text{area}_0}} \quad (3.1)$$

El-Haddad correction curve was fitted to the experimental data to express a relation between fatigue strength and the defect size. The obtained expression was used to determine critical defect size for the given stress state.

### 3.5.5. Fatigue Crack Growth Rate Tests

Fatigue crack growth rate tests were conducted according to ASTM E647 [99]. SE(B) specimens with the dimensions of 10mmx40mmx200mm were tested in the experiment. Crack length measurements were taken by “DC potential drop measurement set-up” (Figure 55). The values were normalized and fitted to the data obtained by the optical measurements taken at certain intervals of crack propagation.



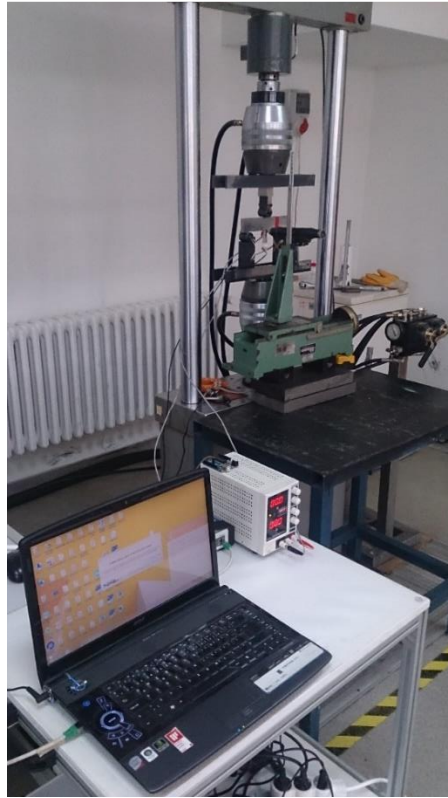


**Figure 55** Set-up for crack measurement by potential drop technique.

Potential drop measurements were converted to the physical crack size to obtain  $da/dN$  vs.  $\Delta K$  plots. Paris equation constants ( $C$  and  $m$ ) and threshold stress intensity factor for developing cracks were calculated.  $\Delta K$  increasing method was applied at two different stress intensity ranges to assess the effect of crack closure.

Modification of electrical data and evaluation of the results were processed by the own computer code named as “Fatigue Crack Growth Rate Evaluation System” (Code VII).

### **3.5.6. Cyclic Plasticity Tests**

The cyclic regime of the axle material was determined according to ASTM E606/E606M-12 [100]. Strain control was applied by placing clip-on extensometers on fatigue specimens with a straight gauge length (Figure 56). Cyclic stress-strain curves were constructed by integration of the hysteresis curves obtained at different strain amplitudes from 0.005 to 0.03.



**Figure 56** Strain-controlled fatigue test set-up.

In addition to cyclic plasticity tests, ratcheting behavior of the tensile test specimen was investigated. Strain accumulation for 350 MPa axially reversed load was recorded until a stable shake-down condition was achieved.

Results of the cyclic fatigue tests were used to investigate cyclic plasticity response and strain accumulation of the tested material.

### **3.6. Finite Element Analysis**

Finite element analysis (FEA) of the wheel-axle assembly was made to investigate stress history after press-fitting and during rolling. The cyclic stress path determined by the FEA was placed into the multiaxial fatigue models as an input.

### **3.6.1. Meshing**

ABAQUS software was used in FEA of the wheel-axle assembly. The full-scale component geometry was modeled in the software environment. The critical regions where the cracking is observed were assigned with fine mesh configuration.

3D FE model has been obtained by the revolution of a 2D solid mesh to get the regular distribution of solid elements. The starting 2D solid mesh was built by adapting the rectangular element CAX4R. An element size of 0.25 x 0.25 mm was selected in the area of interest. The 3D model is composed of C3D8R elements (8-node linear brick) with reduced integration and hourglass control.

### **3.6.2. Loads and Boundary Conditions**

Loads and boundary conditions of the wheel-axle assembly were set according to the free-body diagram presented in ISO 13104. The analysis consisted of two different steps. The half plane symmetry of the system is indicated by orange dots in Figure 57. The press-fit application was analyzed in the first step. The boundary conditions for the press-fit was set by holding the wheels movement on X and Y directions. Press-fit was simulated by applying a press-fit interference of 0.175 mm (0.350mm in total). The linear friction coefficient during pres-fitting is taken as 0.2 since the press fitting was done in hot oil. The axle was allowed to expand freely during press-fitting.

The load application and rail contact were introduced in the second step. A vertical axle load of 136850 N was applied on the upper surface nodes of the axle. A rigid coupling element was defined to deliver the axle load from the axle box (Figure 57). The contact between the rail and wheel was simulated by by setting semi-rigid kinematic coupling elements. Movement on the vertical axes was prevented. The axle was left free to rotate and slide freely in lateral directions. Finally, the mid-length of the axle was used as the symmetry plane for beam bending. The different friction coefficients were analyzed at the wheel-axle contact (0.2, 0.4, 0.6).

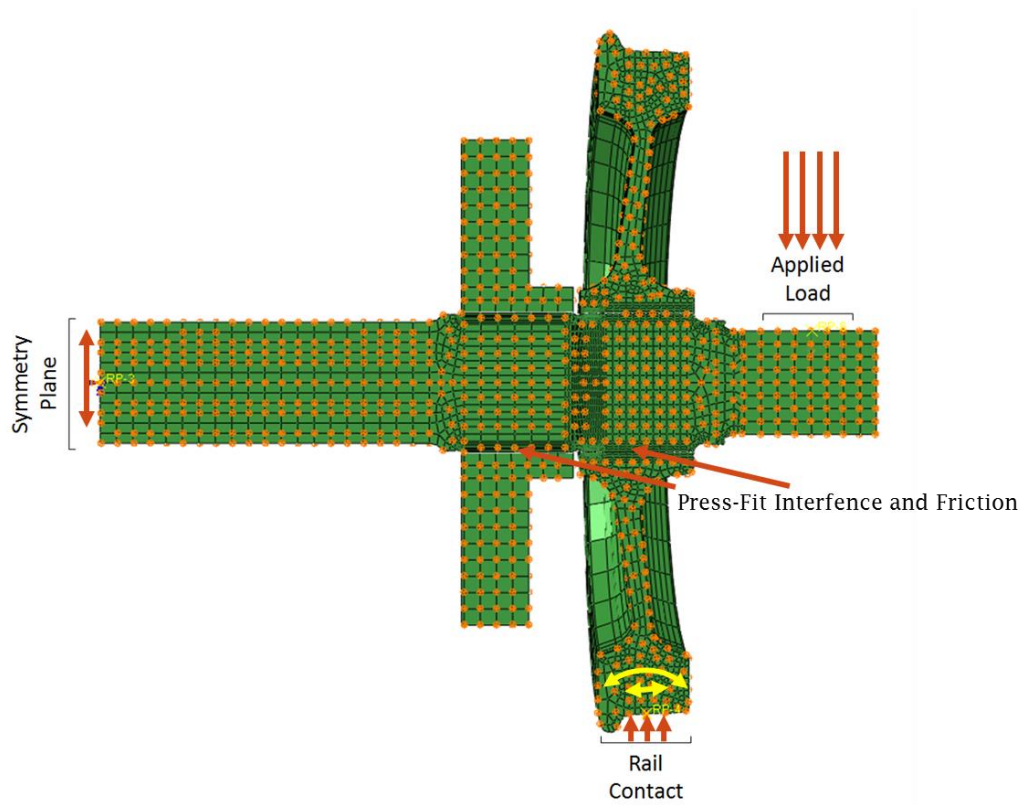


**Figure 57** Loading and boundary conditions applied to the wheel-axle assembly.

The maximum allowable limit for axle body (F1) and press-fit seat (F3) are 120 MPa and 200 MPa, respectively [2]. Considering the safety factors presented in ISO 13104 the maximum allowable tensile stress was set to 85 MPa at the press fits.

## CHAPTER 4

### RESULTS AND DISCUSSION

#### 4.1. Stress Analysis

Initiation of the fretting fatigue initiation was predicted by the post-processing of the stress cycle and stress distribution achieved by FEA. The investigations were supported by the detailed failure analysis of two full-scale axles which had been taken out of service before reaching their planned service lives.

The free body diagram of the wheel-axle-rail assembly and a moment diagram representing the moments at different sections of the axle are given in Figure 58. The analysis was made by applying vertical loads on the press-fitted assembly. A nominal bending stress of 85 MPa was aimed in the press-fitted section. The nominal stress was calculated by using the bending stress equation for simple shaft geometry.

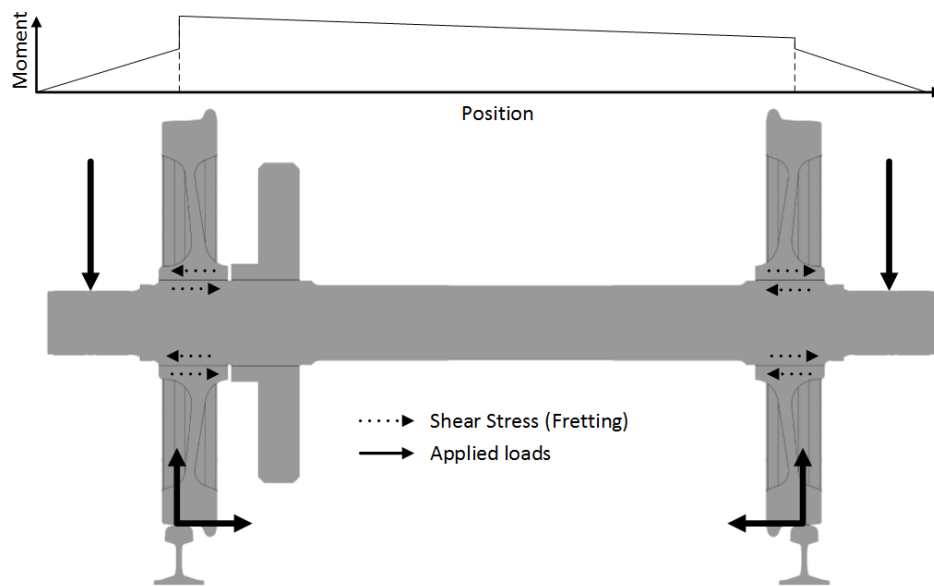


**Figure 58** Schematic view of the loading on the wheel-axle-rail assembly.

In service conditions, the bending stress caused by the axle pressure is much lower than the applied fatigue limit. But, the stress level increases with increasing dynamic

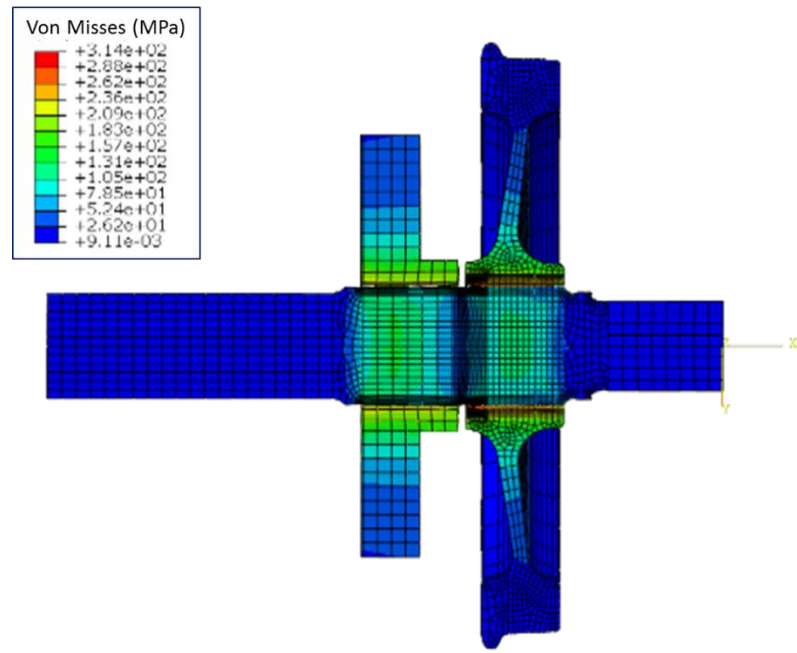
loads, vibration and impact loading from the damaged rail joints. Unbalanced side forces at the wheel-rail contact cause a moment which is transferred to the axle through wheel's side movements. The relative motion between the wheel and the axle cause the reversed shear which is responsible for the initiation of fretting damage.

The analysis consists of two steps. In the first the step, the wheel is press-fitted to the axle by holding the axle along the longitudinal axis, as in the case of practical application. In the second step, the assembly is pushed towards the rail by the applied axle pressure. The distribution of von Mises' stress during press-fitting steps are presented in Figure 59. In the general appearance, the highest level of Von Misses stress is observed below the press-fitted regions and at the root bearing transition notch (V-notch) at the bending side of the axle.

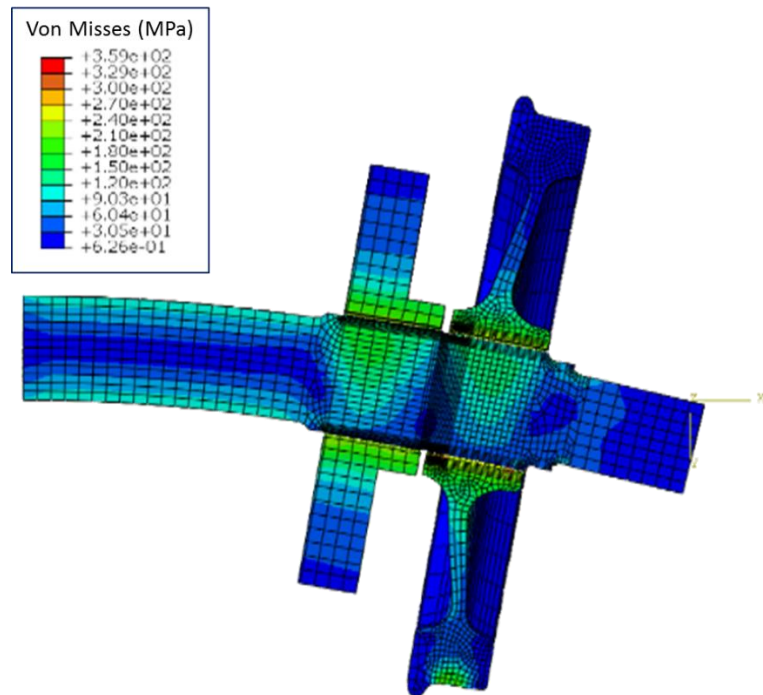
#### **4.1.1. Stress Distribution at Press-Fit Seat**

The distribution of longitudinal and shear stresses at the press-fit seat is given Figure 60a and b. The maximum longitudinal stress at the S transition reaches to the fatigue limit of the material (Figure 60a). Although the computed stress here is mesh size dependent, it gives an idea that the S transition is prone to experience corrosion fatigue. The fine-meshed region shown in Figure 60 is the location where the fretting cracks are observed.

The distribution the shear stress is given in Figure 60b. A minimum was observed at a location 16-18 mm away from the S transition. The magnitude of shear stress is seen to reach zero level at 4-6 mm below the surface. Another maximum was also observed at the contact edge of the press-fit which is also known as a possible location for fretting crack initiation. But again the computed stress at this point is a mesh singularity region. The singularity at the edge of the transition is removed from the analysis and not included in the multiaxial fatigue assessment.



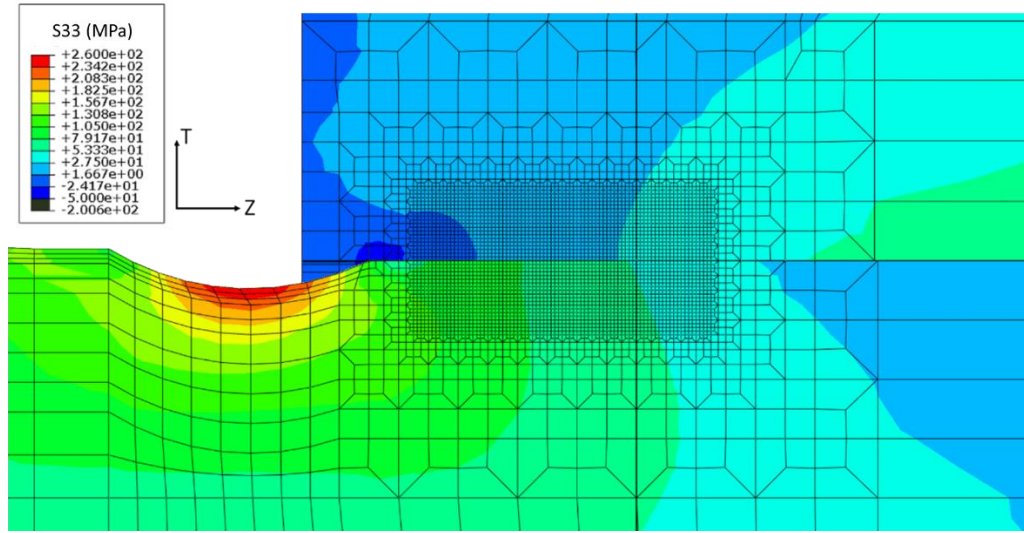
(a)



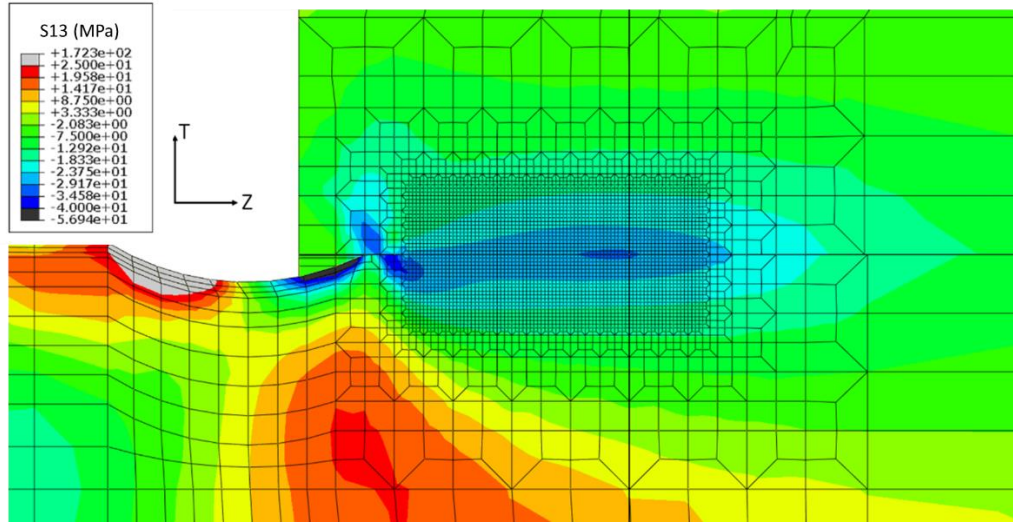
(b)

**Figure 59** Distribution of von-Mises' stress: (a) press-fitting, (b) static loading  
(Deformations are multiplied by a scale factor of 50).





(a)



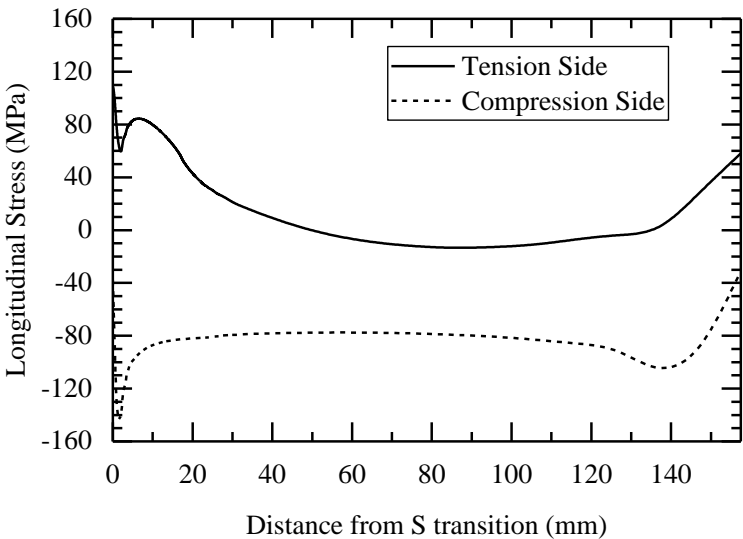
(b)

**Figure 60** Stress distributions for the maximum tensile stress loading of axle: (a) tensile stress, (b) shear stress

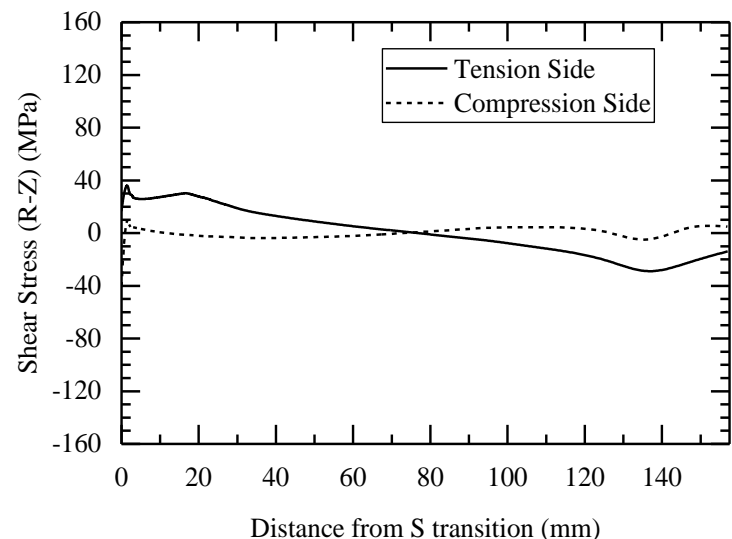
The stress distribution along the line representing the press-fit seat on the 2D plot given in Figure 60 is presented in Figure 61. The maximum and minimum shear stress appeared at the contact edge and at 10-20 mm and 140-150 mm distances from S transition. The last two are typical fretting fatigue locations reported by the Turkish State Railways (TCDD) [11]. Fretting cracks are observed within 10-20 mm distance



from S transition. The positive longitudinal stress accompanies the surface shear in this region. Additionally, this region is also very close to the gear assembly where the torsional loads are transferred to the axle. This region has the highest potential for initiation and multiaxial propagation of fretting cracks



(a)

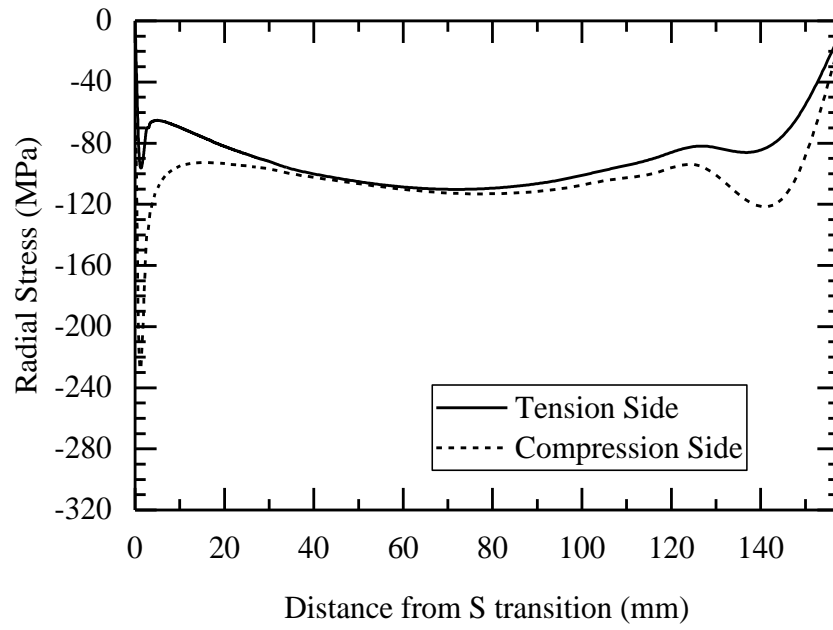


(b)

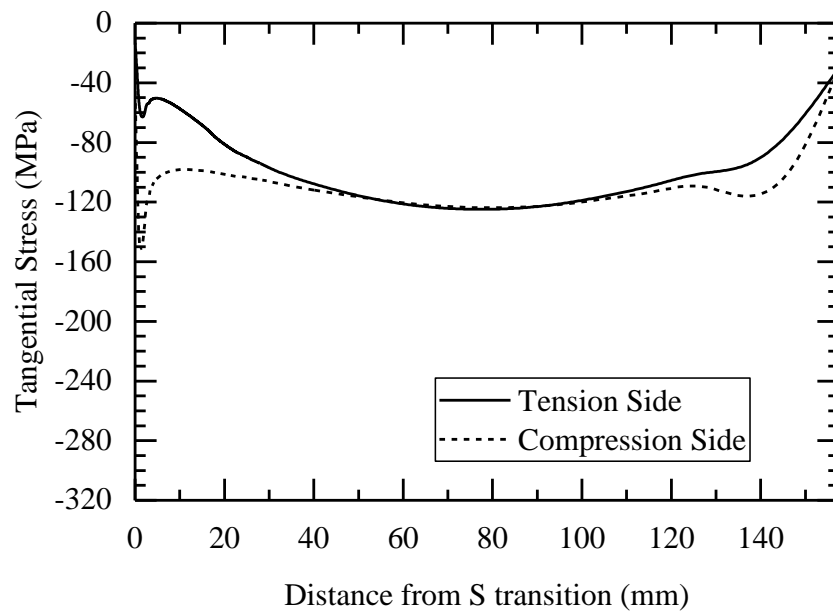
**Figure 61** Distribution of surface shear and tensile stresses along the press-fit surface during (a) maximum tensile loading cycle, (b) maximum compressive loading cycle.

The distribution of radial and tangential compression is presented in Figure 62. The presented stresses are calculated for the 0.350 mm press-fit interference. The magnitude of tangential and radial stress reduces towards the contact edges. The stick-slip boundary where the fretting fatigue cracks nucleate is found within this region [12, 15]. Comparison of the various FEM results revealed that the stick-slip boundary moves towards the center when the amount of interference is reduced. A severe fretting condition is achieved due to the increased amount of slip and displacement. In the opposite case, the stick-slip boundary move towards the contact edge and the fatigue failures due to increased stress concentration and fretting corrosion is promoted in this region. In railway operations, the amount applied press-fit is determined by the press-fitting curves provided for the given geometries. Optimization of the press-fit interference is a design parameter [5].

Crack locations of the investigated axles are shown in Figure 63. Circumferential fretting cracks are visible at 18 and 23mm away from the edge of S transition. The position difference might be due to variations in press-fit interference, roundness, surface characteristics or service conditions.

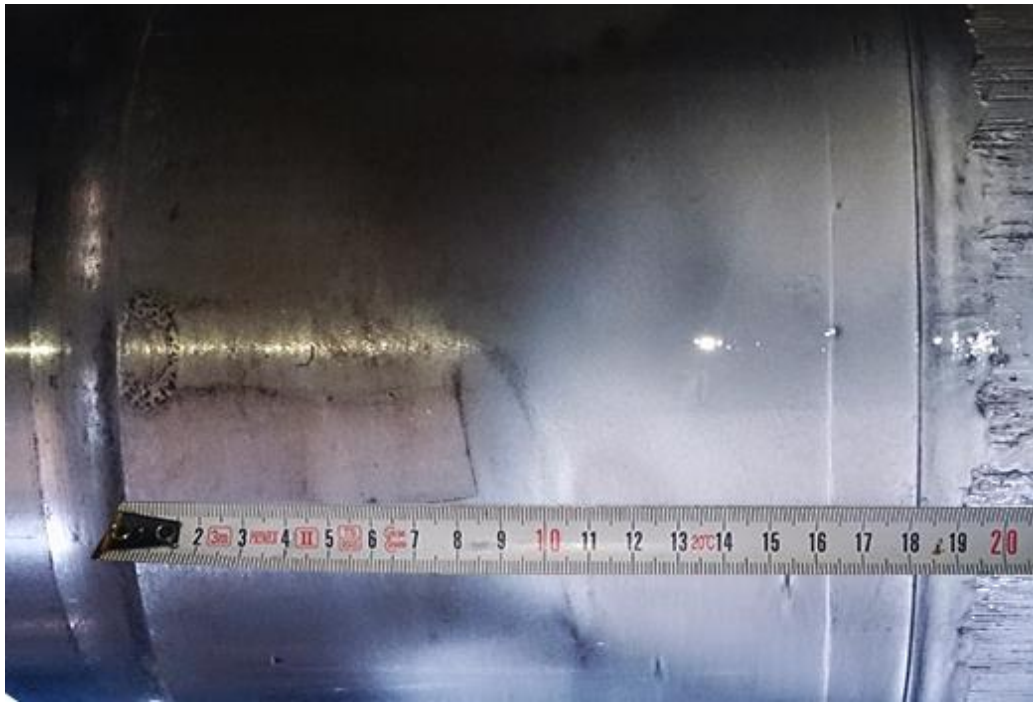


(a)



(b)

**Figure 62** Variation of the compressive stress components caused by applied press-fit during tension and compression cycles of the axle. (a) Radial stress distribution (b) tangential stress distribution.



(a)



(b)

**Figure 63** Fretting cracks on Axle A (a) and Axle B (b).

#### **4.1.2. The Effect of Friction Coefficient**

A linear friction coefficient between the contacting bodies is assumed to in the study. However, the friction coefficient between the contact surfaces is non-linear and changes by seizure, wear and debris accumulation at the press-fit [10, 15]. As a result, the effect of changes in friction coefficient was examined separately.

The friction coefficient slightly increases at the initial period of fretting due to the formation of cold welds between the asperities [10]. As fretting proceeds, damage caused by entrapped debris and corrosion products causes friction coefficient to decrease. Consequently, the stress distribution on the contact surface changes due to loss of interference. That is, the stick-slip boundary displaces from its initial position as fretting fatigue proceeds. Normal and shear stress distributions for different friction coefficients are presented in Figure 64.

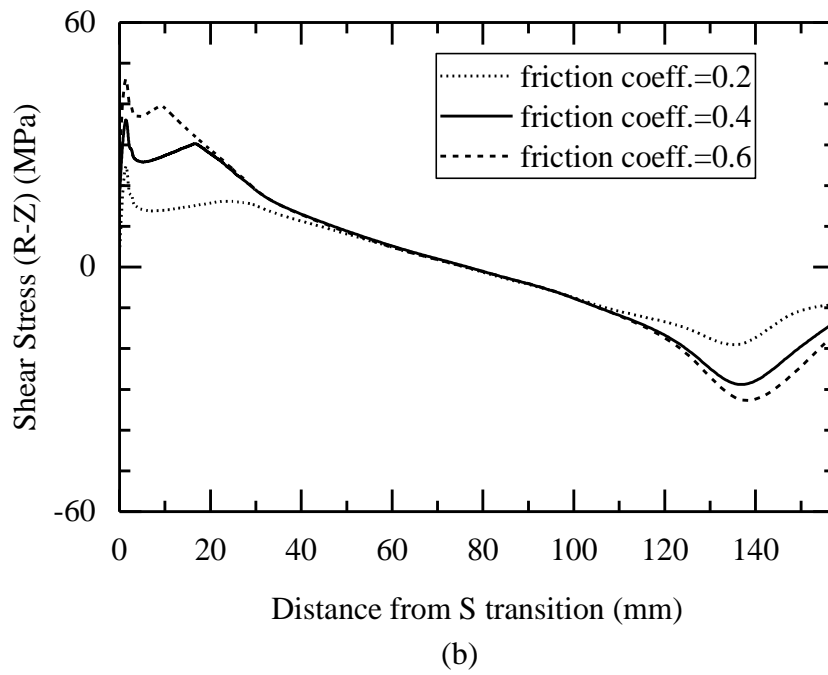
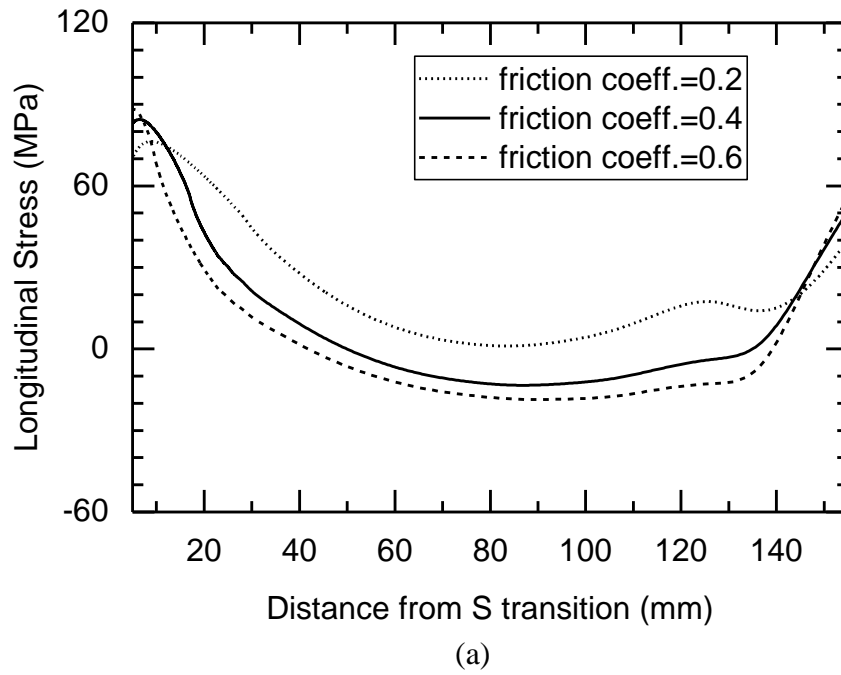


**Figure 64** Change of stress distributions along the press-fit with friction coefficient:  
(a) longitudinal stress, (b) shear stress

As shown in Figure 64 (b), the position of maximum shear stress amplitude moves towards the middle of the press-fit with decreasing friction coefficient. The tensile component of the applied bending stress becomes more effective as friction coefficient reduces (Figure 64 a). The amplitude of shear stress decreases with reducing friction coefficient. The overall effect of friction coefficient change is the shift of stick-slip boundary towards the center of the press-fit.

#### **4.1.3. Multiaxiality Analysis**

The change of stress state at a position where the typical fretting damage is located was examined in the multiaxiality analysis. Components of the stress path at 18mm away from the S transition during fatigue cycle has been extracted from the results of FE analysis. Distributions of tensile and shear stresses during one cycle of rotation are given in Figure 65 and Figure 66.

The path of stress cycle showed that all of the tensile axes are in-phase. Shear component R-T and T-Z remains nearly zero during rolling cycles (Figure 66). Out-of-phase loading between longitudinal stress and these shear components was observed (Figure 65 d,f, and Figure 66). In practical application, the T-Z component of shear is remarkably affected by the applied torque by the drive train. The random fatigue regime may become very effective on the circumferential propagation of existing fretting cracks by non-proportional loading, which is dependent on operation conditions and loads.

Tangential and radial components of the applied stress remain compressive during the entire period of rolling. Furthermore, the amplitude of cyclic stress is quite small. Consequently, these components are treated as the static loads caused by applied press-fit.

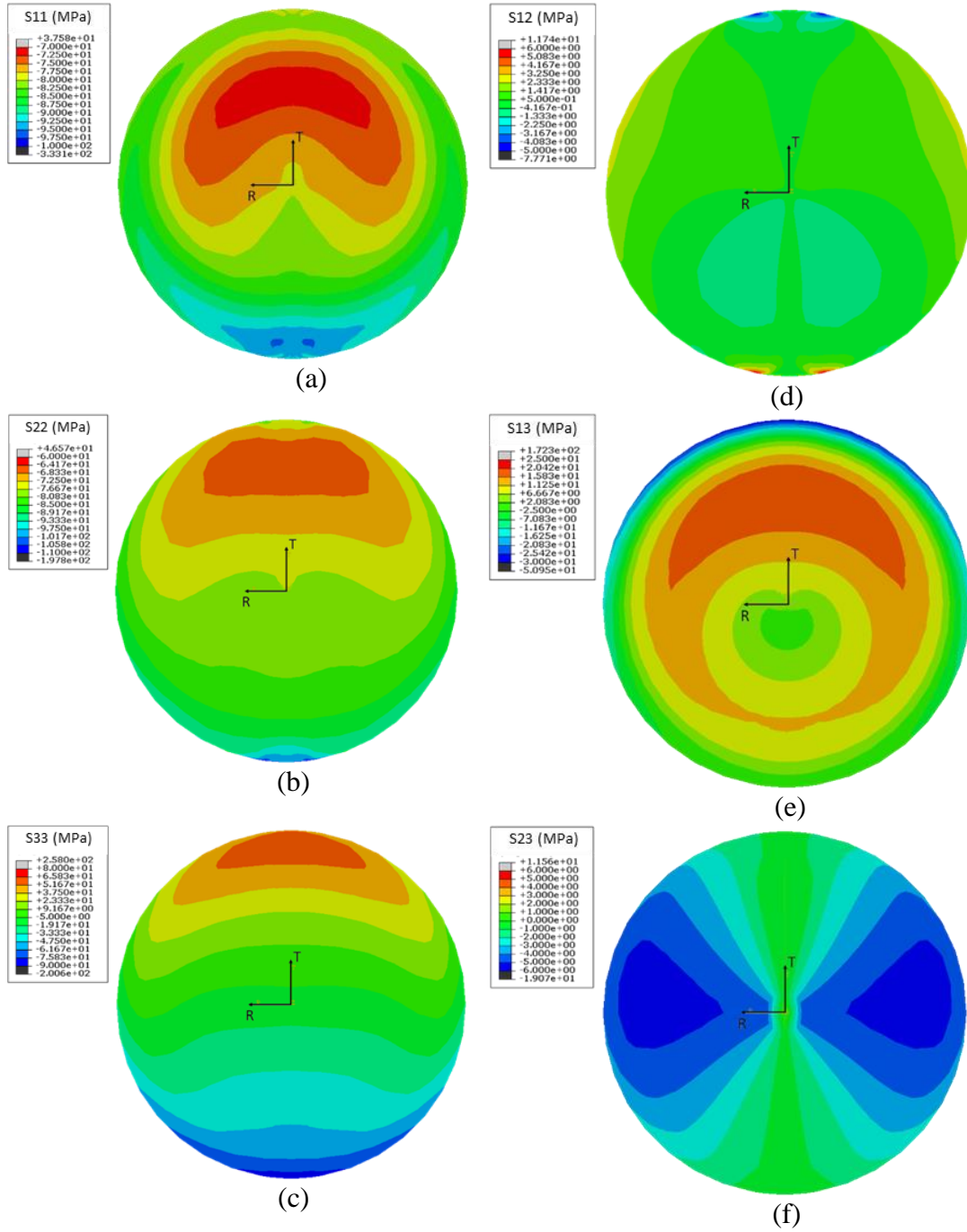


**Figure 65** Distribution of stresses at the axles section during static loading: (a,b,c) radial (S11), tangential (S22) and longitudinal (S33) stresses and (d,e,f) shear stresses (S12, S13, and S23 respectively).



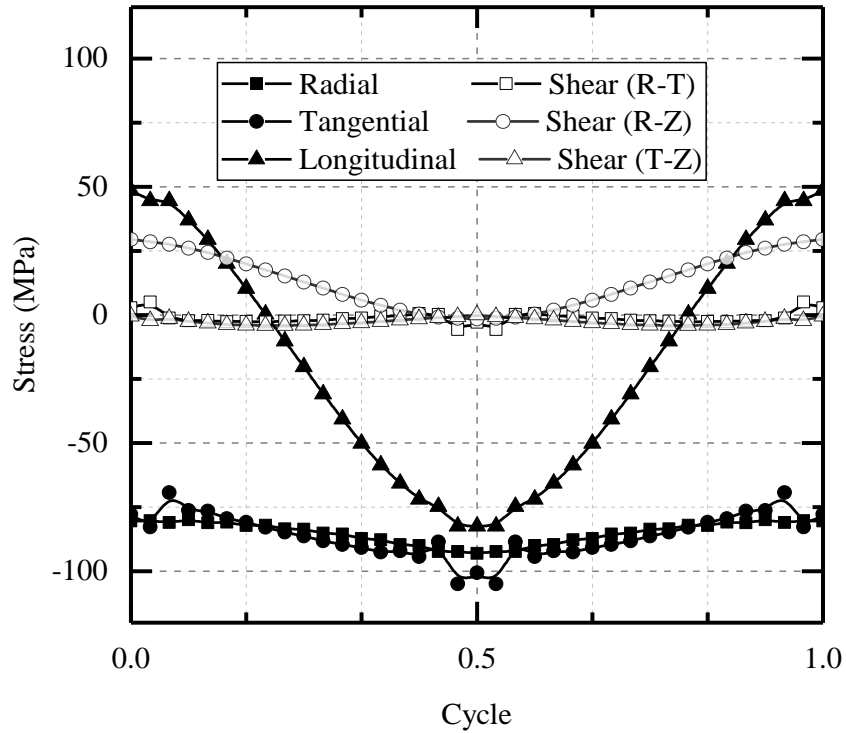


**Figure 66** Cyclic stresses during a loading - unloading cycle (at 18<sup>th</sup> mm).

Analysis of the stress components clearly reveals that the fretting damage is caused by in-phase cyclic loading of R-Z shear and longitudinal stress components. The distributions of longitudinal stress and shear stress at the press fitted region are presented in Figure 60. Change the tensile and shear components at the axle surface during maximum and minimum longitudinal stress positions are given in Figure 61. A detailed investigation reveals that the location of max shear coincides with the identified fretting crack locations (17.04mm away from S transition). Additionally, the surface shear was also effective under the axle surface until a depth of 12-16 mm which show that the effect of surface shear disappears at this depth. The highest shear amplitude is achieved at the first few millimeters as shown in Figure 60b.

#### 4.1.4. Loading Path and Proportionality Analysis

FE analysis revealed in-phase, and out-of-phase loading between normal and shear stresses exists during loading cycles. Proportionality analysis of the stress state at an 18mm distance away from the S transition is presented in Figure 67.

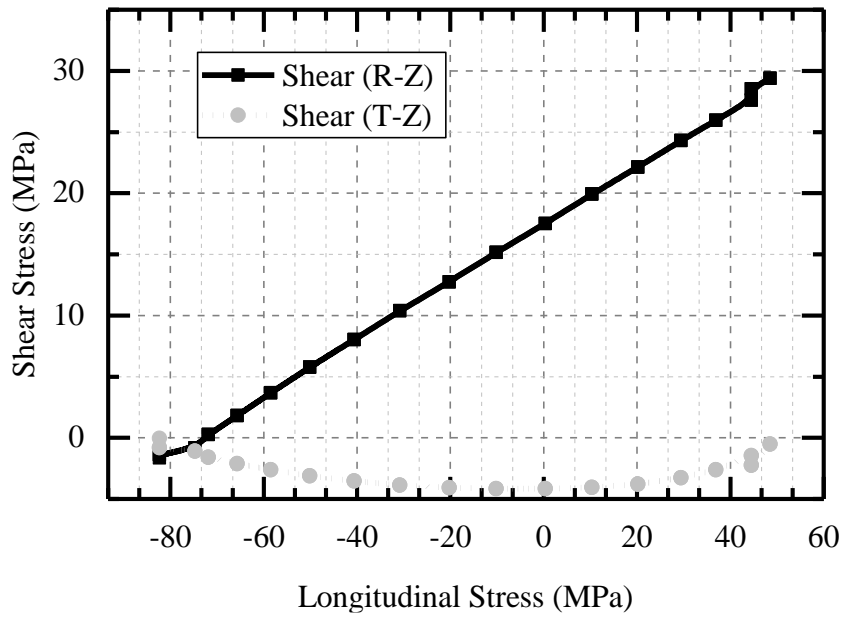
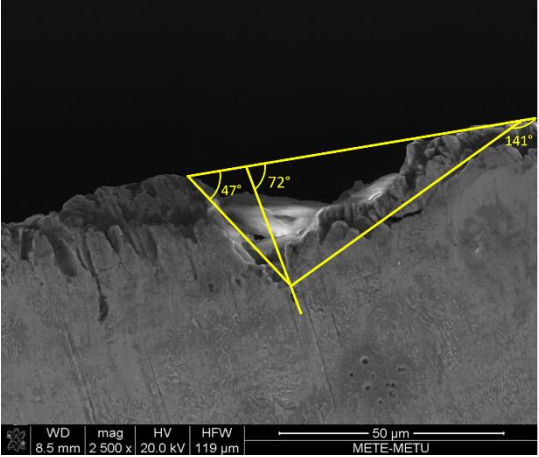


**Figure 67** Proportional and non-proportional loading path at an 18mm distance from S transition.

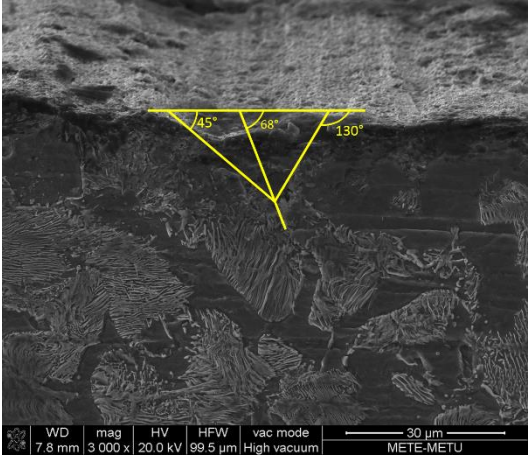
Proportional loading of longitudinal stress and fretting shear (R-Z) is identified for major cyclic stresses. The slope of the proportional curve is 0.237 which makes  $13.37^\circ$  angle with principal axis. Thus, the maximum shear planes are achieved at  $38.33^\circ$  or  $128.33^\circ$  counter clockwise rotations from the longitudinal axis (Z) on R-Z plane.

SEM investigations around the crack initiation region reveal the presence of small triangular zone giving rise to the propagation of major cracks. The results obtained from the proportionality analysis and fractography show that the orientations of small cracks coincide with the maximum shear stress planes which are  $38.32^\circ$  and  $128.32^\circ$  planes with respect to the longitudinal axis (Figure 68). This result is also consistent

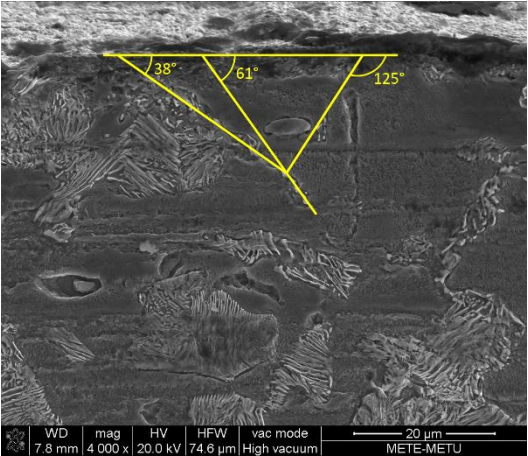
with the Stage I propagation characteristics [24]. The oxide fill between the rubbed crack walls in Figure 68d is an indication of effective shear during the earlier stages of fretting fatigue.



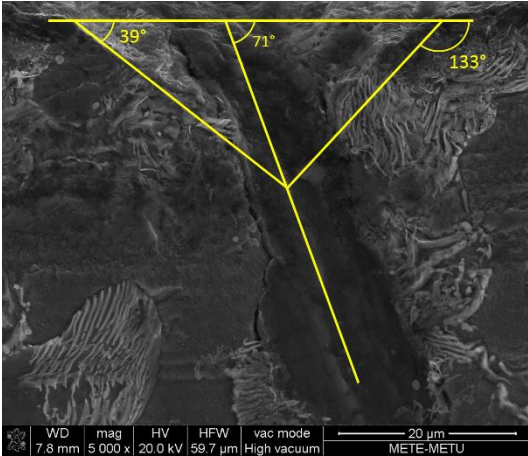
(a)



(b)



(c)

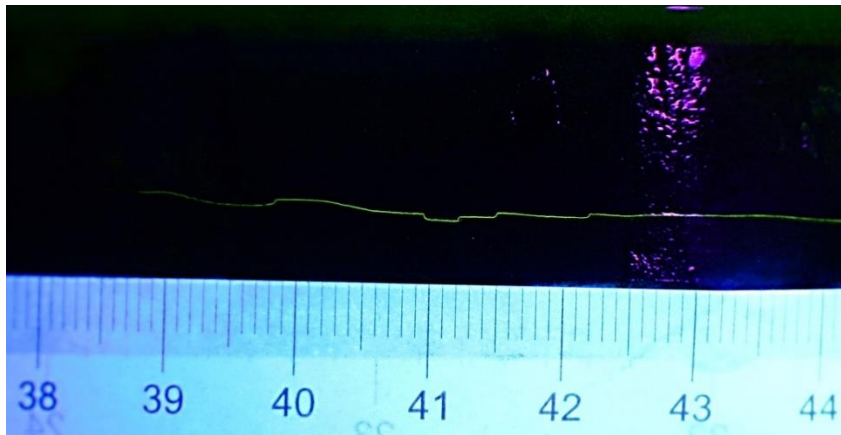


(d)

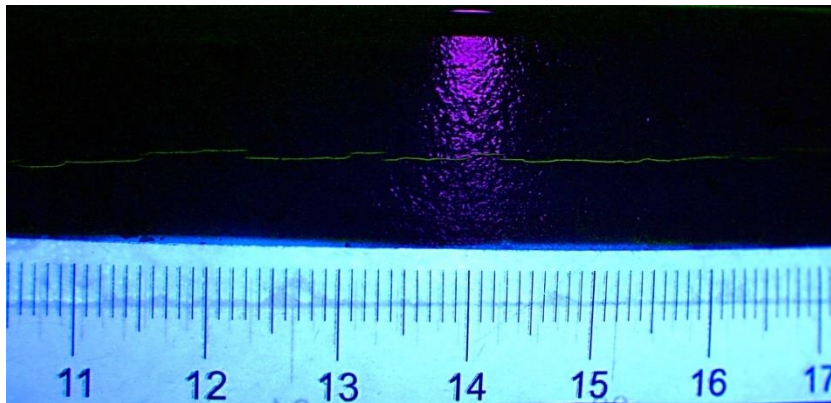
**Figure 68** Initiation regions of fretting cracks. Non-propagating small cracks (a,b,c) and propagated major crack (d) were examined under SEM. Accumulation of debris inside the major crack can also be seen (d).

#### 4.2. Fractographic Investigation of Fretting Fatigue Cracks

The simultaneous nucleation of small fretting cracks at several locations is known as the multi-site damage (MSD) [10]. The fretting cracks join and propagate readily under the influence of applied stress and result in fretting fatigue failure of the axles. Magnetic particle investigations of the observed fretting cracks on the examined axles showed broken line pattern which revealed the incorporation of parallel crack planes to form a major circumferential crack (Figure 69).



(a)



(b)

**Figure 69** Broken line pattern of the cracks: (a) Axle A, (b) Axle B.

The shape and distribution of the small fretting cracks and propagation path of the long crack chain are important in the assessment of fretting fatigue. In practice, propagated circumferential cracks behave as notches and propagates more rapidly than minute

surface cracks. The typical location and profile of the major fretting cracks are presented in Figure 70. The visible crack tip deflections indicated crack propagation under dynamic mixed mode conditions. As stated in the stress analysis the effect of surface shear reduced gradually underneath the press-fitted contact. The initial direction of crack propagation was towards the bearing side, but crack tip deflected to Mode I path as fretting fatigue proceeded (Figure 70b).

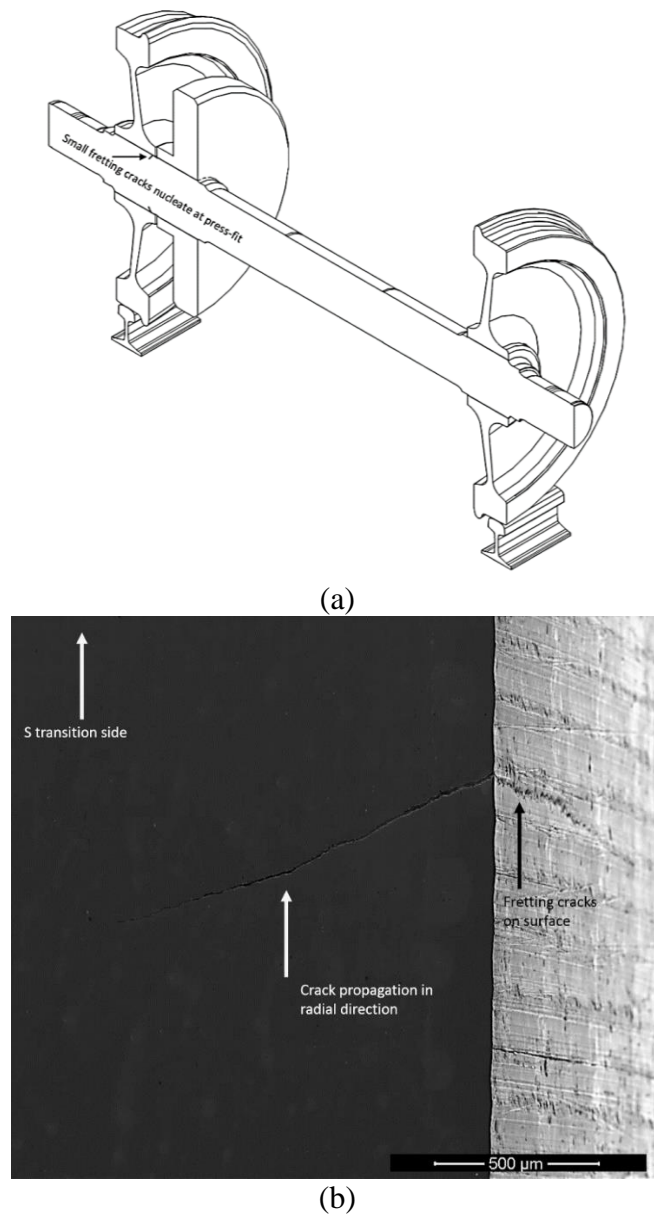
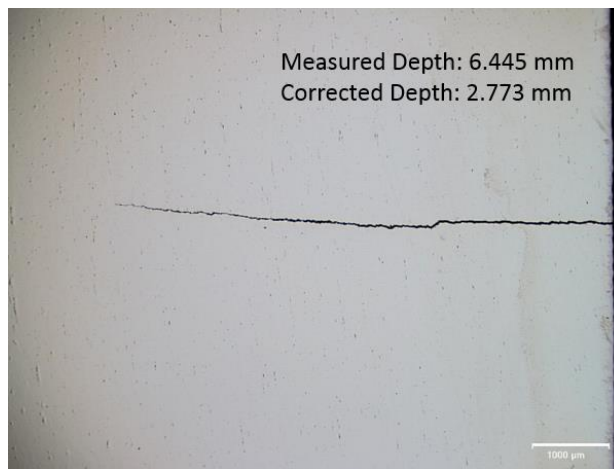


**Figure 70** Position and propagation direction of fretting cracks on (a) macro scale, (b) micro scale (x150)

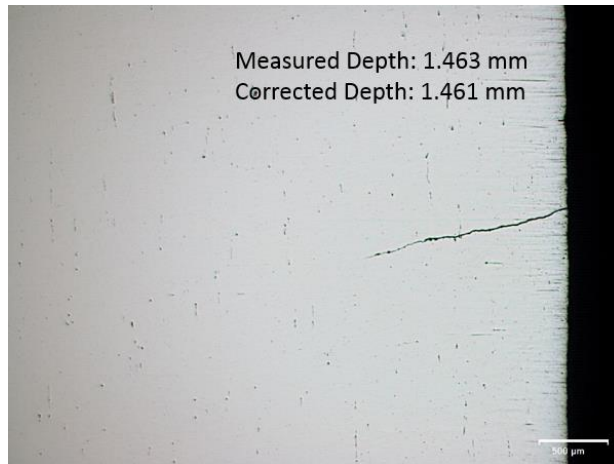
#### 4.2.1. Size and Distribution of Fretting Fatigue Cracks

Geometry and distribution of the circumferential cracks were examined by combining the crack measurements taken from the polished specimen surfaces sliced from the disk inspected by MPI.

The crack depth and angle measured on the polished surface was corrected according to the method presented in Section 3.4.2. At the locations far from the diameter, the difference between measured and corrected depth was large while it was trivial at the diameter sections as expected (Figure 71a and b).



(a)



(b)

**Figure 71** Crack measurements on planes (a) far from the diameter, and (b) close to the diameter.

Combining the measurements on the polished surface and magnetic particle inspection map, the coordinates of crack tip locations in the cylindrical coordinate system were determined.

Identified crack coordinates were placed in 3D space by using a CAD program. Separate minute cracks were differentiated from each other by examining the magnetic particle inspection photographs. Distribution of fretting cracks and their projection on the axle cross section are presented in Figure 72 -Figure 74. Two-dimensional projections of the corrected crack tip position are presented in. Maximum depth of crack is 3.03 mm for Axle A and 2.63mm for Axle B.

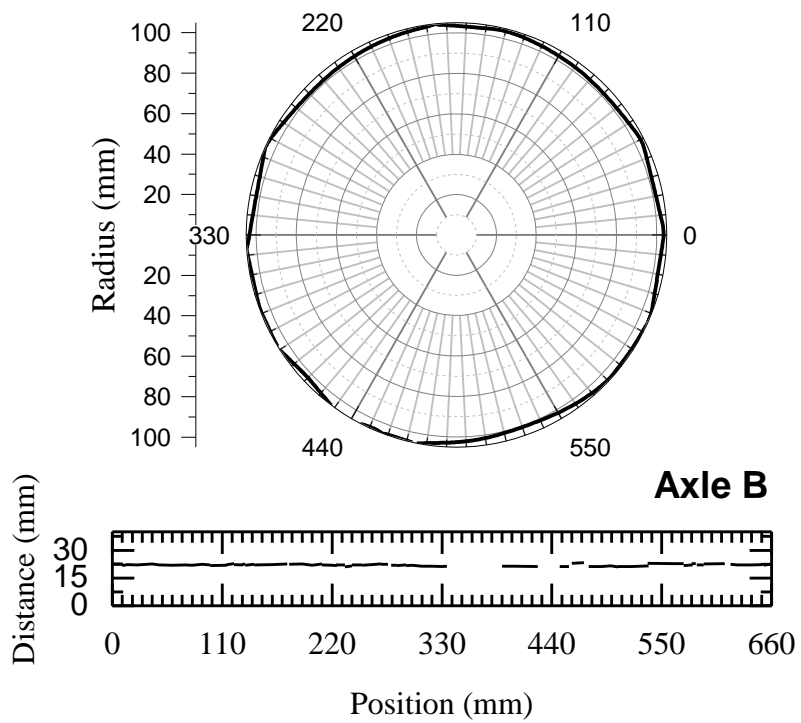
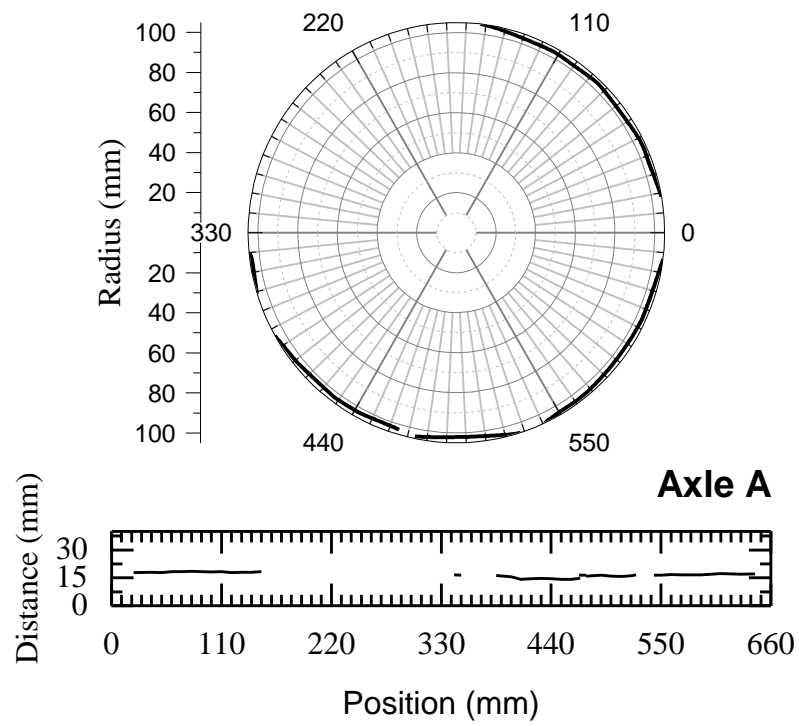


**Figure 72** Crack maps based on the corrected crack measurements.



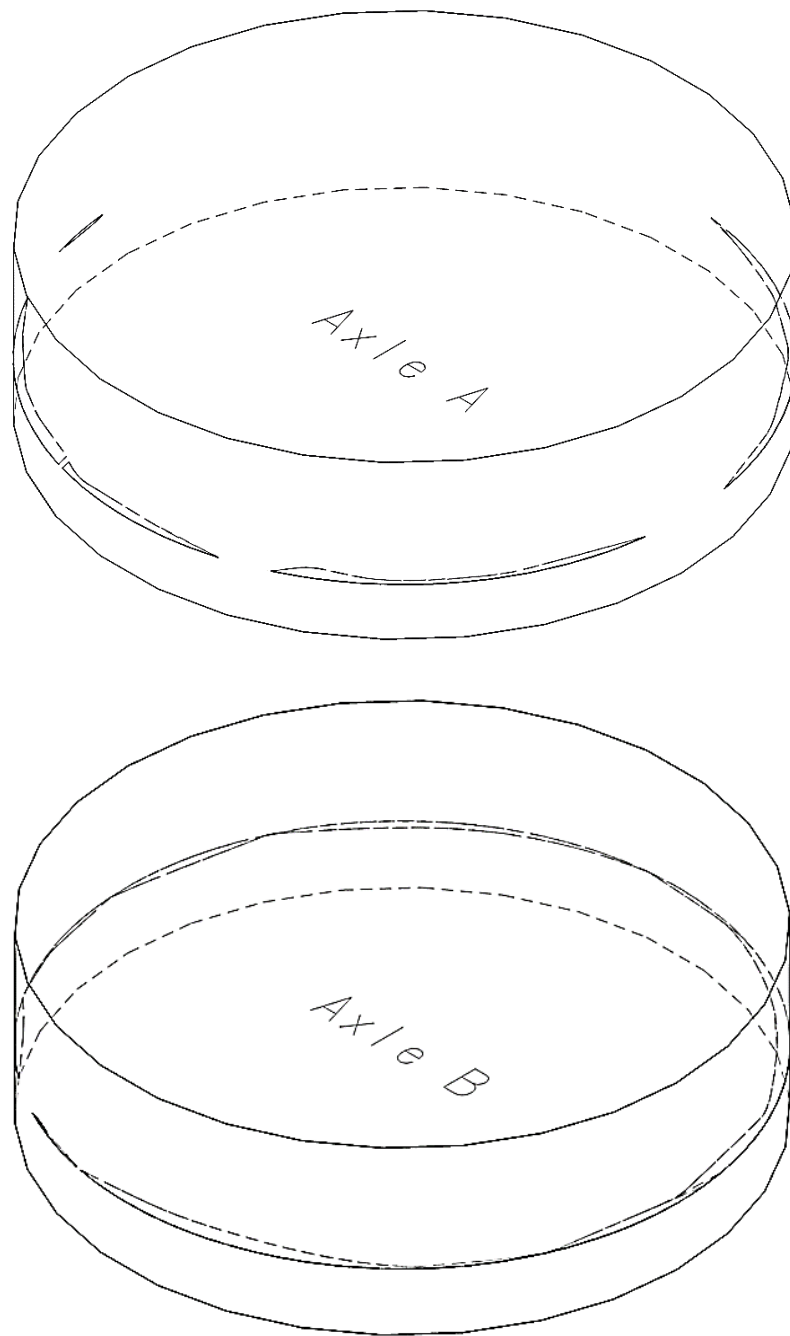


**Figure 73** 3D distribution of fatigue cracks on the sectioned 30-mm-thick discs.

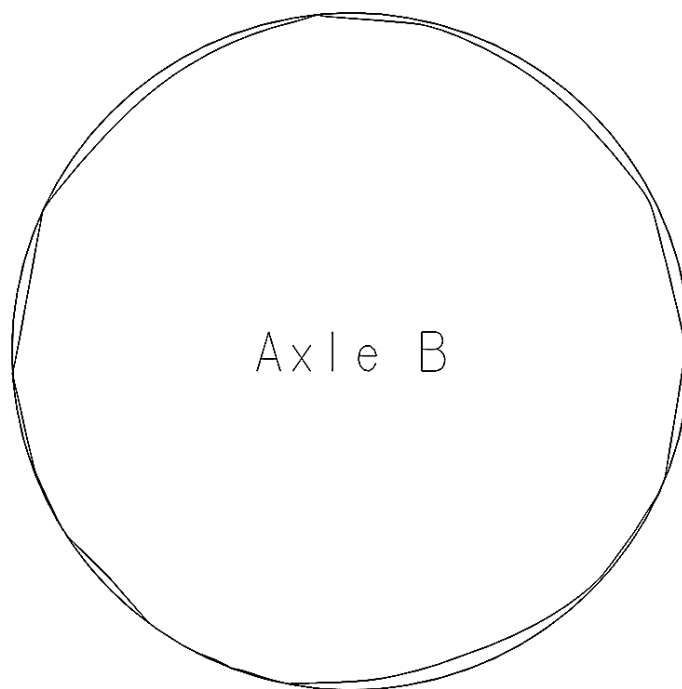
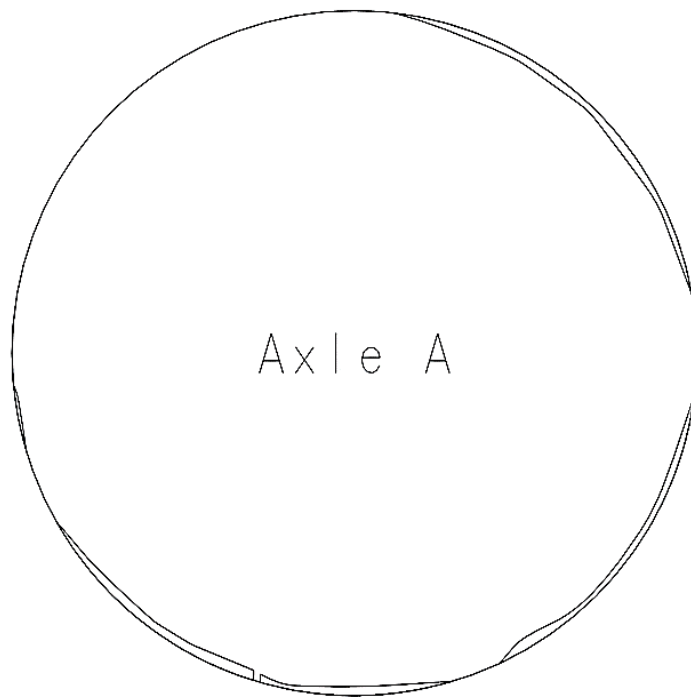


**Figure 74** Estimated projection of the circumferential cracks on the axle cross-section.

Examination of the crack depth distribution verified the coalescence of fine cracks commenced at different origins. Additionally, crack propagation rate varied at different locations. The regions with a high number of small cracks were prone to rapid propagation. Cumulative fatigue crack propagation resulted in a reduction of fatigue life drastically.

Evaluation of 3D crack maps indicated an initial propagation angle between  $60^\circ$  and  $80^\circ$  with respect to the longitudinal axis of the shaft. The statistical distribution of the initial crack angles is presented in Figure 76. The most frequent values were between  $67^\circ$  and  $72^\circ$ . The results of the crack measurements on the polished samples coinciding radial directions are given in Table 7.

An angle of  $70^\circ$  with respect to the longitudinal axis was assumed to determine the major crack behavior. Measurements on the polished samples were compatible with the crack measurement corrections. Exceptions were found at the locations where parallel crack join one another (Figure 75).

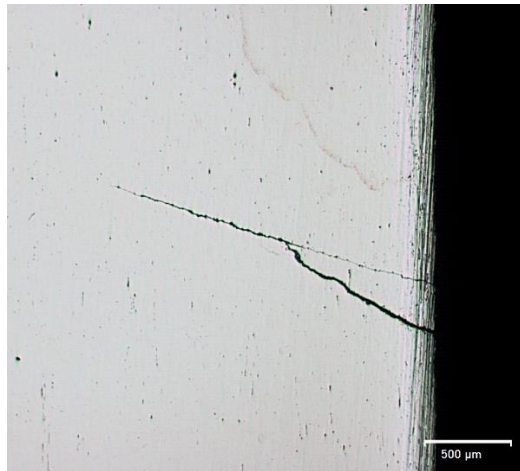


**Figure 75** Propagation of cracks initiated from different points.

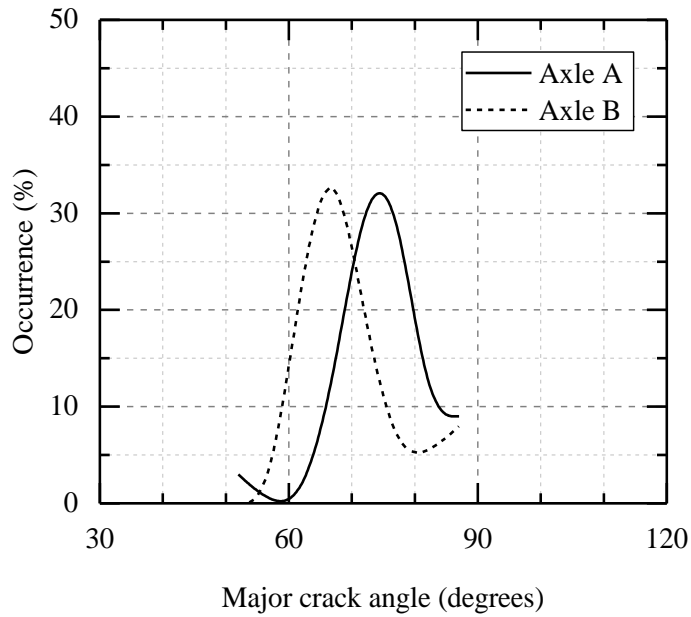


**Figure 76** The major crack angle with respect to the longitudinal axis.

**Table 7** Crack depths and positions coinciding with radial direction.

<b>Axle A</b>			
Specimen Code	Angular Position (degree)	Measured Crack Depth (mm)	Measured Crack Angle (degree)
X6	19.71	2.03	77.81
X7	217.83	1.85	75.58
X10	24.04	1.46	76.74
Z1	297.67	1.53	68.74
Z8	300.77	3.03	63.03
<b>Axle-B</b>			
Specimen Code	Angular Position (degree)	Measured Crack Depth (mm)	Measured Crack Angle (degree)
Y3	200.20	1.76	72.94
Y8	1.10	1.24	70.12
Y9	179.11	1.78	70.54
Y12	0.55	1.19	61.80
Z3	93.79	0.74	62.68
Z4	269.43	2.46	67.96
Z5	267.75	2.12	68.80
Z7	95.27	0.64	64.74

#### 4.2.2. Metallurgical Condition of the Axle Material

The metallurgical investigation was made to ensure whether the insufficient metallurgical properties do not promote the premature fatigue failure of the component. The effect of inherent defects, embrittlement or inhomogeneities which may affect the initiation and propagation of the fretting cracks was questioned.

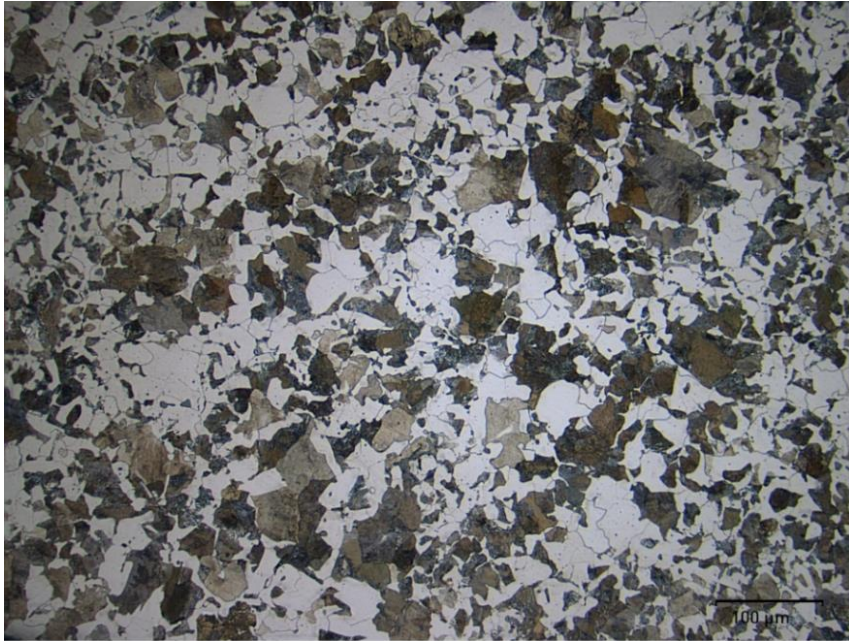
The applicability of the proposed assessment methods is slightly affected by the metallurgical condition of the axle material as long as the introduced material properties to the applied models are determined by the specimens extracted from the axle material to be used in the production. However, the proposed methods are not capable of taking the factors such as roughness, microstructure, inclusions and material defects into consideration. The ease of fatigue crack initiation is strictly related to these factors.

**Table 8** Spectral analysis (by weight %).

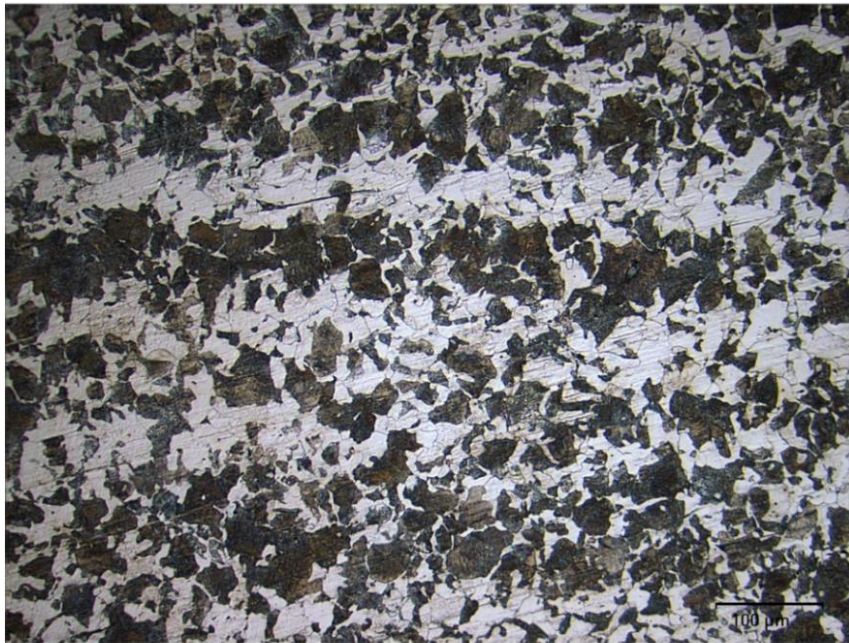
Grade	C	Si	Mn	P	S	Cr	Mo
34CrMo4	0.33	0.28	0.39	0.040	0.030	0.91	0.21
Allowable Limits [101]	0.34 -0.37	0.40	0.60- 0.90	0.025	0.035	0.90-1.20	0.15-0.30

First, the spectral analysis showed some deviations from reference limits (Table 8). Manganese content was observed to be lower than the minimum allowable limit. Normally, the insufficient manganese is associated with a decreased critical cooling rate for austenite-martensite transformation which is important for hardening applications. However, the normalized microstructure requested by the product specifications was not affected by the critical cooling rate. The metallographs showing the cut axle sections are presented in (Figure 77). Formation of ferrite bands along the longitudinal axis of the axle was clearly seen in the microstructure. The ferrite bands lie parallel with the flow direction during the hot forging process. The average grains size of the undeformed grains were 40-50  $\mu\text{m}$ .

The phosphorus content exceeded the maximum allowable limits which reduced tensile properties, % elongation and toughness.



(a)



(b)

**Figure 77** Representative micrographs on (a) transverse, (b) longitudinal plane (550x).





(a)



(b)

**Figure 78** Sulfur print of the press-fitted sections for (a) axle A, (b) axle B.

The sulfur print of the axle sections is presented in (Figure 78). Sulfide inclusions were quite widespread and frequently observed under a microscope, but they were evenly distributed and within acceptable limits.

The tensile properties and impact toughness of the samples extracted from the axles are presented in Table 9 and Figure 79. The tensile test results showed that the material exhibits medium ductility, and the tensile strength to yield strength ratio is 2.2. Comparison of the yield stress with the standard axle grades EA1N and EA4T ( 320 MPa and 350 MPa respectively) showed inferior yield properties [6]. Similarly, the impact tests results in transverse direction were slightly lower than minimum impact toughness requirements for EA1N and EA4T (25J and 20J, respectively). The reduction in yield strength and impact toughness is related to the high phosphorus and sulfur content. Additionally, ductile-to-brittle transition temperature was inside the service temperatures. The axles with major fretting fatigue cracks may not maintain structural integrity at low temperatures.

**Table 9** Tensile properties of 34CrMo4 railway axle steel.

E (GPa)	R <sub>0.2</sub> (MPa)	R <sub>m</sub> (MPa)	Elongation (%)	Area Red. (%)	K (MPa)	n
191	253	564	29	57	1446	0.34

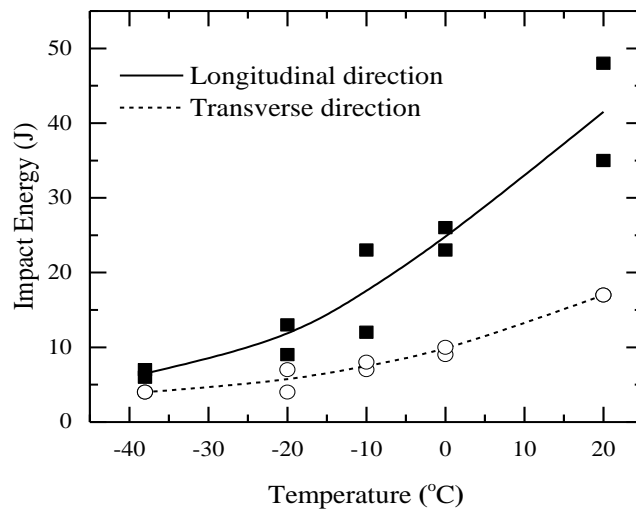


**Figure 79** Variation of impact toughness with temperature (longitudinal)



#### 4.2.3. Surface Deformations

The main mechanism of fretting crack formation is associated with the low cycle deformation observed at the heavily deformed layer [15]. Cyclic deformation caused by multi-axial surface stresses are considered as the source of fretting cracks [10, 24, 102]. The applicability of strain-life based multiaxial fatigue models to determine the number of cycles has been discussed in the literature [10, 15, 42, 50]. Despite the success in predicting the location locations of fatigue initiation, the applied models are not sufficient to describe the number of cycles for initiation of fretting cracks. Improving fatigue crack initiation resistance through surface modifications is used effectively in practice [9, 14].

Cyclic hardening of the 34CrMo4 has been investigated through low cycle fatigue tests. The cyclic stress –strain curve and its comparison to the monotonic tensile properties are given in Figure 80. The constants of the cyclic plasticity equation were measured as  $K' = 1447.8 \text{ MPa}$  and  $n' = 0.29$ . Cyclic hardening was observed.

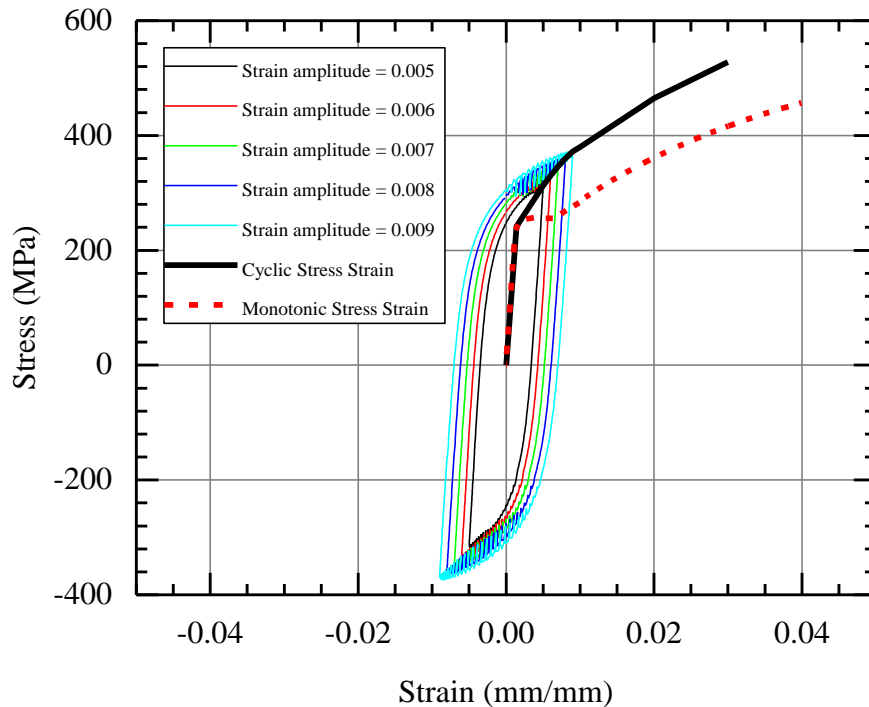


**Figure 80** Cyclic stress- strain curve and monotonic curves for 34CrMo4.

Hardness profile measurements along the radial direction showed no remarkable hardness change at the outer diameter. The average hardness was found to be  $169 \pm 4$  HV (30) for Axle A and  $179 \pm 4$  HV(30) for Axle B.

SEM investigations on the damaged axles showed small cracks originated from the heavily deformed surface layer. The nominal thickness of the deformed surface layer is measured as  $5 \mu\text{m}$  (Figure 81, region b). Small fretting cracks emanating from the deformed surface layer intersect and form a delta-shaped crack initiation zone at the crack origin (Figure 81, region a).

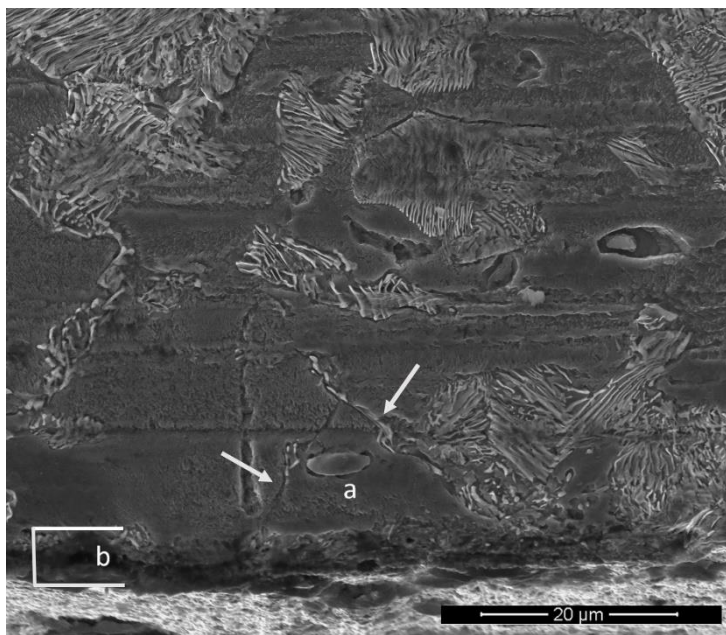


**Figure 81** (a) Formation of triangular region between two critical planes of crack propagation, (b) thickness of the deformed layer (8000x)

Accumulation of small non-propagating cracks were more frequent in the vicinity of major cracks (Figure 82). The typical sizes of the arrested cracks are about  $50 \mu\text{m}$ . Additional surface damage is associated with debris entrapment in the following stages of fretting [14]. Examination of major crack initiation sites shows that the triangular zone detach as fretting fatigue proceeds (Figure 82 and Figure 83).

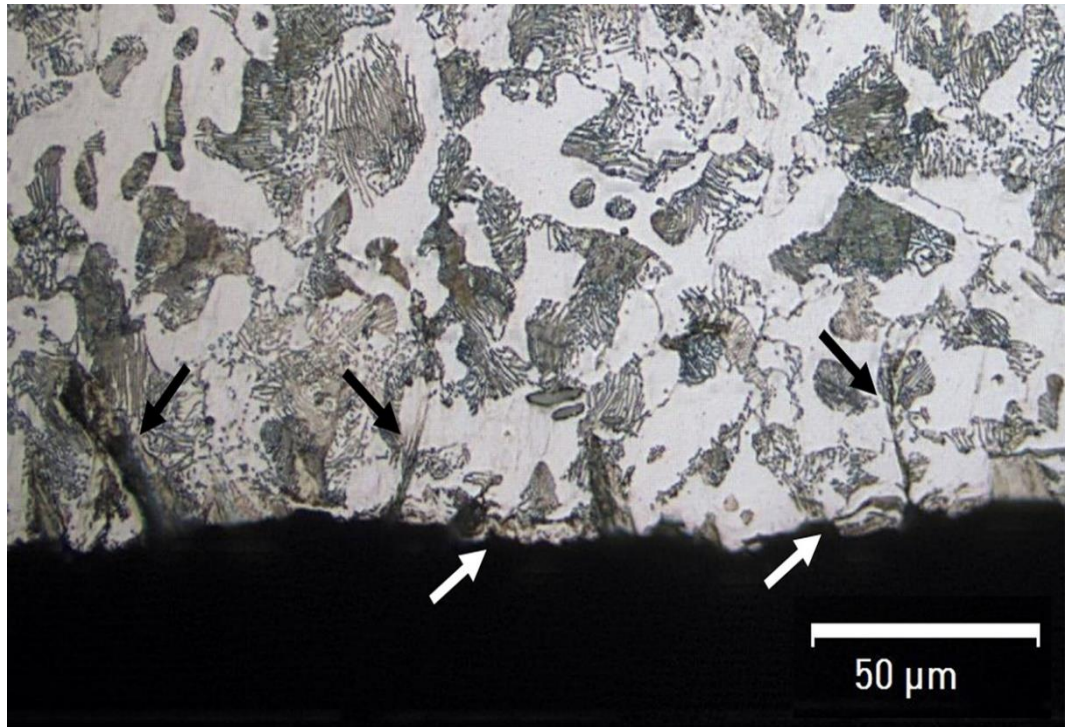


**Figure 82** Propagating and non-propagating cracks at the material surface (x1000).

Another important result obtained from the fractography is that the primary cracks tend to form at the pearlite-ferrite phase boundaries; i.e. the initiation stage of the fretting crack is affected by the lamellar morphology of pearlite (Figure 81 and Figure 83). Separation of pearlite-ferrite grain boundaries during crack initiation can be clearly seen despite the trans-granular advance of the crack during propagation (Figure 94). The sensitivity of pearlitic microstructure is explained by the restricted deformability of cementite layer [43]. A similar disadvantage of the lamellar microstructure against fretting fatigue initiation is reported in the literature [103].

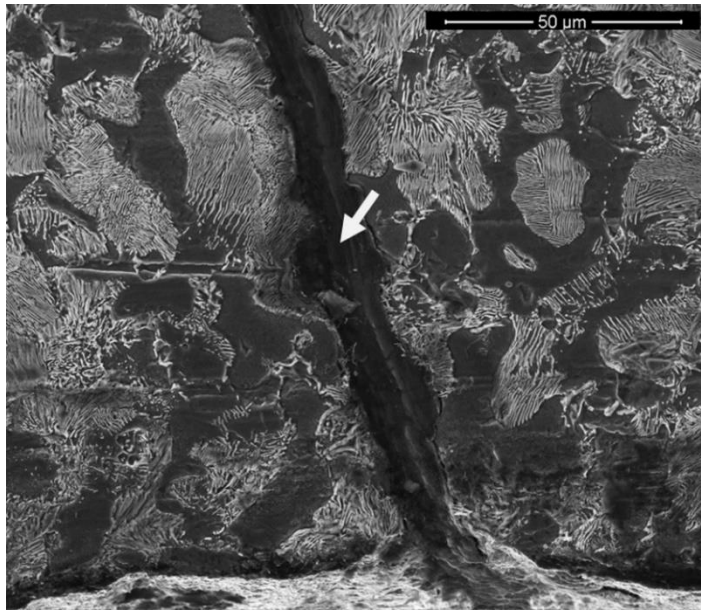


**Figure 83** Debris accumulation inside major crack (x2000).

The major crack path shows that accumulation of oxide products between the crack faces continues in the middle part of crack propagation (Figure 83 and Figure 84). Source of debris found inside the cracks might be due to rubbing of the crack surfaces. Non-conforming profile of the crack faces also indicates the possibility of rubbing.

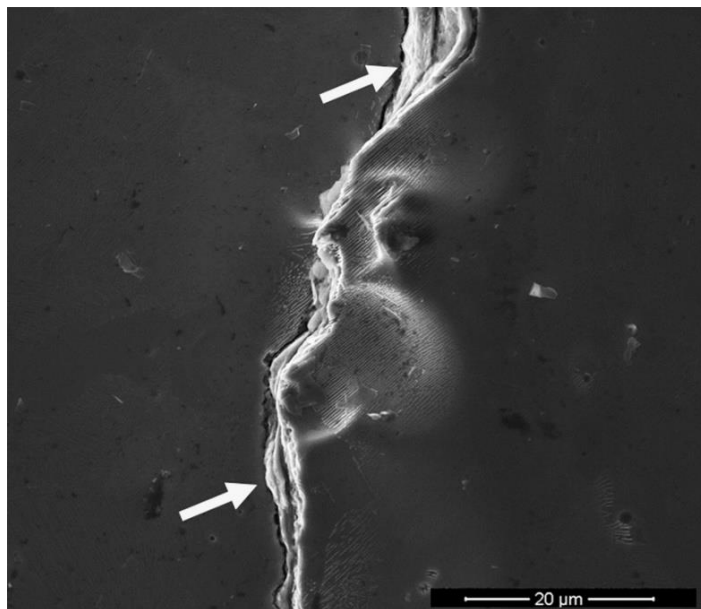


**Figure 84** Debris accumulation between the crack faces (x4000)

#### 4.2.3.1. *Effect of Surface Roughness*

Another parameter affecting the friction between the contact surfaces is roughness. SEM examinations on the damaged axle's surface showed a flattened surface profile Figure 85.

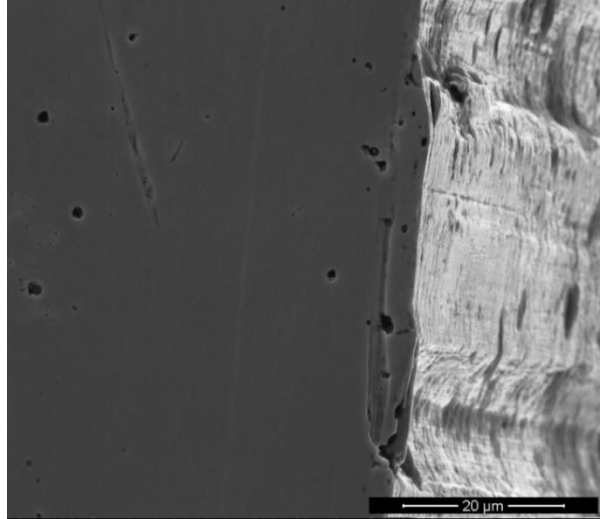


**Figure 85** Deformation and crack initiation at surface asperities (Axle B).

The surface roughness reduces gradually as surface profile changes. Plastically deformed surface asperities detach from the surface as debris leaving behind a surface crater which later acts as a nucleation site for fretting fatigue cracks. Morphology of surface a cavity found on one of the examined axles is shown in Figure 86.

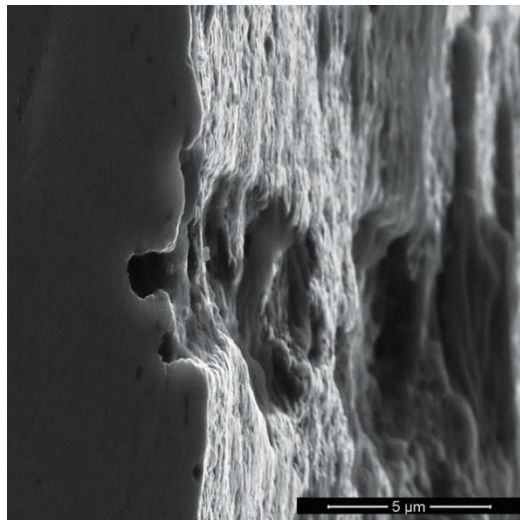


**Figure 86** SEM micrograph showing fretting damage at the surface.

Surface irregularities such as material defects, asperities, inclusions and grain boundaries, are the unexceptional contributors to the fretting damage [15, 64, 103, 104]. For this reason, the rough surface finish at the beginning may deteriorate faster despite better mechanical locking. The intense debris accumulation causes further damage by the abrasive effect. The fine surface finish improves fretting fatigue performance [13].

#### 4.2.3.2. *Effect of Metallic Inclusions*

Analytical study of fretting damage shows that the fatigue index just below the surface may reach values higher than those at the surface in some cases [16]. Consequently, sub-surface defects and inclusions coming from the forging/casting operations may give rise or contribute to the initiation of fretting cracks. Susceptibility of sub-surface inclusions to cracking was investigated on the polished and etched sections. Separation of sub-surface grain boundaries and sulfide inclusions were observed in some regions which are approximately 50  $\mu\text{m}$  below the axle surface (Figure 87).

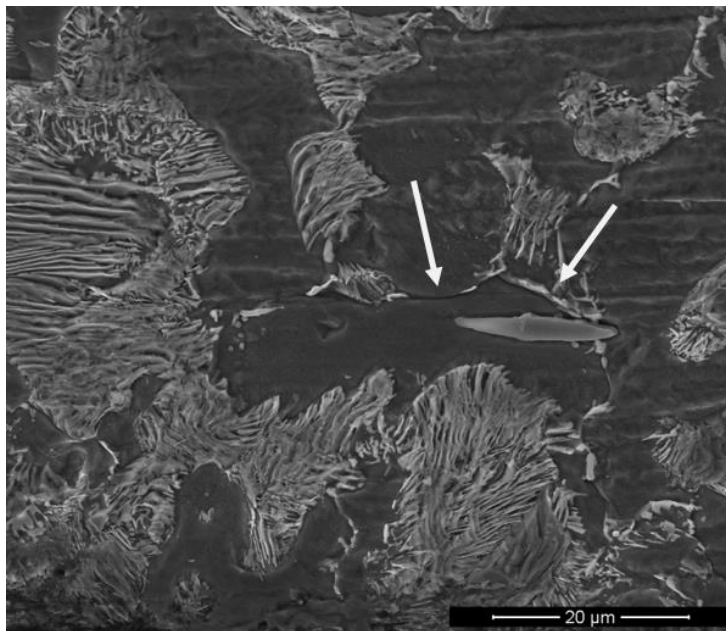


**Figure 87** Sub-surface cracking at grain boundaries.



The reason for the separation is explained as a result of mismatching mechanical properties of the ferritic-pearlitic matrix and deformable MnS inclusions [105]. However, the parallel propagation of subsurface defects is less critical when compared to the crack propagation in the radial direction (Figure 88). Separation of sulfide inclusions and grain boundaries are observed at the subsurface (Figure 87 and 88).

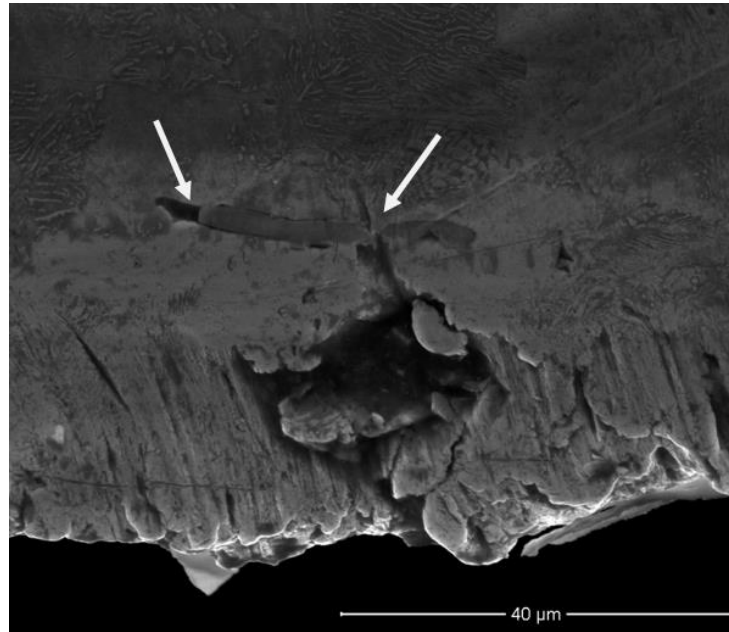


**Figure 88** MnS inclusions intersected by a surface crack.

#### **4.2.4. Crack Propagation Plane**

The investigation of the crack propagation plane was conducted on a surface achieved by separating the crack faces by an external load (Figure 89). Macro appearance showed a rusty layer near the surface. The rusty region is preceded by a fresh fracture surface which was an indication of delayed propagation. Additionally, the formation of a boundary separating the propagation plane into two distinct regions is clearly seen. The change of propagation plane at this boundary is incorporated with the deflection of the crack tip during propagation. Crack tip deflections are associated with the transition between different modes of crack propagation [91].

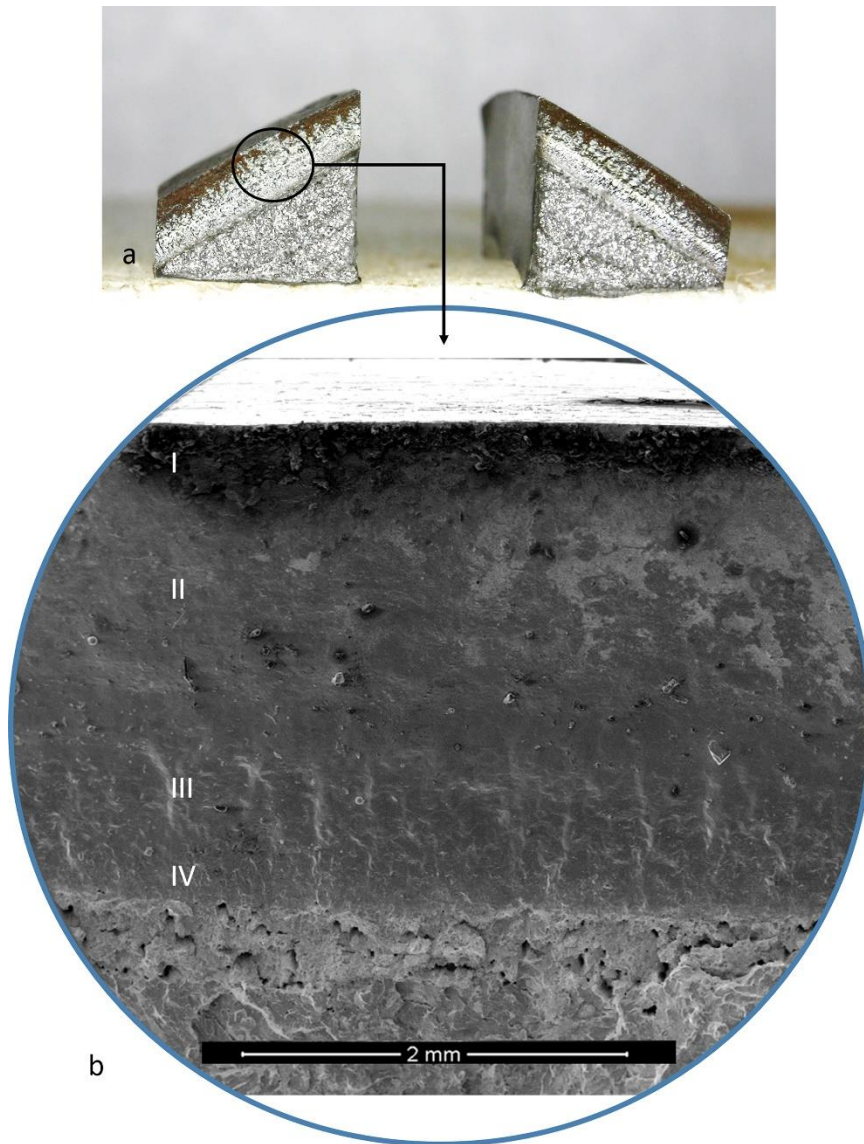


**Figure 89** Macrograph: rubbing in the damaged section.

The SEM micrographs of the propagation plane are given in Figure 89b, where four different regions are indicated.

The oxidation marks in the first region were visible from the surface to 300  $\mu\text{m}$  depth. The delayed propagation at this stage reveals that the small fretting cracks remain non-propagated until a threshold condition has been achieved. In practice, these shallow cracks are not detected easily by ultrasonic inspection.



Severe rubbing in the second region exists down to 2.2 mm depth. Effect of rubbing reduces as the crack propagates beyond 1.66 mm depth (Figure 90, region III). A wavy appearance of the rubbed section might be due to the rubbed “ratcheting marks” which are typical for the multiple site initiation of fatigue cracks [21, 106, 107].

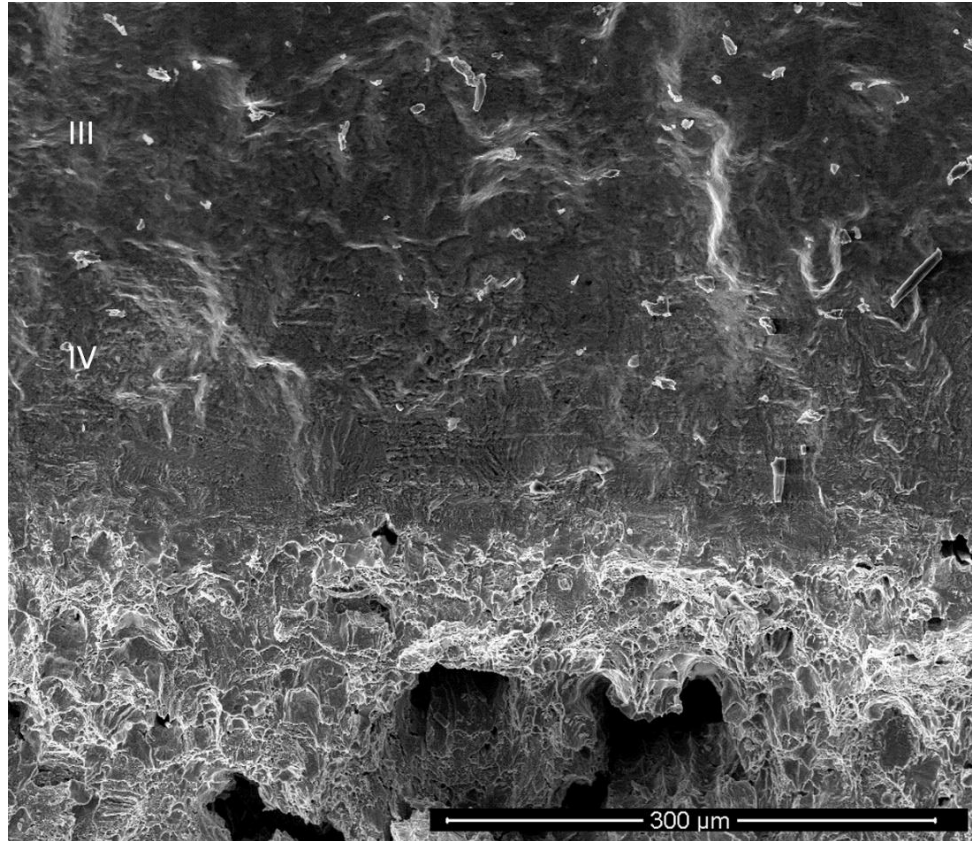
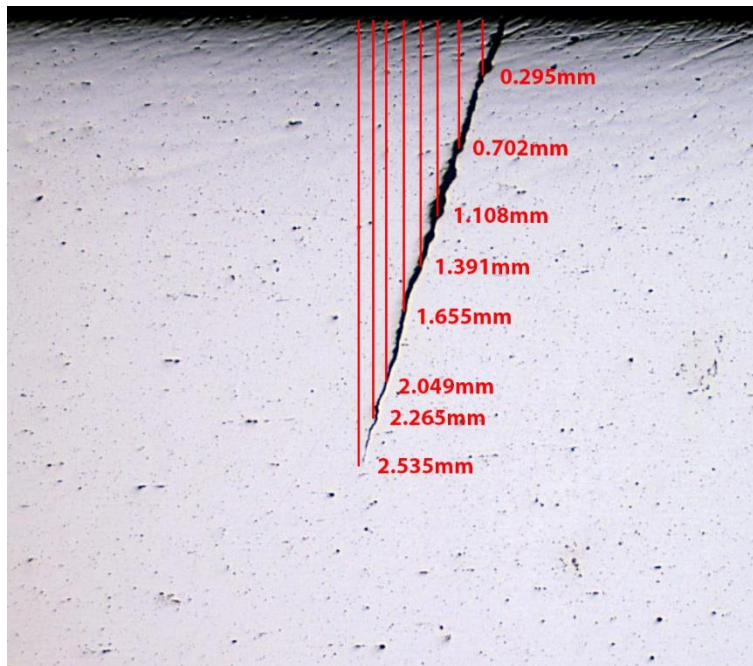
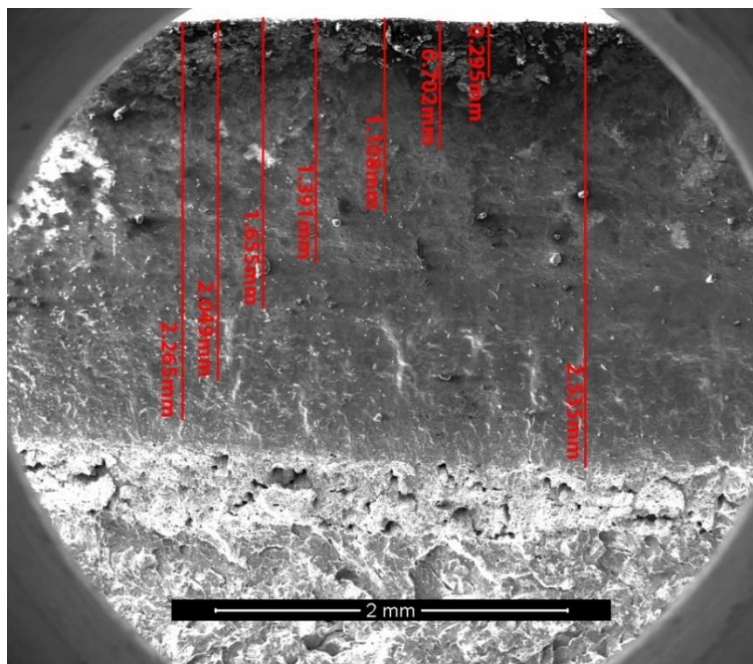


**Figure 90** Transition from rubbing to the indications of axial fatigue (x500).

The existence of the fatigue striations in the fourth region shows that a transition from rubbing to tearing mode emerges as crack depth reaches to 2.2mm (Figure 90, region IV). A stable crack growth condition had been achieved before the crack was inspected at 2.60 mm depth. Mode I propagation under the influence of the major bending stress after reaching a certain depth was reported to be typical for the axle failures [4, 5, 17]. Crack tip deflections are observed at different stages of crack propagation showing the transition between the various modes of fracture (Figure 91a). A comparison of polished surface measurements with crack plane measurements is given in Figure 91a and b. A remarkable deflection from the initial linear path is seen at 1600 μm depth.



(a)



(b)

**Figure 91** Crack depth comparisons on (a) the polished surface (b) fracture plane

### 4.3. Multiaxial Fatigue Assessment

The fatigue limit for railway axles is determined according to the test methods presented in international standards.[5, 6, 9]. Comparison of fatigue tests with notched and plain specimens is used to determine the allowable fatigue limits of the axle sections and qualified by the full-scale tests [5]. However, laboratory tests are not sufficient alone to represent the multiaxial loading presented in the stress analysis. Multiaxial fatigue models offer methods to express the complex loadings unique fatigue index parameters.

#### 4.3.1. Stress-Based Approach

Incorporation of uniaxial fatigue data with the cyclic stress computed by the FEA was achieved through the application of stress-based multiaxial fatigue models. The modified Dang-Van and Liu-Mahadevan models were used in the analysis. Additionally, the results obtained from the multiaxial fatigue analysis and Kitagawa-Takahashi diagrams were used to determine an allowable defect size.

##### 4.3.1.1. Uniaxial Fatigue Tests

Uniaxial fatigue tests are required for the determination of empirical constants in Dang-Van and Liu-Mahadevan multiaxial fatigue models. The fatigue limits for reversed tension ( $R=-1$ ), tension to tension ( $R=0$ ) were determined by staircase method with a failure probability of 10% within 95 % confidence interval. The reversed shear ( $R=-1$ ) limit was taken as 70% of the axially reversed fatigue limit [76]. The fatigue limit for axial and shear loading are presented in Table 10. Wöhler curves for the axial tests are presented in Figure 92 and Figure 93. The ratio of the reversed fatigue limit to tension-tension fatigue limit ( $\sigma_{w,R=-1} / \sigma_{w,R=0}$ ) was found to be 0.75. Maximum run-out stress during the test exceeded the yield strength of the material.

**Table 10** Fatigue limits under tension and shear loading (*10% prob. within 95% conf.*).

Loading	Stress Ratio	Stress Amplitude (MPa)
Tension	0	173
Tension	-1	232
Shear	-1	162

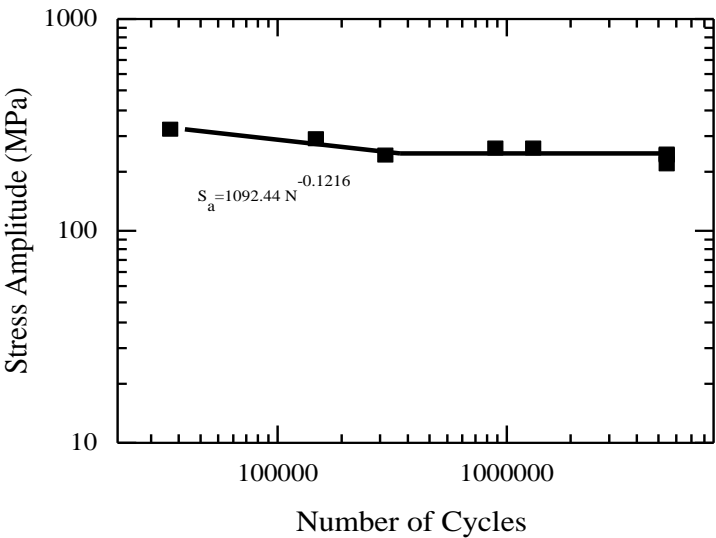


**Figure 92** S-N diagram of the 34CrMo4 railway axle material (R=-1)

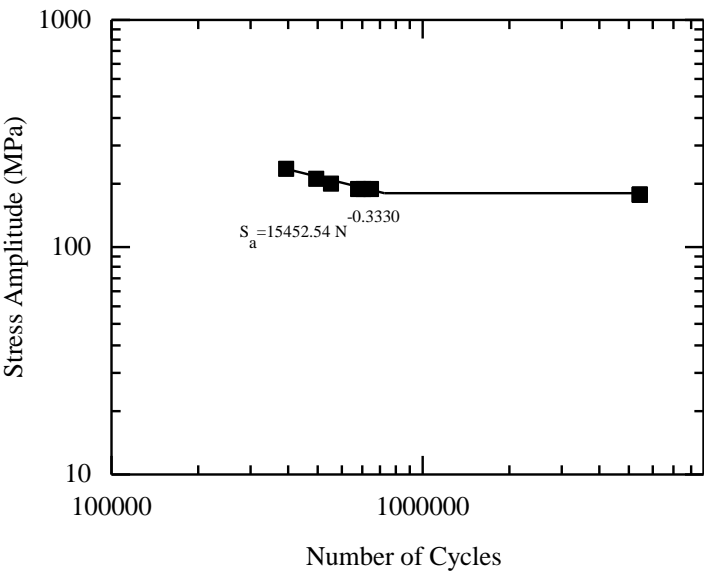


**Figure 93** S-N diagram of the 34CrMo4 railway axle material (R=0)

Goodman and Haigh's diagrams based on the specimen scale tests are presented in Figure 94 and Figure 95. The safety locus expressed by the yield and Goodman lines indicated that the design loads are selected in the safe region. The fatigue limit for the reversed axial stress was very close to the yield stress but still below the 250 MPa which is described as the minimum limit for EA1N and EA4T [6].

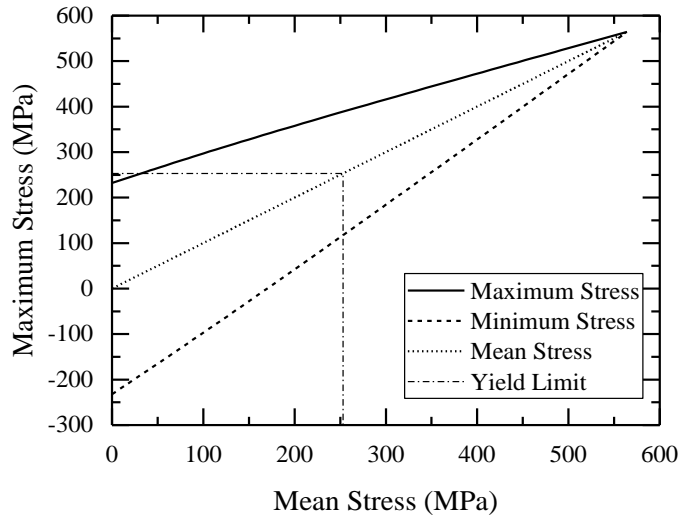


**Figure 94** Goodman diagram of the normalized 34CrMo4 steel

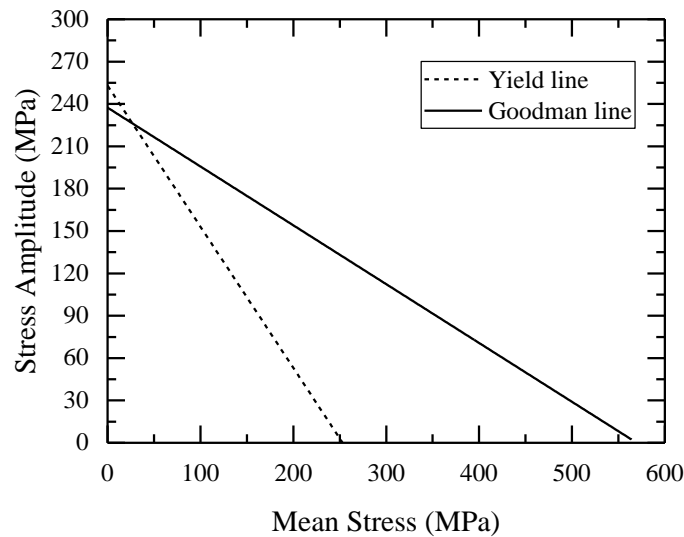


**Figure 95** Haigh diagram of the normalized 34CrMo4 steel

#### 4.3.1.2. Kitagawa - Takahashi Analysis

The characteristic short crack limit for 34CrMo4 was characterized by rotating beam fatigue testing on defect-machined samples. Kitagawa diagrams were constructed based on the Murakami's square root area method. The obtained Kitagawa diagram is presented in Figure 96.

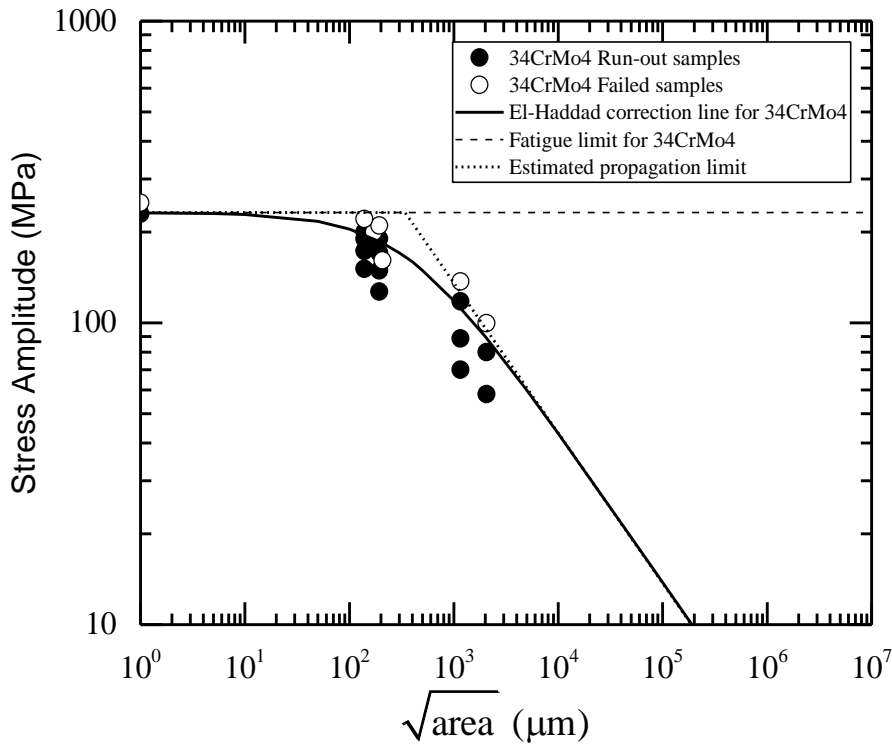


**Figure 96** Kitagawa diagram (normalized 34CrMo4)

El-Haddad correction curve was fitted to the experimental data to express a size relation that can be used in analytical studies (Equation 4.1).

$$\Delta S_w = \Delta S_{w0} \sqrt{\frac{\sqrt{area_0}}{\sqrt{area} + \sqrt{area_0}}} \quad 4.1$$

where  $\sqrt{\text{area}_0}$  is the short crack limit,  $S_{w0}$  is the original fatigue limit (232 MPa), and  $S_w$  is the fatigue limit of the sample including a defect measured in “square root of area” parameter.

The short crack limit expressed by the El-Haddad relation was found to be 352  $\mu\text{m}$ , corresponding to 110  $\mu\text{m}$  of depth for small cracks [64]. The estimated threshold intensity factor for small cracks found as  $3.61 \text{ MPa.m}^{1/2}$  by Equation 4.2.

$$K_{I,th} = 0.65 S_w \sqrt{\pi \sqrt{\text{area}_0}} \quad (4.2)$$

Fatigue strength, which can be changed through toughening or surface hardening, is more effective on the threshold intensity factor than the  $\sqrt{\text{area}_0}$  term. The contribution of local compressive stresses may increase the limits for threshold condition. On the contrary, fretting crack initiation contributed by the factors presented in the fractographic discussion may shorten the period before reaching the threshold conditions.

#### 4.3.1.3. *Dang –Van Multiaxial Fatigue Model*

Application of Dang Van model to the fretting problem is based on the idea of mesoscale stresses. The Dang-Van tool predicts deviatoric component of residual stress tensor ( $\rho^*$ ) computed by drawing the center of minimum circumscribing ellipse traveled by the macro stress tensor  $\Sigma(t)$ .

Mesoscale stress tensor is given by Equation 4.3

$$\sigma_{ij}(t) = \Sigma_{ij}(t) + \text{dev} \rho^* \quad (4.3)$$

In the mesoscale approach, the Dang Van model seeks for the time-dependent path of hydrostatic stress and shear amplitude. Equation 4.4 expresses the fatigue index in Dang-Van criterion

$$\tau(t) + a\sigma_h(t) = b \quad (4.4)$$

Constants of the Dang Van equation (a and b) were calculated by combining the fatigue test results conducted at different loading regimes. Limiting conditions for multiaxial

fatigue limit were drawn by the straight line passing through the above the stress path during the uniaxial test. The Dang-Van constants were determined as  $a=0.65$  and  $b=160.35$  based on the fatigue limits of the normalized 34CrMo4 (Figure 97).

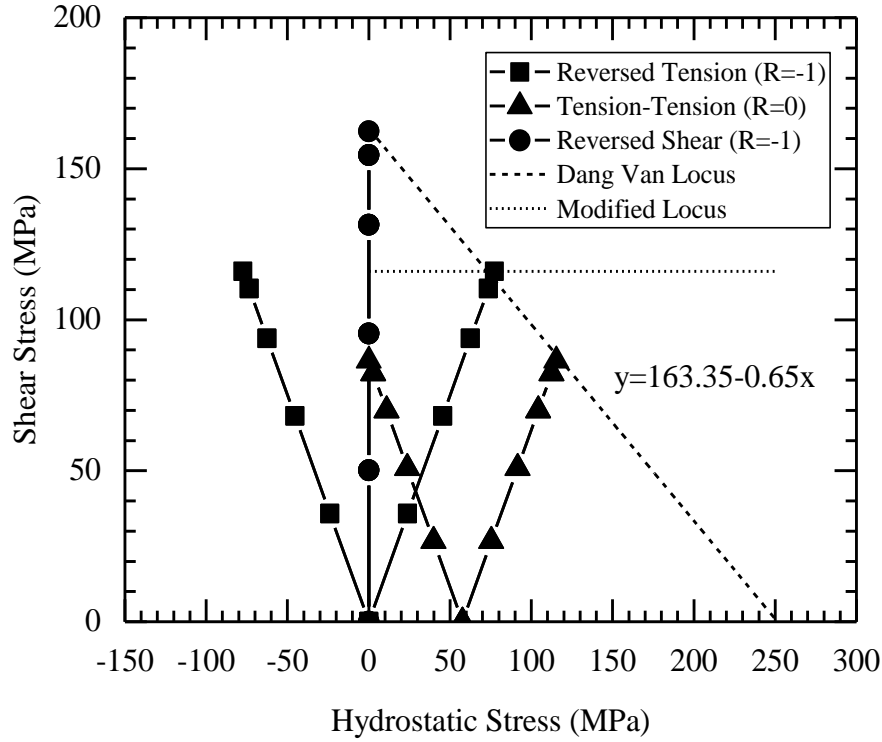


**Figure 97** Determination of Dang-Van constants and application of modified locus for the normalized 34CrMo4.

Besides, an additional “modified locus” was defined based on the results presented by Desimone et. al. [108]. The modified locus has been imposed to converge effect of localized shakedown in mesoscale [108]. The fatigue failure is observed when the “hydrostatic stress vs. shear stress” path exceeds the limits presented by the Dang Van locus and the modified locus.

In this study, shifts of the Dang Van locus and modified locus with an existing defect were linked with the decrease of fatigue limit presented by the El-Haddad equation. Thus, determination of allowable defect size by using the Dang- Van locus becomes possible.



Application of Dang Van locus on the stress path determined at different points, and different defect size is presented in Figure 98.

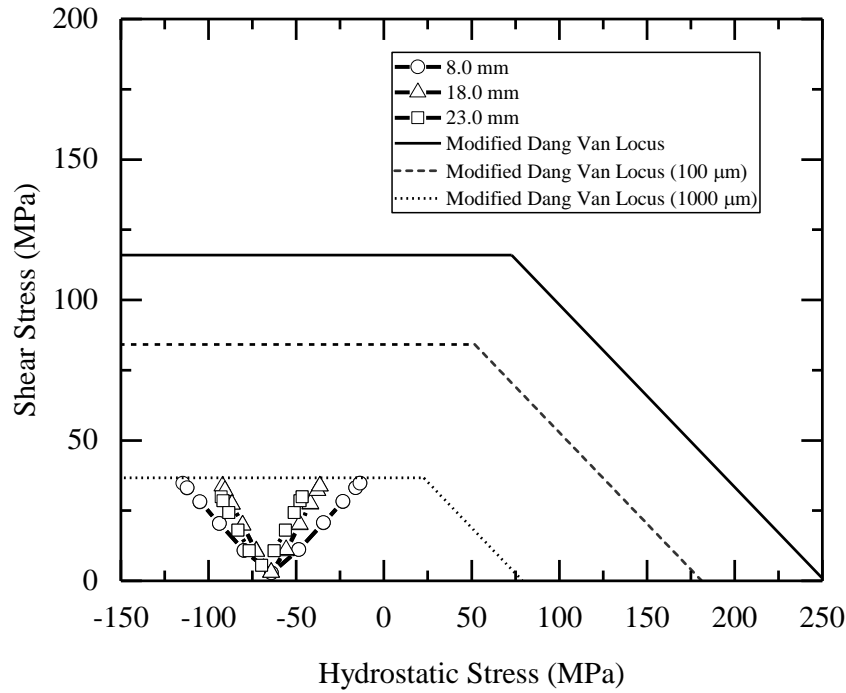


**Figure 98** Dang Van criterion and original locus.at points on the contact area

In Figure 98, an original locus for the axles including 100  $\mu\text{m}$ , and 1000  $\mu\text{m}$  cracks are demonstrated based on the reduced fatigue strengths obtained by Kitagawa analysis. Corresponding  $\sqrt{\text{area}}$  values for 100  $\mu\text{m}$  and 1000  $\mu\text{m}$  cracks are 316.23  $\mu\text{m}$  and 3162.28  $\mu\text{m}$ , respectively.

The reduced fatigue strength due to present defects was computed by using El-Haddad correction curve [60, 109]. The corresponding fatigue strengths were 168 MPa and 73 MPa for 100  $\mu\text{m}$  and 1000  $\mu\text{m}$  cracks, respectively.

Referencing to El-Haddad correction equation and modified Dang Van locus limitations, the distribution of allowable defect size along the contact area were constructed for different friction regimes (Figure 99).

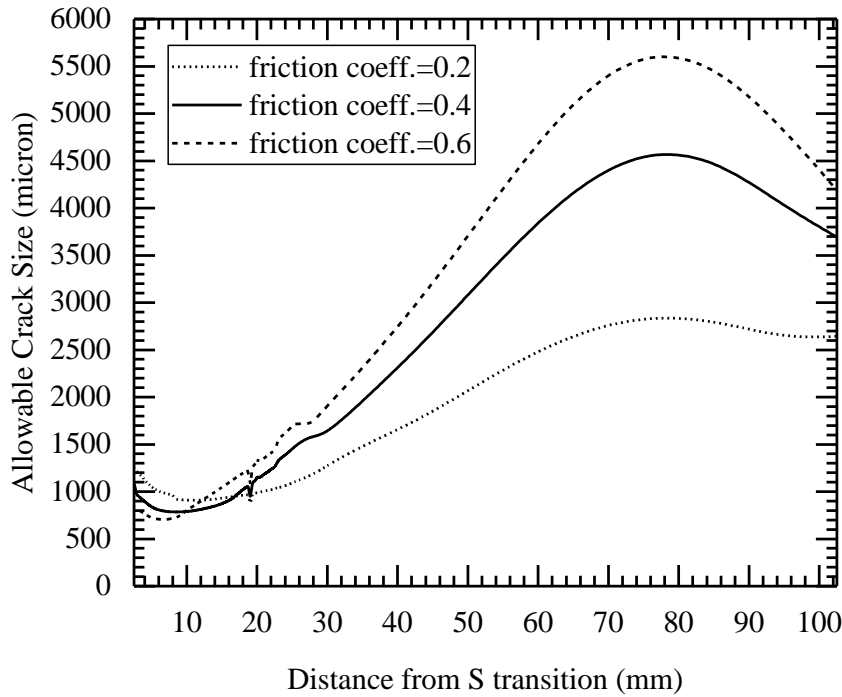


**Figure 99** Comparison of the allowable crack size along the contact surface according to Dang Van multiaxial fatigue criterion.

The results presented in Figure 99 show that the sensitive region for multiaxial fatigue damage shifts towards the interior part of the press fit. Additionally, the first 5-25 mm from the S transition is sensitive to the fretting damage as friction coefficient at the press fit decreases. Defects reaching to the 600-900  $\mu\text{m}$  depth are considered as propagating cracks according to the results obtained by Dang-Van analysis. Predictions made by modified Dang Van model is, thus, consistent with the fractographic measurements.

#### 4.3.1.4. Liu – Mahadevan Multiaxial Fatigue Model

The fatigue index and the critical planes for the given stress distribution along the press fit contact have been computed by using the Liu-Mahadevan multiaxial fatigue model. [75, 110]. The allowable defect size at each surface node has been determined by using the small crack data obtained by Kitagawa analysis (Figure 100).

The fatigue index suggested by the model is computed on the critical plane which is the maximum normal stress plane of the given load path.

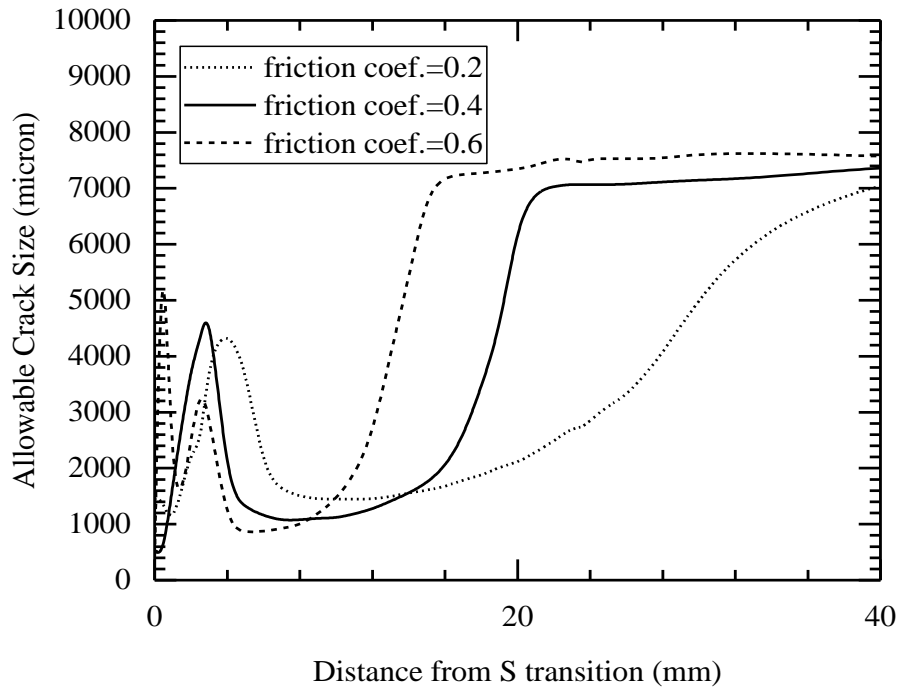


**Figure 100** Application of Liu Mahadevan criterion at different locations along the contact area (under the nominal bending stress of 120 MPa).

Similar to the results of the Dang Van analysis, the Liu-Mahadevan model presented a shift of sensitive region towards the mid-section of the press-fit as friction coefficient decreases. Similarly, the first 5-20 mm of the press-fit was found to be critical for the fatigue propagation. The size limit for fatigue crack propagation is estimated to be 900-1300  $\mu\text{m}$  (in depth) within the examined region. The obtained results are more conservative than those achieved by Dang Van model. Fractographic evidence showed the transition to Mode I propagation at a crack length of 1.6mm. Certainly, the short crack propagation under the influence of mixed mode loading starts at shorter crack depths which are probably comparable in size with the results obtained by Liu-Mahadevan model.

### 4.3.2. Fracture Mechanics Based Approach

Fracture mechanics based approach was used in the multiaxial fatigue assessment. A crack analog method was applied by calculating the stress intensity factors at the critical cracks by using weight function method. The maximum tangential stress and an equivalent stress intensity factor at different stages of crack propagation is compared with the threshold conditions determined by Kitagawa analysis and fatigue crack growth rate tests.

#### 4.3.2.1. Fracture Toughness Tests

Fracture toughness tests were conducted to investigate the material behavior and crack tip plasticity during crack propagation. Load vs. crack mouth opening displacement (CMOD) curves obtained at room temperature (25°C) and -10°C for 20mm thick SEN(B) specimens are presented in Figure 101.

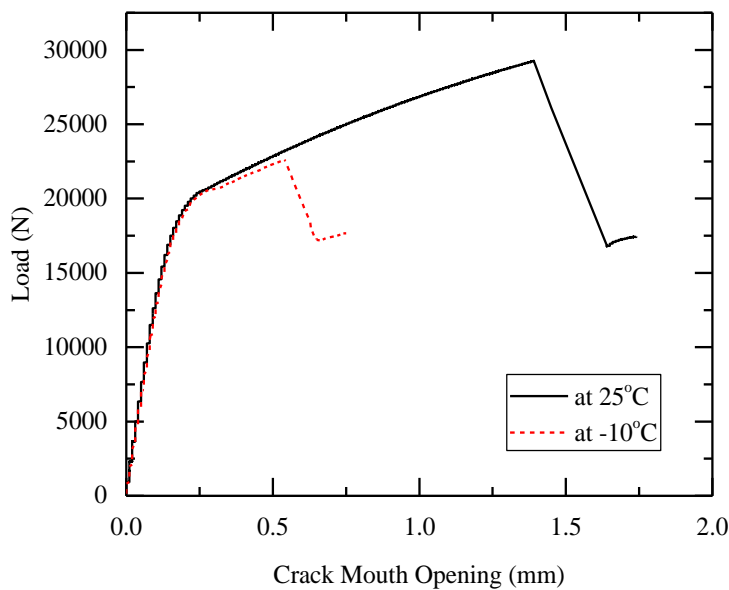


**Figure 101** Load vs. CMOD graphs for 34CrMo4 at different temperatures

The crack tip opening displacements and the maximum achieved stress intensity factors at test temperatures are presented in Table 11. The fracture toughness at low

temperature is less than one-third of the fracture toughness at the room temperature. The sudden loss of toughness at low temperature may accelerate crack propagation and cause sudden loss of toughness and crack tip plasticity.

**Table 11** Results of the fracture toughness tests (ISO 12135)

Temperature (°C)	K <sub>max</sub> (MPa.m <sup>1/2</sup> )	δ <sub>20</sub> (mm)
20	79	0.366
-10	62	0.117

The invalid plain strain fracture toughness ( $K_Q$ ) is ca. 55-58 MPa.m<sup>1/2</sup> which is comparable with the other invalid measurements from EA1N and EA4T axle steels (52 MPa.m<sup>1/2</sup> and 73 MPa.m<sup>1/2</sup>, respectively) [9]. However, the test results were thickness dependent since the elastic plane strain condition were not satisfied [94].

The reduction of fracture toughness with temperature is in agreement with the impact toughness test results. The the amount of tearing shown in Figure 102 verify the reduced crack tip plasticity at low temperatures.

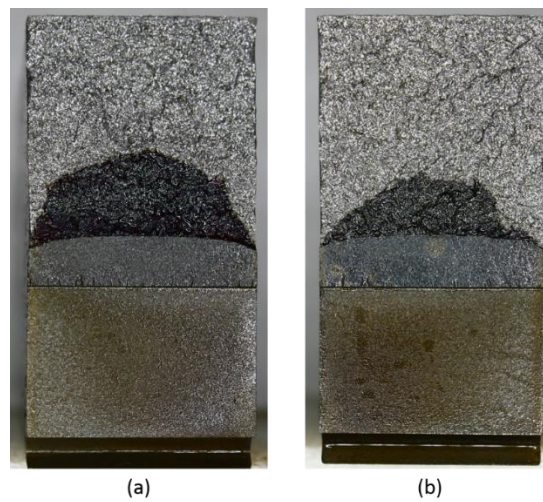


**Figure 102** Fracture surface appearances at (a) room temperature, and (b) -10°C

#### 4.3.2.2. Fatigue Crack Growth Rate

Fatigue crack growth rate for two identical SEN(B) specimens with a stress ratio ( $R=0.1$ ) and different loading amplitudes are given in (Figure 103). The minimum threshold limit were found to be  $16.40 \text{ MPa.m}^{1/2}$ . In literature, the threshold limit for EA1N and EA4T with similar specimen configuration (SE(B) specimens with  $R=0.1$ ) were presented as  $8.90 \text{ MPa.m}^{1/2}$  and  $6.28 \text{ MPa.m}^{1/2}$ , respectively [35]. The effect of crack closure can be inferred from the comparison of threshold limits in Figure 103. The obtained threshold limits are questionable because they are highly affected by the crack closure and very high when compared to the results from EA1N and EA4T samples. The obtained threshold limits are quite higher than that of small cracks obtained by Kitagawa test.

The Paris equation constants were calculated as  $C= 3.24 \times 10^{-11} ((\text{MPa.m}^{1/2})^{-2.67} \text{m.cycle}^{-1})$  and  $m=2.67$ . These values were used to estimate crack propagation paths and remaining life assessment of the axles. The rate of stable fatigue crack growth is smaller than that of EA1N ( $m= 2.99$ ) and bigger than EA4T ( $m= 2.11$ ) [35].

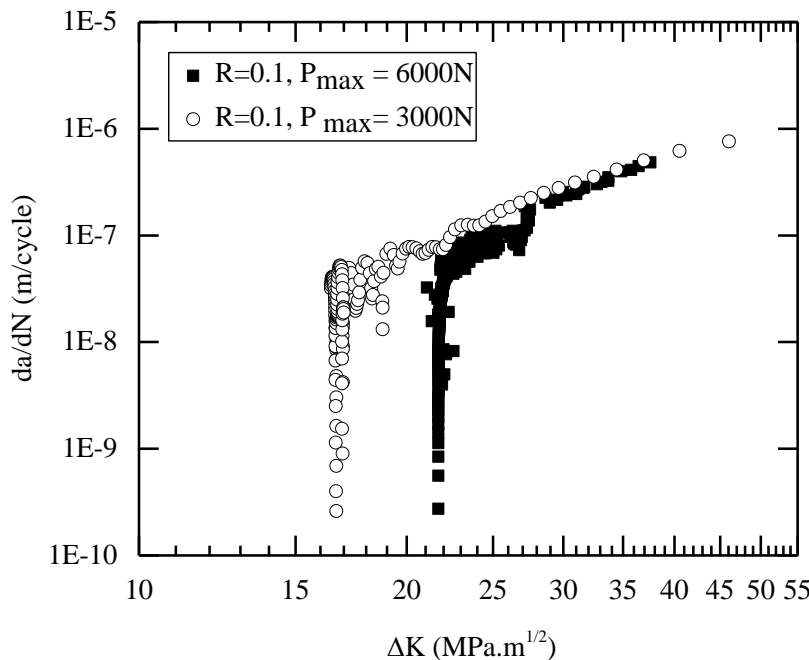


**Figure 103** Fatigue crack growth rate data for 34CrMo4 steel (normalized)

In practical application, estimation of remaining fatigue life by Paris law may not be reliable in the case of axle fretting. Because the circumferential fretting cracks behave as notch and thus the effective stress intensity at the crack tip is much higher than that of side cracks. Furthermore, the rate of crack propagation is not uniform around the circumference as shown in the three-dimensional distribution of the examined axles.

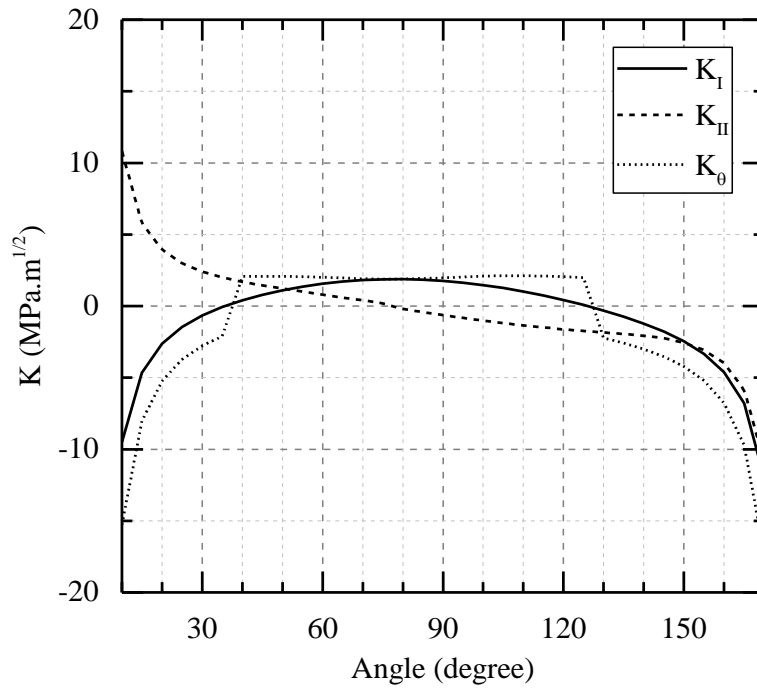
#### 4.3.2.3. *Maximum Tangential Stress Criterion*

Weight function solutions for “an inclined edge crack on a semi-plane” by Beghini et. al. was used to calculate the stress intensity factor on a fretting crack [56, 80]. The stress profile on the crack was computed by translating the stress distribution along the wheel seat obtained by FEA . The computed intensity factor ( $K_I$  and  $K_{II}$ ) were used to estimate the intensity factor ( $K_\Theta$ ) and crack tip deflections ( $\Theta$ ) caused by maximum tangential stress ( $\sigma_{\Theta, \max}$ ). Crack propagation under mixed mode loading was evaluated by comparing the estimated  $K_\Theta$  with the fatigue crack threshold limits determine by fatigue crack growth rate tests and Kitagawa-Takahashi analysis.

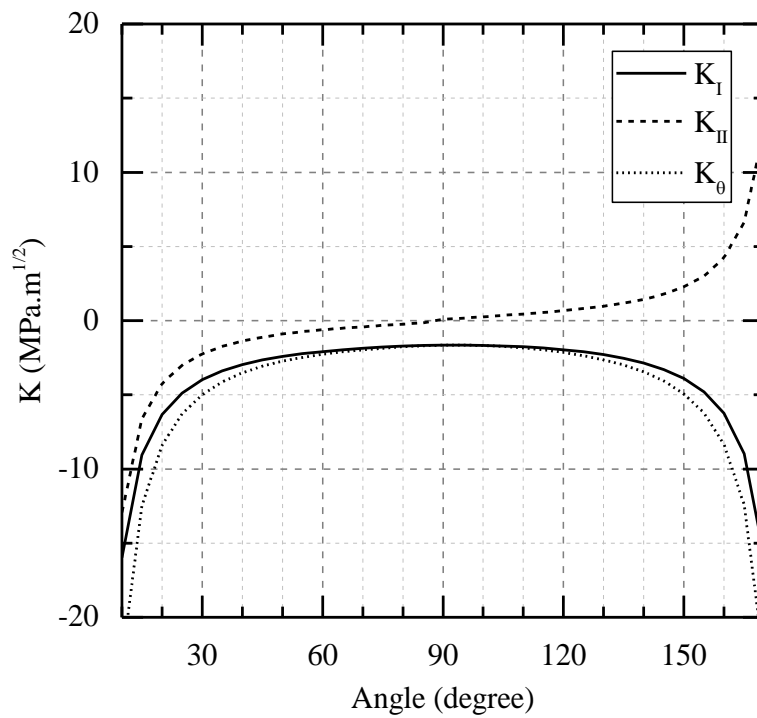
##### 4.3.2.3.1. Prediction of Fatigue Crack Initiation

Fractographic examination of the broken axles revealed a typical major crack angle ranging from  $65^\circ$  to  $75^\circ$  and at the distances 17mm and 22 mm away from S transition.  $K_I$ ,  $K_{II}$  and corresponding  $K_\Theta$  for 110  $\mu\text{m}$  deep inclined cracks within  $10^\circ$  - $170^\circ$  range are presented Figure 104. The method was applied to the nodes within 2.5-30 mm region from S transition where the stress gradient is regular.

Comparison of Figure 104a and Figure 104b reveals that  $K_I$  remains negative during the entire rolling period for the cracks which are located between  $0^\circ$  and  $38^\circ$ ,  $128^\circ$  and  $180^\circ$  (Figure 104 a). The value of  $K_\Theta$  is also negative in this region. The probability of crack propagation is higher between  $38^\circ$  and  $128^\circ$  crack angles where  $K_\Theta$  is maximized. The amplitude of the shear mode is more effective than that of the opening mode at the edges of positive  $K_I$ -transition corresponding to the angles of  $38^\circ$  and  $128^\circ$  (Figure 104 a) which are also consistent with crack observations on the maximum shear plane. The highest value of  $K_I$  is obtained at  $70^\circ$  (Figure 104 a). The computed stress intensity factors are all negative in the compression cycle (Figure 104b).



(a)



(b)

**Figure 104** Variations of stress intensity factors with a crack angle for 110  $\mu\text{m}$  deep cracks (a) maximum applied nominal stress (b) minimum applied nominal stress.



#### 4.3.2.3.1. Prediction of Fatigue Crack Propagation

Fracture appearance and stages of mixed mode propagation were discussed in the fractographic examination (Figure 90). SEM examinations showed the presence of non-rubbed fatigue striations appeared after a depth of 1600  $\mu\text{m}$  which indicated a transition to Mode I type crack propagation. Results of the weight function estimations for this critical depth (1600  $\mu\text{m}$ ) are given in Figure 105.

The most critical  $\Delta K_{\theta}$  values are identified at 5.75 mm away from the S transition (inside the contact). The value of the  $\Delta K_{\theta}$  is computed to be 8.41  $\text{MPa}\cdot\text{m}^{1/2}$  for 1600  $\mu\text{m}$  crack inclined at 70°.  $\Delta K_{\theta}$  reduces to 3.5 -4  $\text{MPa}\cdot\text{m}^{1/2}$  at a location 18-20 mm away from S transition, which is still comparable with the threshold limit determined by Kitagawa analysis (3.61  $\text{MPa}\cdot\text{m}^{1/2}$ ).

Fractographic evidence also showed Mode I dominance beyond this point. Consequently, 1600  $\mu\text{m}$  depth was found to be a critical value for the initiation of Mode I propagation. This size limit is also comparable with the limit predicted by multiaxial fatigue analysis.

The onset of crack propagation under the influence of mixed mode loading could not be evidenced due to excessive rubbing of the crack surfaces. Furthermore, the depth of oxide penetration inside the fatigue crack was about 300  $\mu\text{m}$  which can be considered as a base limit to short crack propagation.

The comparison of SIF at tension and compression cycles has shown that the propagation takes place at the tension cycle where both  $K_I$  and  $K_{II}$  are positive. The shear mode intensity ( $K_{II}$ ) during compression cycle may be the reason for extensive rubbing observed on the fractographs (Figure 89 and Figure 90). SIF computations also showed that the shear mode, and thus, the rubbing effect arises as the crack propagates further into the axle which is also in agreement with the earlier results [89].

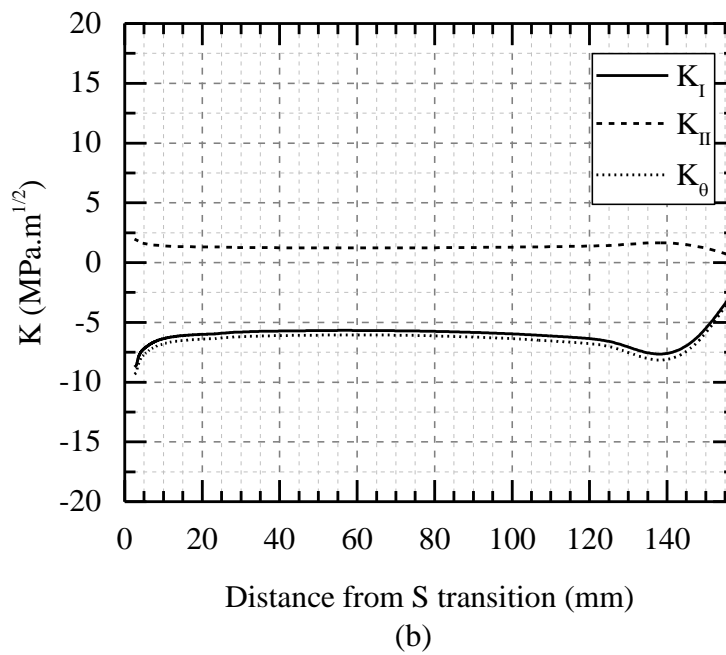
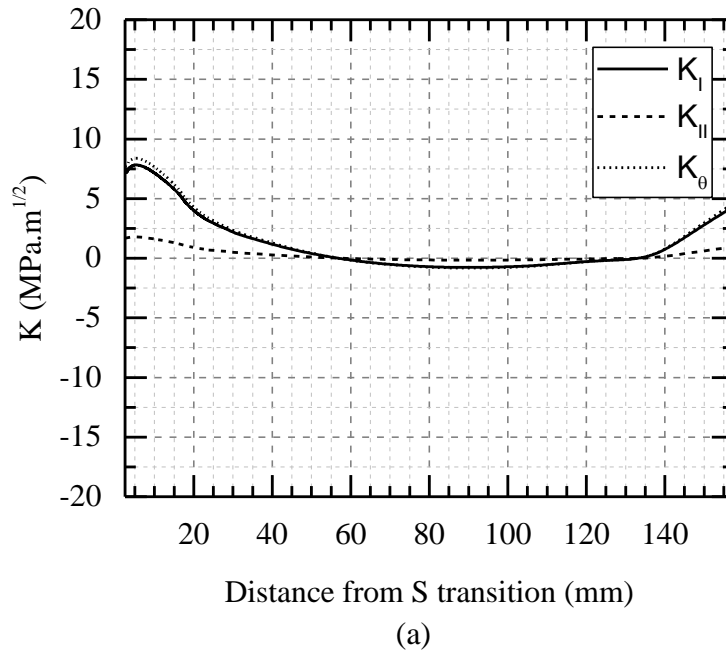


**Figure 105** Distribution of stress intensity factor for 70° degree inclined crack, with a depth of 1600  $\mu\text{m}$ , along press-fit (a) maximum applied nominal stress, (b) minimum applied nominal stress.

Fractography and the SIF calculations reveal Mode I dominance beyond a critical crack depth. Similarly, the major crack angle at the initiation stage was found to be around  $70^\circ$  by analytical and experimental results. Based on maximum tangential stress calculations, the expected crack tip deflection ( $\Theta$ ) is  $23^\circ$  in the final stage. The possible path of the crack tip is sketched in Figure 106.

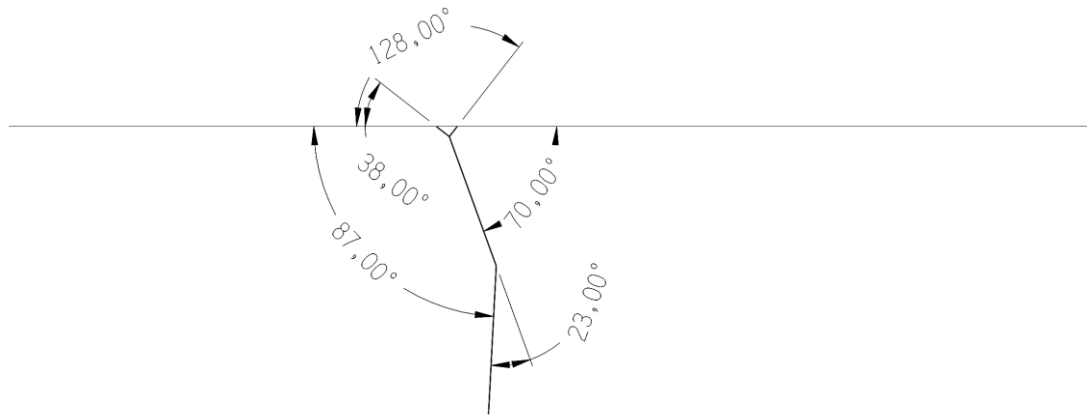


**Figure 106** Settlement of the estimated crack and its possible deflection.

Estimated crack shape and path is also in agreement with the micrographs presented in Figure 68 and maximum shear plane calculations.



## CHAPTER 5

### SUMMARY AND CONCLUSIONS

Applicability of multiaxial fatigue approaches to the fretting fatigue of railway axles was presented in this study. A new technical procedure that can be utilized in the optimization of fretting fatigue resistance was introduced. Development of a design tool to assess the structural integrity of press-fitted wheelsets under fretting fatigue conditions was aimed. The proposed methods were based on the post-processing of stress history obtained through finite element analysis of the wheel-axle assembly.

The critical conditions for initiation and propagation of small fretting cracks were determined by the application of stress-based and fracture-mechanics-based multiaxial fatigue models. Calculated multiaxial fatigue index and the stress intensity factors for the identified stress paths were compared with the fatigue strength and threshold stress intensity factors determined from experimental Kitagawa-Takahashi analysis and uniaxial fatigue tests. The decrease in the uniaxial fatigue properties due to present fretting cracks were expressed by the El-Haddad correction curve that was fitted to the Kitagawa diagrams.

The calculated parameters by the proposed assessment procedure provided consistent results with the fractographic measurements taken from the damaged railway axles. Although the proposed evaluation procedures did not intend to calculate the number of cycles spent during the fretting crack initiation, the metallurgical and mechanical variables affecting the rate of fretting fatigue crack initiation was examined in the highest detail. The possible treatments to maximize the period of fretting crack initiation and debris accumulation were presented.

The following conclusions can be drawn from this particular study:

- Resistance against fretting fatigue may be improved by retarding the fretting crack formation on the material surface. The pearlite- ferrite grain boundaries on the contact surface are not resistant to the fretting fatigue initiation as a result of the non-homogenous deformation of ferrite and cementite phases.

- The fatigue crack initiation period is the major part of the fretting fatigue life. The small fretting cracks grow rapidly upon reaching the small crack threshold limit as stated by the fractographic evidence.
- The improvement of fretting fatigue life can be attained by retarding the crack initiation period through heat treatment, case hardening or surface treatment operations. Toughening and generating compressive surface residual stresses by quenching and tempering or induction hardening should be used for improvement and prevention. Pearlitic microstructure should be avoided on the surface layer.
- The optimization of heat or surface treatments may be aided by the use of proposed assessment procedure through small-scale mechanical test results. However, the tribological effect of tempered martensite morphology, and thus the ease of fretting crack initiation, is not reflected by the applied methods.
- Initiation of fretting cracks is associated with the incremental collapse of surface asperities and contributed by the following abrasive effect of entrapped debris. The area of normal contact should be maximized by applying a fine surface finish. The rough surfaces should be avoided within the contact area.
- The deformable sulfide inclusions or volume defects below the press-fitted contact result in sub-surface fretting cracks. Observations on the hot-forged axles showed that the sulfide inclusions align along the longitudinal axis of the axle. The sub-surface cracks emanated from the tips of the sulfide inclusions are parallel to the surface and are in the arrested condition.
- The severity of fretting fatigue is determined by the relative movement of contact surfaces. The amount of slip at the stick-slip interface, and thus, the rate of fretting crack initiation can be minimized by increasing the press-fit interference to an optimum level.
- The predicted fretting sensitive locations are slightly closer to the S transition when compared to the locations shown by MPI. This can be explained by the loose press-fit of the wheel assembly in the real application and loss of tightness and friction caused by fretting wear. The expected outcome of the

both cases is displacement of stick-slip boundary towards the central portion of the contact as evidenced by FEA.

- The fatigue life estimations between the short and long crack threshold limits can be utilized for deciding the optimum frequency of successive inspection intervals. The effect of crack closure and notch sensitivity of the axle material should be taken into consideration. The estimations based on the LEFM conditions may be conservative for ductile materials.
- The onset of fatigue crack propagation estimated by the maximum tangential stress criteria is about 800  $\mu\text{m}$ . The value obtained by the modified Dang-Van model is very close while the one achieved by the Liu-Mahadevan model is slightly conservative.
- The results obtained by fracture mechanics approach are in agreement with fractographic measurements. The gradual loss of rubbing effect up to a depth of 1.6mm can be successfully presented by the stress intensity factor predictions using weight function solution.
- The estimated path of fretting cracks is consistent with the experimental crack paths observed during SEM investigations.

In summary, the proposed multiaxial fatigue assessment procedure provides reliable results which are consistent with the experimental data. The presented approaches and multiaxial fatigue models are capable of describing the onset of fretting fatigue crack propagation by using FEA outputs and mechanical test results. The proposed analytical, numerical and experimental methods can be effectively utilized in improvement of the axle design and optimization of the assembly parameters at the design stage. Furthermore, the effect of heat treatments, case hardening operations or material replacements can be evaluated based on the small scale mechanical tests by using the proposed methods. Finally, the proposed procedure can be used in structural integrity assessment, and the maintenance cost can be reduced through the declaration of non-conservative defect acceptance criteria and an optimized NDI frequency.





## REFERENCES

- [1] R.A. Smith, Hatfield Memorial Lecture 2007 Railways and materials: synergetic progress, *Ironmaking & Steelmaking*, 35 (2008) 505-513.
- [2] EN 13104 Railway Applications - Wheelsets and Bogies - Powered Axles - Design Method, 2001.
- [3] EN 13103 Railway Applications - Wheelsets and Bogies - Non Powered Axles - Design Method 2000.
- [4] EN 13262 Railway Applications - Wheelsets and Bogies - Wheels - Product Requirements, 2004.
- [5] EN 13260 Railway Applications – Wheelsets and Bogies – Wheelsets – Products Requirements, 2005.
- [6] EN 13261 Railway Applications - Wheelsets and Bogies - Axles - Product Requirements, 2009.
- [7] C. Lonsdale, D. Stone, North American axle failure experience, *Proceedings of the Institution of Mechanical Engineers, Part F: Journal of Rail and Rapid Transit*, 218 (2004) 293-298.
- [8] U. Zerbst, C. Klinger, D. Klingbeil, Structural assessment of railway axles – A critical review, *Engineering Failure Analysis*, 35 (2013) 54-65.
- [9] S. Cantini, S. Beretta, *Structural Reliability Assessment of Railway Axles*, Lucchini RS, 2011.
- [10] M.P. Szolwinski, T.N. Farris, Mechanics of fretting fatigue crack formation, *Wear*, 198 (1996) 93-107.
- [11] A. Keskin Tekerlek ve aks imalatı, in, DATEM, Ankara 2010.
- [12] S. Suresh, *Fatigue of Materials*, Cambridge University Press, 1998.
- [13] O. Horger, Influence of fretting corrosion on the fatigue strength of fitted members, in: *Symposium on Fretting Corrosion*, ASTM International, 1952.
- [14] K. Hirakawa, K. Toyama, M. Kubota, The analysis and prevention of failure in railway axles, *International Journal of Fatigue*, 20 (1998) 135-144.
- [15] A. Ekberg, Fretting fatigue of railway Axles—A review of predictive methods and an outline of a finite element model, *Proceedings of the Institution of Mechanical Engineers, Part F: Journal of Rail and Rapid Transit*, 218 (2004) 299-316.
- [16] S. Foletti, S. Beretta, G. Gurer, Defect acceptability under full-scale fretting fatigue tests for railway axles, *International Journal of Fatigue*, (2015) 34-43.
- [17] T. Hattori, M. Nakamura, T. Watanabe, Simulation of fretting-fatigue life by using stress-singularity parameters and fracture mechanics, *Tribology International*, 36 (2003) 87-97.

- [18] M. Kubota, S. Kataoka, Y. Kondo, Effect of stress relief groove on fretting fatigue strength and index for the selection of optimal groove shape, *International Journal of Fatigue*, 31 (2009) 439-446.
- [19] C.D. Lykins, S. Mall, V. Jain, An evaluation of parameters for predicting fretting fatigue crack initiation, *International Journal of Fatigue*, 22 (2000) 703-716.
- [20] T. Makino, T. Kato, K. Hirakawa, Review of the fatigue damage tolerance of high-speed railway axles in Japan, *Engineering Fracture Mechanics*, 78 (2011) 810-825.
- [21] C. Song, M. Shen, X. Lin, D. Liu, M. Zhu, An investigation on rotatory bending fretting fatigue damage of railway axles, *Fatigue and Fracture of Engineering Materials and Structures*, 37 (2014) 72-84.
- [22] M. Nesládek, M. Španiel, J. Jurenka, J. Růžička, J. Kuželka, Fretting fatigue—experimental and numerical approaches, *International Journal of Fatigue*, 44 (2012) 61-73.
- [23] C. Navarro, S. Muñoz, J. Domínguez, On the use of multiaxial fatigue criteria for fretting fatigue life assessment, *International Journal of Fatigue*, 30 (2008) 32-44.
- [24] D. Socie, G. Marquis, *Multiaxial Fatigue*, Society of Automotive Engineers, 2000.
- [25] S. Fouvry, D. Nowell, K. Kubiak, D.A. Hills, Prediction of fretting crack propagation based on a short crack methodology, *Engineering Fracture Mechanics*, 75 (2008) 1605-1622.
- [26] M. Luke, I. Varfolomeev, K. Lütkepohl, A. Esderts, Fatigue crack growth in railway axles: Assessment concept and validation tests, *Engineering Fracture Mechanics*, 78 (2011) 714-730.
- [27] U. Zerbst, S. Beretta, G. Köhler, A. Lawton, M. Vormwald, H.T. Beier, C. Klinger, I. Černý, J. Rudlin, T. Heckel, D. Klingbeil, Safe life and damage tolerance aspects of railway axles – A review, *Engineering Fracture Mechanics*, 98 (2013) 214-271.
- [28] M. Kubota, S. Niho, C. Sakae, Y. Kondo, Effect of Understress on Fretting Fatigue Crack Initiation of Press-Fitted Axle, *JSME International Journal Series A Solid Mechanics and Material Engineering*, 46 (2003) 297-302.
- [29] K. Nishioka, Fundamental investigations of fretting fatigue: part 6, effects of contact pressure and hardness of materials, *Bulletin of JSME*, 15 (1972) 135-144.
- [30] K. Nishioka, K. Hirakawa, Fundamental investigations of fretting fatigue : Part 5, the effect of relative slip amplitude, *Bulletin of JSME*, 12 (1969) 692-697.
- [31] K. Nishioka, K. Hirakawa, Fundamental Investigations of Fretting Fatigue: Part 2, fretting fatigue testing machine and some test results, *Bulletin of JSME*, 12 (1969) 180-187.

- [32] K. Nishioka, K. Hirakawa, Fundamental investigations of fretting fatigue: Part 3, some phenomena and mechanisms of surface cracks, *Bulletin of JSME*, 12 (1969) 397-407.
- [33] K. Nishioka, K. Hirakawa, Fundamental investigations of fretting fatigue: Part 4, the effect of mean stress, *Bulletin of JSME*, 12 (1969) 408-414.
- [34] K. Nishioka, S. Nishimura, K. Hirakawa, Fundamental investigations of fretting fatigue: Part 1, on the relative slip amplitude of press-fitted axle assemblies, *Bulletin of JSME*, 11 (1968) 437-445.
- [35] V. Linhart, I. Černý, An effect of strength of railway axle steels on fatigue resistance under press fit, *Engineering Fracture Mechanics*, 78 (2011) 731-741.
- [36] S. Guzowski, M. Michnej, Influence of technological methods increasing surface layer durability on axles fretting wear in railway wheel sets, (2016).
- [37] K. Kubiak, S. Fouvry, A.M. Marechal, J.M. Vernet, Behaviour of shot peening combined with WC-Co HVOF coating under complex fretting wear and fretting fatigue loading conditions, *Surface and Coatings Technology*, 201 (2006) 4323-4328.
- [38] L. Ke, Y. Wang, Fretting contact with finite friction of a functionally graded coating with arbitrarily varying elastic modulus Part 1: Normal loading, *The Journal of Strain Analysis for Engineering Design*, 42 (2007) 293-304.
- [39] D.W. Hoepfner, Mechanisms of fretting fatigue and their impact on test methods development, *Astm Special Technical Publication*, 1159 (1992) 23-23.
- [40] J. Williams, *Engineering Tribology*, Cambridge University Press, 2005.
- [41] W. Maxwell, B. Dudley, A. Cleary, J. Richards, J. Shaw, Measures to counter fatigue failure in railway axles, *Journal of the Institution of Locomotive Engineers*, 58 (1968) 136-171.
- [42] R.B. Waterhouse, *Fretting Corrosion*, Pergamon Press, 1972.
- [43] G.E. Dieter, D. Bacon, *Mechanical Metallurgy*, McGraw-Hill, 1988.
- [44] O. Vingsbo, S. Söderberg, On fretting maps, *Wear*, 126 (1988) 131-147.
- [45] K. Johnson, *Contact mechanics*, 1985, in, Cambridge University Press, Cambridge, 1974.
- [46] M. Akkok, *Tribology Lecture Notes*, Middle East Technical University, Ankara, 2011.
- [47] P.L. Hurricks, The mechanism of fretting — A review, *Wear*, 15 (1970) 389-409.
- [48] Y. Berthier, L. Vincent, M. Godet, Fretting fatigue and fretting wear, *Tribology International*, 22 (1989) 235-242.
- [49] K. Endo, H. Goto, Initiation and propagation of fretting fatigue cracks, *Wear*, 38 (1976) 311-324.

- [50] D.A. Hills, D. Nowell, J.J. O'Connor, On the mechanics of fretting fatigue, *Wear*, 125 (1988) 129-146.
- [51] F. Alwahdi, F.J. Franklin, A. Kapoor, The effect of partial slip on the wear rate of rails, *Wear*, 258 (2005) 1031-1037.
- [52] F. Alwahdi, F. Franklin, A. Kapoor, The Effect of Partial Slip on the Wear Rate of Rails, *Wear*, 258 (2005) 1031-1037.
- [53] K. Johnson, *Contact mechanics*, Cambridge University Press, 1987.
- [54] R.G. Budynas, J.K. Nisbett, J.E. Shigley, *Shigley's mechanical engineering design*, 10th ed., McGraw-Hill, New York, 2014.
- [55] A.H. Slocum, *Precision machine design*, Prentice Hall, Englewood Cliffs, N.J., 1992.
- [56] M. Beghini, C. Santus, An application of the weight function technique to inclined surface cracks under rolling contact fatigue: Assessment and parametric analysis, *Engineering Fracture Mechanics*, 98 (2013) 153-168.
- [57] L. Pook, On fatigue crack paths, *International Journal of Fatigue*, 17 (1995) 5-13.
- [58] M.H. El Haddad, K.N. Smith, T.H. Topper, Fatigue Crack Propagation of Short Cracks, *Journal of Engineering Materials and Technology*, 101 (1979) 42-46.
- [59] H. Kitagawa, S. Takahashi, Applicability of fracture mechanics to very small cracks or the cracks in the early stage, in: *Second International Conference on Mechanical Behavior of Materials*. ASM, Metals Park, Ohio. 1976, 627-631, 1976.
- [60] S. Beretta, M. Filippini, M. Giglio, EU Project Euraxles WP3-Kitagawa Diagram for A4T Steel, in, *Politecnico di Milano*, Milano, 2012.
- [61] M. El Haddad, K. Smith, T. Topper, Fatigue crack propagation of short cracks, *Journal of Engineering Materials and Technology*, 101 (1979) 42-46.
- [62] K. Tanaka, Y. Nakai, M. Yamashita, Fatigue growth threshold of small cracks, *International Journal of Fracture*, 17 (1981) 519-533.
- [63] Y. Murakami, *Stress Intensity Factors Handbook*, Pergamon Press, 1988.
- [64] Y. Murakami, *Metal Fatigue: Effects of small defects and nonmetallic inclusions: effects of small defects and nonmetallic inclusions*, Elsevier, 2002.
- [65] A. Ekberg, E. Kabo, Fatigue of railway wheels and rails under rolling contact and thermal loading—an overview, *Wear*, 258 (2005) 1288-1300.
- [66] H. Gough, Engineering steels under combined cyclic and static stresses, *Proceedings of the Institution of Mechanical Engineers*, 160 (1949) 417-440.
- [67] H. Gough, H. Pollard, The Strength of Metals Under Combined Alternating Stresses, *Proceedings of the Institution of Mechanical Engineers*, 131 (1935) 3-103.
- [68] G. Sines, *Failure of Materials Under Combined Repeated Stresses With Superimposed Static Stresses*, National Advisory Committee for Aeronautics, 1955.

- [69] G. Sines, Behavior of Metals Under Complex Static and Alternating Stresses, *Metal Fatigue*, 1 (1959) 145-169.
- [70] W.N. Findley, A theory for the effect of mean stress on fatigue of metals under combined torsion and axial load or bending, *Engineering Materials Research Laboratory, Division of Engineering, Brown University*, 1958.
- [71] W.N. Findley, P.N. Mathur, Modified theories of fatigue failure under combined stress, 1954.
- [72] T. Mataka, An explanation on fatigue limit under combined stress, *Bulletin of JSME*, 20 (1977) 257-263.
- [73] D. McDiarmid, A general criterion for high cycle multiaxial fatigue failure, *Fatigue & Fracture of Engineering Materials & Structures*, 14 (1991) 429-453.
- [74] D. McDiarmid, A shear stress based critical-plane criterion of multiaxial fatigue failure for design and life prediction, *Fatigue and Fracture of Engineering Materials and Structures*, 17 (1994) 1475-1484.
- [75] Y. Liu, S. Mahadevan, Multiaxial high-cycle fatigue criterion and life prediction for metals, *International Journal of Fatigue*, 27 (2005) 790-800.
- [76] K. Dang Van, I. Papadopoulos, High cycle metal fatigue from theory to applications, *CISM Courses and Lectures*, vol, 392 (1999).
- [77] K. Dang Van, B. Griveau, O. Message, On a new multiaxial fatigue limit criterion: Theory and application, *Biaxial and Multiaxial Fatigue*, 3 (1989) 479-496.
- [78] E. Orowan, Fundamentals of brittle behavior in metals, *Fatigue and Fracture of Metals*, (1952) 139-167.
- [79] H. Tada, P. Paris, G. Irwin, *The Analysis of Cracks Handbook*, New York: ASME Press, 2000.
- [80] M. Beghini, L. Bertini, V. Fontanari, Weight function for an inclined edge crack in a semiplane, *International Journal of fracture*, 99 (1999) 281-292.
- [81] M. Beghini, L. Bertini, V. Fontanari, Stress intensity factors for an inclined edge crack in a semiplane, *Engineering Fracture Mechanics*, 62 (1999) 607-613.
- [82] M. Kuna, *Finite Elements in Fracture Mechanics: Theory - Numerics - Applications*, Springer, 2013.
- [83] A.T. Zehnder, *Fracture Mechanics*, Springer, 2012.
- [84] A.C. Ugural, S.K. Fenster, *Advanced Strength and Applied Elasticity*, Pearson Education, 2003.
- [85] ASTM E399 Standard Test Method for Linear-Elastic Plane-Strain Fracture Toughness of Metallic Materials, ASTM International, 2012.
- [86] ASTM E1820 Standard Test Method for Measurement of Fracture Toughness, ASTM International, 2013.

- [87] K. Tanaka, S. Matsuoka, M. Kimura, Fatigue strength of 7075-T6 aluminium alloy under combined axial loading and torsion, *Fatigue and Fracture of Engineering Materials and Structures*, 7 (1984) 195-211.
- [88] K. Tanaka, Y. Akinawa, H. Yu, Propagation of a circumferential fatigue crack in medium-carbon steel bars under combined torsional and axial loadings, *ASTM Special Technical Publication*, (1999) 295-311.
- [89] A. Otsuka, K. Mori, T. Miyata, The condition of fatigue crack growth in mixed mode condition, *Engineering Fracture Mechanics*, 7 (1975) 429-439.
- [90] Y.G. Matvienko, Maximum average tangential stress criterion for prediction of the crack path, *International Journal of Fracture*, 176 (2012) 113-118.
- [91] K. Tanaka, Fatigue crack propagation from a crack inclined to the cyclic tensile axis, *Engineering Fracture Mechanics*, 6 (1974) 493-507.
- [92] G.C. Sih, *Mechanics of fracture initiation and propagation: surface and volume energy density applied as failure criterion*, Springer Science & Business Media, 2012.
- [93] G.C. Sih, B.M. Barthelemy, Mixed mode fatigue crack growth predictions, *Engineering Fracture Mechanics*, 13 (1980) 439-451.
- [94] ISO 12135 Metallic materials — Unified method of test for the determination of quasistatic fracture toughness, ISO, 2015.
- [95] ASTM E1290 Standard Test Method for Crack-Tip Opening Displacement (CTOD) Fracture Toughness Measurement, 2013.
- [96] Iso 12107:2003 Metallic Materials - Fatigue Testing - Statistical Planning and Analysis of Data, 2003.
- [97] ISO 1099:2006 Metallic materials -- Fatigue testing -- Axial force-controlled method, ISO, 2006.
- [98] ISO 1352:2011 Metallic materials - Torque-controlled fatigue testing, 2011.
- [99] ASTM E647 Standard Test Method for Measurement of Fatigue Crack Growth Rates, ASTM International, 2013.
- [100] ASTM E606/E606M Standard Test Method for Strain-Controlled Fatigue Testing, ASTM International, 2004.
- [101] EN 10083-3:2006 Steels for quenching and tempering - Part 3: Technical Delivery Conditions for Alloy Steel, 2006.
- [102] A.J. McEvily, *Metal Failures: Mechanisms, Analysis, Prevention*, John Wiley & Sons, 2002.
- [103] S. Mall, S.A. Namjoshi, W.J. Porter, Effects of microstructure on fretting fatigue crack initiation behavior of Ti-6Al-4V, *Materials Science and Engineering: A*, 383 (2004) 334-340.

- [104] M.H. Wharton, D.E. Taylor, R.B. Waterhouse, Metallurgical factors in the fretting-fatigue behaviour of 70/30 brass and 0.7% carbon steel, *Wear*, 23 (1973) 251-260.
- [105] T. Bruce, E. Rounding, H. Long, R.S. Dwyer-Joyce, Characterisation of white etching crack damage in wind turbine gearbox bearings, *Wear*, 338–339 (2015) 164-177.
- [106] R.W. Hertzberg, *Deformation and Fracture Mechanics of Engineering Materials*, J. Wiley & Sons, 1996.
- [107] P.P. Milella, *Fatigue and Corrosion in Metals*, Springer Science & Business Media, 2012.
- [108] H. Desimone, A. Bernasconi, S. Beretta, On the application of Dang Van criterion to rolling contact fatigue, *Wear*, 260 (2006) 567-572.
- [109] Y. Murakami, M. Endo, Effects of defects, inclusions and inhomogeneities on fatigue strength, *International Journal of Fatigue*, 16 (1994) 163-182.
- [110] Y. Liu, B. Stratman, S. Mahadevan, Fatigue crack initiation life prediction of railroad wheels, *International Journal of Fatigue*, 28 (2006) 747-756.





## CURRICULUM VITAE

### PERSONAL INFORMATION

Surname, Name: Gürer, Göksu  
Nationality: Turkish (TC)  
Date and Place of Birth: 05 June 1984, Ankara  
Marital Status: Single  
Phone: +90 312 210 5841  
Fax: +90 312 210 2518  
email: gurer.goksu@gmail.com

### EDUCATION

Degree	Institution	Year of Graduation
B. Sc.	Dept. of Metallurgical & Materials Engrg. / METU	2007
Minor	Dept. of Aerospace Engrg. / METU	2007
M. Sc.	Dept. of Metallurgical & Materials Engrg. / METU	2010
PhD.	Dept. of Metallurgical & Materials Engrg. / METU	2017

### WORK EXPERIENCE

Year	Place	Enrollment
2006	Robert Bosch Tr. Diesel / Bursa	Project Assistant
2007-2012	Dept. of Metallurgical & Materials Engrg. / METU	Research Asisstant
2012-2013	Dept. of Mechanical Engrg. / Politecnico di Milano	Host Researcher
2013-2017	METU Welding Technology and Non-Destructive Testing Research / Application Center / METU	Coordinator, Structural Integrity and Advanced Mechanical Testing

### FOREIGN LANGUAGES

English (Advanced), Italian (Basic)

### PUBLICATIONS

1. Foletti S., Beretta S., Gürer G., "Defect acceptability under full-scale fretting fatigue tests for railway axles." *International Journal of Fatigue*: 34-43, (2015)
2. Gürer G., Gür H., "Failure analysis of fretting fatigue initiation and growth on railway axle press-fits," *under review, Case Studies in Engineering Failure Analysis*

### HOBBIES

Cycling, Scuba Diving, Skiing, Climbing, Handball, Model rocketry